



Universiteit Gent
Faculteit Wetenschappen
Vakgroep Fysica en Sterrenkunde

² No title yet

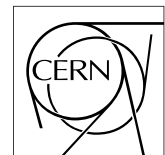
³ No sub-title neither, obviously...

⁴ Alexis Fagot

5



Thesis to obtain the degree of
Doctor of Philosophy in Physics
Academic years 2012-2017



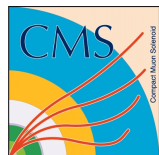


Universiteit Gent
Faculteit Wetenschappen
Vakgroep Fysica en Sterrenkunde

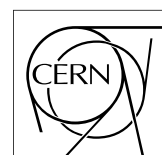
Promotoren: Dr. Michael Tytgat
Prof. Dr. Dirk Ryckbosch

Universiteit Gent
Faculteit Wetenschappen
Vakgroep Fysica en Sterrenkunde
Proeftuinstraat 86, B-9000 Gent, België
Tel.: +32 9 264.65.28
Fax.: +32 9 264.66.97

17



Thesis to obtain the degree of
Doctor of Philosophy in Physics
Academic years 2012-2017



Acknowledgements

¹⁹ Ici on remerciera tous les gens que j'ai pu croiser durant cette aventure et qui m'ont permis de passer
²⁰ un bon moment

²¹ *Gent, ici la super date de la mort qui tue de la fin d'écriture*
²² *Alexis Fagot*

Table of Contents

23

24	Acknowledgements	i
25	Nederlandse samenvatting	vii
26	English summary	ix
27	1 Introduction	1-1
28	1.1 A story of High Energy Physics	1-1
29	1.2 Organisation of this study	1-1
30	2 Investigating the TeV scale	2-1
31	2.1 The Standard Model of Particle Physics	2-2
32	2.1.1 A brief history of particle physics	2-2
33	2.1.2 Construction and test of the model	2-4
34	2.1.3 Investigating the TeV scale	2-4
35	2.2 The Large Hadron Collider & the Compact Muon Solenoid	2-4
36	2.2.1 LHC, the most powerful particle accelerator	2-4
37	2.2.1.1 Particle acceleration	2-5
38	2.2.1.2 LHC discoveries and LHC physics program	2-8
39	2.2.1.3 High Luminosity LHC	2-9
40	2.2.2 CMS, a multipurpose experiment	2-9
41	2.3 Muon Phase-II Upgrade	2-9
42	3 Physics of Resistive plate chambers	3-1
43	3.1 Principle	3-1
44	3.1.1 Electron drift velocity	3-4
45	3.2 Rate capability and time resolution of Resistive Plate Chambers	3-4
46	3.2.1 Operation modes	3-4
47	3.2.2 Detector designs and performance	3-6
48	3.2.2.1 Double-gap RPC	3-7
49	3.2.2.2 Multigap RPC (MRPC)	3-8
50	3.2.2.3 Charge distribution and performance limitations	3-9
51	3.3 Signal formation	3-12
52	3.4 Gas transport parameters	3-12
53	4 Longevity studies and Consolidation of the present CMS RPC subsystem	4-1
54	4.1 Resistive Plate Chambers at CMS	4-1
55	4.1.1 Overview	4-1
56	4.1.2 The present RPC system	4-2
57	4.1.3 Pulse processing of CMS RPCs	4-3
58	4.2 Testing detectors under extreme conditions	4-4

59	4.2.1	The Gamma Irradiation Facilities	4-7
60	4.2.1.1	GIF	4-7
61	4.2.1.2	GIF++	4-9
62	4.3	Preliminary tests at GIF	4-11
63	4.3.1	Resistive Plate Chamber test setup	4-11
64	4.3.2	Data Acquisition	4-13
65	4.3.3	Geometrical acceptance of the setup layout to cosmic muons	4-13
66	4.3.3.1	Description of the simulation layout	4-14
67	4.3.3.2	Simulation procedure	4-16
68	4.3.3.3	Results	4-17
69	4.3.4	Photon flux at GIF	4-17
70	4.3.4.1	Expectations from simulations	4-17
71	4.3.4.2	Dose measurements	4-22
72	4.3.5	Results and discussions	4-23
73	4.4	Longevity tests at GIF++	4-24
74	4.4.1	Description of the Data Acquisition	4-27
75	4.4.2	RPC current, environmental and operation parameter monitoring	4-28
76	4.4.3	Measurement procedure	4-29
77	4.4.4	Longevity studies results	4-29
78	5	Investigation on high rate RPCs	5-1
79	5.1	Rate limitations and ageing of RPCs	5-1
80	5.1.1	Low resistivity electrodes	5-1
81	5.1.2	Low noise front-end electronics	5-1
82	5.2	Construction of prototypes	5-1
83	5.3	Results and discussions	5-1
84	6	Conclusions and outlooks	6-1
85	6.1	Conclusions	6-1
86	6.2	Outlooks	6-1
87	A	A data acquisition software for CAEN VME TDCs	A-1
88	A.1	GIF++ DAQ file tree	A-1
89	A.2	Usage of the DAQ	A-2
90	A.3	Description of the readout setup	A-3
91	A.4	Data read-out	A-3
92	A.4.1	V1190A TDCs	A-4
93	A.4.2	DataReader	A-6
94	A.4.3	Data quality flag	A-10
95	A.5	Communications	A-12
96	A.5.1	V1718 USB Bridge	A-13
97	A.5.2	Configuration file	A-13
98	A.5.3	WebDCS/DAQ intercommunication	A-17
99	A.5.4	Example of inter-process communication cycle	A-18
100	A.6	Software export	A-18

101	B Details on the offline analysis package	B-1
102	B.1 GIF++ Offline Analysis file tree	B-1
103	B.2 Usage of the Offline Analysis	B-2
104	B.2.1 Output of the offline tool	B-3
105	B.2.1.1 ROOT file	B-3
106	B.2.1.2 CSV files	B-5
107	B.3 Analysis inputs and information handling	B-6
108	B.3.1 Dimensions file and IniFile parser	B-6
109	B.3.2 TDC to RPC link file and Mapping	B-7
110	B.4 Description of GIF++ setup within the Offline Analysis tool	B-9
111	B.4.1 RPC objects	B-9
112	B.4.2 Trolley objects	B-10
113	B.4.3 Infrastructure object	B-11
114	B.5 Handeling of data	B-12
115	B.5.1 RPC hits	B-13
116	B.5.2 Clusters of hits	B-14
117	B.6 DAQ data Analysis	B-15
118	B.6.1 Determination of the run type	B-16
119	B.6.2 Beam time window calculation for efficiency runs	B-17
120	B.6.3 Data loop and histogram filling	B-18
121	B.6.4 Results calculation	B-19
122	B.6.4.1 Rate normalisation	B-19
123	B.6.4.2 Rate and activity	B-21
124	B.6.4.3 Strip masking tool	B-23
125	B.6.4.4 Output CSV files filling	B-25
126	B.7 Current data Analysis	B-29

¹²⁷

Nederlandse samenvatting –Summary in Dutch–

¹²⁹ Le resume en Neerlandais (j'aurais peut-être pu apprendre la langue juste pour ça...).

¹²⁸

English summary

¹³¹ Le meme résume mais en Anglais (on commencera par la hein!).

List of Figures

132

133	2.1	CERN accelerator complex.	2-5
134	2.2	Pictures of the different accelerators. From top to bottom: first the LINAC 2 and the <i>Pb</i> source of LINAC 3. Then the Booster and the LEIR. Finally, the PS, the SPS and the LHC.	2-7
135	2.3	Figure 2.3a: schematics of the LHC cryodipoles. 1: Superconducting Coils, 2: Beam pipe, 3: Heat exchanger Pipe, 4: Helium-II Vessel, 5: Superconducting Bus-bar, 6: Iron Yoke, 7: Non-Magnetic Collars, 8: Vacuum Vessel, 9: Radiation Screen, 10: Thermal Shield, 11: Auxiliary Bus-bar Tube, 12: Instrumentation Feed Throughs, 13: Protection Diode, 14: Quadrupole Bus-bars, 15: Spool Piece Bus-bars. Figure 2.3b: magnetic field and resulting motion force applied on the beam particles. . .	2-8
136	2.4	Figure 2.4a: picture of the LHC quadrupoles. Figure 2.4b: magnetic fields and resulting focussing force applied on the beam by 2 consecutive quadrupoles.	2-8
137	2.5	Absorbed dose in the CMS cavern after an integrated luminosity of 3000 fb. R is the transverse distance from the beamline and Z is the distance along the beamline from the Interaction Point at Z=0.	2-9
138	2.6	A quadrant of the muon system, showing DTs (yellow), RPCs (light blue), and CSCs (green). The locations of new forward muon detectors for Phase-II are contained within the dashed box and indicated in red for GEM stations (ME0, GE1/1, and GE2/1) and dark blue for improved RPC (iRPC) stations (RE3/1 and RE4/1).	2-10
139	2.7	RMS of the multiple scattering displacement as a function of muon p_T for the proposed forward muon stations. All of the electromagnetic processes such as bremsstrahlung and magnetic field effect are included in the simulation.	2-11
140	3.1	Different phases of the avalanche development in the RPC gas volume subjected to a constant electric field E_0 . a) An avalanche is initiated by the primary ionisation caused by the passage of a charged particle through the gas volume. b) Due to its growing size, the avalanche starts to locally influence the electric field. c) The electrons, lighter than the cations reach the anode first. d) The ions reach the cathode. While the charges have not recombined, the electric field in the small region around the avalanche stays affected and locally blind the detector.	3-2
141	3.2	Effeciency (circles and stars with 30 mV and 100 mV thresholds respectively) and streamer probability (opened circles) as function of the operating voltatge of a 2 mm single gap HPL RPC flushed with a gas mixture containing (a) 5%, (b) 2%, (c) 1% and (d) no SF_6 [33].	3-3
142	3.3	Movement of the charge carriers in an RPC. Figure 3.3a: Voltage across an RPC whose electrode have a relative permittivity of 5 at the moment the tension s applied. Figure 3.3b: After the charge carriers moved, the electrodes are charged and there is no voltage drop over the electrodes anymore. The full potential is applied on the gas gap only. Figure 3.3c: The streamer discharge initiated by a charged particle transports electrons and cations towards the anode and cathode respectively.	3-5
143			
144			
145			
146			
147			
148			
149			
150			
151			
152			
153			
154			
155			
156			
157			
158			
159			
160			
161			
162			
163			
164			
165			
166			
167			
168			
169			
170			
171			

172	3.4	Typical oscilloscope pulses in streamer mode (Figure 3.4a) and avalanche mode(Figure 3.4b). In the case of streamer mode, the very small avalanche signal is visible.	3-5
173			
174	3.5	Rate capability comparison for the streamer and avalanche mode of operation. An order of magnitude in rate capability for a maximal efficiency drop of 10% is gained by using the avalanche mode over the streamer mode.	3-6
175			
176	3.6	Possible double-gap RPC layouts: a) "standard" 1D double-gap RPC, as used in CMS experiment, where the anodes are facing each other and a 1D read-out plane is sandwiched in between them, b) double read-out double-gap RPC as used in ATLAS experiment, where the cathodes are facing each other and 2 read-out planes are used on the outer surfaces. This last layout can offer the possibility to use a 2D reconstruction by using orthogonal read-out planes.	3-7
177			
178	3.7	Comparison of performance of CMS double and single gap RPCs using cosmic muons [44]. Figure 3.7a: Comparison of efficiency sigmoids. Figure 3.7b: Voltage distribution at 95% of maximum efficiency. Figure 3.7c: $\Delta_{10\%}^{90\%}$ distribution.	3-7
179			
180	3.8	Presentation of ALICE MRPC using 250 μm gas gaps, 620 μm outer glass electrodes and 550 μm inner floating electrodes. More details on the labels are given in [45].	3-8
181			
182	3.9	Particle identification applied to electrons in the STAR experiment. The identification is performed combining ToF and dE/dx measurements [50].	3-9
183			
184	3.10	Comparison of the detector performance of ALICE ToF MRPC [51] at fixed applied voltage (in blue) and at fixed effective voltage (in red). The effective voltage is kept fixed by increasing the applied voltage accordingly to the current drawn by the detector.	3-9
185			
186	3.11	Ratio between total induced and drifting charge have been simulated for single gap, double-gap and multigap layouts [52]. The total induced charge for a double-gap RPC is a factor 2 higher than for a multigap.	3-10
187			
188	3.12	Charge spectra have been simulated for single gap, double-gap and multigap layouts [52]. It appears that when single gap shows a decreasing spectrum, double and multigap layouts exhibit a spectrum whose peak is detached from the origin. The detachment gets stronger as the number of gaps increases.	3-11
189			
200	3.13	The maximal theoretical efficiency is simulated for single gap, double-gap and multi-gap layouts [52] at a constant gap thickness of 2 mm and using an effective Townsend coefficient of 9 mm^{-1}	3-11
201			
202			
203	4.1	Signals from the RPC strips are shaped by the FEE described on Figure 4.1a. Output LVDS signals are then read-out by a TDC module connected to a computer or converted into NIM and sent to scalers. Figure 4.1b describes how these converted signals are put in coincidence with the trigger.	4-3
204			
205			
206			
207	4.2	Description of the principle of a CFD. A comparison of threshold triggering (left) and constant fraction triggering (right) is shown in Figure 4.2a. Constant fraction triggering is obtained thanks to zero-crossing technique as explained in Figure 4.2b. The signal arriving at the input of the CFD is split into three components. A first one is delayed and connected to the inverting input of a first comparator. A second component is connected to the noninverting input of this first comparator. A third component is connected to the noninverting input of another comparator along with a threshold value connected to the inverting input. Finally, the output of both comparators is fed through an AND gate.	4-4
208			
209			
210			
211			
212			
213			
214			
215			
216	4.3	(4.3a) Extrapolation from 2016 data of single hit rate per unit area in the barrel region. (4.3b) Extrapolation from 2016 data of single hit rate per unit area in the endcap region.	4-6
217			
218			

219	4.4	Background Fluka simulation compared to 2016 Data at $L = 10^{34} \text{ cm}^{-2} \cdot \text{s}^{-1}$ in the fourth endcap disk region. A mismatch in between simulation and data can be observed. [To be understood.]	4-7
220	4.5	Layout of the test beam zone called X5c GIF at CERN. Photons from the radioactive source produce a sustained high rate of random hits over the whole area. The zone is surrounded by 8 m high and 80 cm thick concrete walls. Access is possible through three entry points. Two access doors for personnel and one large gate for material. A crane allows installation of heavy equipment in the area.	4-8
221	4.6	^{137}Cs decays by β^- emission to the ground state of ^{137}Ba (BR = 5.64%) and via the 662 keV isomeric level of ^{137}Ba (BR = 94.36%) whose half-life is 2.55 min.	4-9
222	4.7	Floor plan of the GIF++ facility. When the facility downstream of the GIF++ takes electron beam, a beam pipe is installed along the beam line (z-axis). The irradiator can be displaced laterally (its center moves from $x = 0.65$ m to 2.15 m), to increase the distance to the beam pipe.	4-9
223	4.8	Simulated unattenuated current of photons in the xz plane (Figure 4.8a) and yz plane (Figure 4.8b) through the source at $x = 0.65$ m and $y = 0$ m. With angular correction filters, the current of 662 keV photons is made uniform in xy planes.	4-10
224	4.9	Description of the RPC setup. Dimensions are given in mm. A tent containing RPCs is placed at 1720 mm from the source container. The source is situated in the center of the container. RE-4-2-BARC-161 chamber is 160 mm inside the tent. This way, the distance between the source and the chambers plan is 2060 mm. Figure 4.9a provides a side view of the setup in the xz plane while Figure 4.9b shows a top view in the yz plane.	4-11
225	4.10	RE-4-2-BARC-161 chamber is inside the tent as described in Figure 4.9. In the top right, the two scintillators used as trigger can be seen. This trigger system has an inclination of 10° relative to horizontal and is placed above half-partition B2 of the RPCs. PMT electronics are shielded thanks to lead blocks placed in order to protect them without stopping photons from going through the scintillators and the chamber.	4-12
226	4.11	Hit distributions over all 3 partitions of RE-4-2-BARC-161 chamber is showed on these plots. Top, middle and bottom figures respectively correspond to partitions A, B, and C. These plots show that some events still occur in other half-partitions than B2, which corresponds to strips 49 to 64, in front of which the trigger is placed, con- tributing to the inefficiency of detection of cosmic muons. In the case of partitions A and C, the very low amount of data can be interpreted as noise. On the other hand, it is clear that a little portion of muons reach the half-partition B1, corresponding to strips 33 to 48.	4-13
227	4.12	Results are derived from data taken on half-partition B2 only. On the 18 th of June 2014, data has been taken on chamber RE-2-BARC-161 at building 904 (Prevessin Site) with cosmic muons providing us a reference efficiency plateau of $(97.54 \pm$ $0.15)\%$ represented by a black curve. A similar measurement has been done at GIF on the 21 st of July with the same chamber giving a plateau of $(78.52 \pm 0.94)\%$ represented by a red curve.	4-14
228	4.13	Representation of the layout used for the simulations of the test setup. The RPC is represented as a yellow trapezoid while the two scintillators as blue cuboids looking at the sky. A green plane corresponds to the muon generation plane within the sim- ulation. Figure 4.9a shows a global view of the simulated setup. Figure 4.9b shows a zommed view that allows to see the 2 scintillators as well as the full RPC plane.	4-15
229	4.14	γ flux $F(D)$ is plot using values from table 4.1. As expected, the plot shows similar attenuation behaviours with increasing distance for each absorption factors.	4-18

268	4.15	Figure 4.15a shows the linear approximation fit done via formulae 4.7 on data from table 4.2. Figure 4.15b shows a comparison of this model with the simulated flux using a and b given in figure 4.15a in formulae 4.4 and the reference value $D_0 =$ 50cm and the associated flux for each absorption factor F_0^{ABS} from table 4.1	4-20
272	4.16	Dose measurements has been done in a plane corresponding to the tents front side. This plan is 1900 mm away from the source. As explained in the first chapter, a lens-shaped lead filter provides a uniform photon flux in the vertical plan orthogonal to the beam direction. If the second line of measured fluxes is not taken into account because of lower values due to experimental equipments in the way between the source and the tent, the uniformity of the flux is well showed by the results.	4-22
278	4.17	4-23
279	4.18	Evolution of the maximum efficiency for RE2 (4.18a) and RE4 (4.18b) chambers with increasing extrapolated γ rate per unit area at working point. Both irradiated (blue) and non irradiated (red) chambers are shown.	4-25
282	4.19	Evolution of the working point for RE2 (4.19a) and RE4 (4.19b) with increasing extrapolated γ rate per unit area at working point. Both irradiated (blue) and non irradiated (red) chambers are shown.	4-25
285	4.20	Evolution of the maximum efficiency at HL-LHC conditions, i.e. a background hit rate per unit area of 300 Hz/cm^2 , with increasing integrated charge for RE2 (4.20a) and RE4 (4.20b) detectors. Both irradiated (blue) and non irradiated (red) chambers are shown. The integrated charge for non irradiated detectors is recorded during test beam periods and stays small with respect to the charge accumulated in irradiated chambers.	4-26
291	4.21	Comparison of the efficiency sigmoid before (triangles) and after (circles) irradiation for RE2 (4.21a) and RE4 (4.21b) detectors. Both irradiated (blue) and non irradiated (red) chambers are shown.	4-26
294	4.22	Evolution of the Bakelite resistivity for RE2 (4.22a) and RE4 (4.22b) detectors. Both irradiated (blue) and non irradiated (red) chambers are shown.	4-27
296	4.23	Evolution of the noise rate per unit area for the irradiated chamber RE2-2-BARC-9 only.	4-27
298	A.1	(A.1a) View of the front panel of a V1190A TDC module [58]. (A.1b) View of the front panel of a V1718 Bridge module [59]. (A.1c) View of the front panel of a 6U 6021 VME crate [60].	A-3
301	A.2	Module V1190A <i>Trigger Matching Mode</i> timing diagram [58].	A-4
302	A.3	Structure of the ROOT output file generated by the DAQ. The 5 branches (<code>EventNumber</code> , <code>number_of_hits</code> , <code>Quality_flag</code> , <code>TDC_channel</code> and <code>TDC_TimeStamp</code>) are visible on the left panel of the ROOT browser. On the right panel is visible the histogram cor- responding to the variable <code>nHits</code> . In this specific example, there were approximately 50k events recorded to measure the gamma irradiation rate on the detectors. Each event is stored as a single entry in the <code>TTree</code>	A-10
308	A.4	The effect of the quality flag is explained by presenting the content of <code>TBranch</code> <code>number_of_hits</code> of a data file without <code>Quality_flag</code> in Figure A.4a and the con- tent of the same <code>TBranch</code> for data corresponding to a <code>Quality_flag</code> where all TDCs were labelled as <code>GOOD</code> in Figure A.4b taken with similar conditions. It can be noted that the number of entries in Figure A.4b is slightly lower then in Figure A.4a due to the excluded events.	A-12

314	A.5	Using the same data as previously showed in Figure A.4, the effect of the quality flag is explained by presenting the reconstructed hit multiplicity of a data file without <code>Quality_flag</code> in Figure A.5a and the reconstructed content of the same RPC partition for data corresponding to a <code>Quality_flag</code> where all TDCs were labelled as <code>GOOD</code> in Figure A.5b taken with similar conditions. The artificial high content of bin 0 is completely suppressed.	A-12
320	A.6	WebDCS DAQ scan page. On this page, shifters need to choose the type of scan (Rate, Efficiency or Noise Reference scan), the gamma source configuration at the moment of data taking, the beam configuration, and the trigger mode. These information will be stored in the DAQ ROOT output. Are also given the minimal measurement time and waiting time after ramping up of the detectors is over before starting the data acquisition. Then, the list of HV points to scan and the number of triggers for each run of the scan are given in the table underneath.	A-14
327	B.1	Example of expected hit time distributions in the cases of efficiency (Figure B.1a) and noise/gamma rate per unit area (Figure B.1b) measurements as extracted from the raw ROOT files. The unit along the x-axis corresponds to ns. The fact that "the" muon peak is not well defined in Figure B.1a is due to the contribution of all the RPCs being tested at the same time that don't necessarily have the same signal arrival time. Each individual peak can have an offset with the ones of other detectors. The inconsistancy in the first 100 ns of both time distributions is an artefact of the TDCs and are systematically rejected during the analysis.	B-16
335	B.2	The effect of the quality flag is explained by presenting the reconstructed hit multiplicity of a data file without <code>Quality_flag</code> . The artificial high content of bin 0 is the effect of corrupted data.	B-19
338	B.3	Display of the masking tool page on the webDCS. The window on the left allows the shifter to edit <code>ChannelsMapping.csv</code> . To mask a channel, it only is needed to set the 3rd field corresponding to the strip to mask to 0. It is not necessary for older mapping file formats to add a 1 for each strip that is not masked as the code is versatile and the default behaviour is to consider missing mask fields as active strips. The effect of the mask is directly visible for noisy channels as the corresponding bin turns red. The global effect of masking strips will be an update of the rate value showed on the histogram that will take into consideration the rejected channels.	B-24

List of Tables

346

347	3.1	Properties of the most used electrode materials for RPCs.	3-4
348	4.1	Total photon flux ($E\gamma \leq 662$ keV) with statistical error predicted considering a ^{137}Cs activity of 740 GBq at different values of the distance D to the source along the x-axis of irradiation field [55].	4-17
349	4.2	Correction factor c is computed thanks to formulae 4.5 taking as reference $D_0 = 50$ cm and the associated flux F_0^{ABS} for each absorption factor available in table 4.1.	4-19
350	4.3	The data at D_0 in 1997 is taken from [55]. In a second step, using Equations 4.8 and 4.9, the flux at D can be estimated in 1997. Then, taking into account the attenuation of the source activity, the flux at D can be estimated at the time of the tests in GIF in 2014. Finally, assuming a sensitivity of the RPC to γ $s = 2 \cdot 10^{-3}$, an estimation of the hit rate per unit area is obtained.	4-21
351	A.1	Inter-process communication cycles in between the webDCS and the DAQ through file string signals.	A-19
352			
353			
354			
355			
356			
357			
358			
359			

List of Acronyms

List of Acronyms

A

366 AFL Almost Full Level

B

371 BARC Bhabha Atomic Research Centre
372 BLT Block Transfer
373 BR Branching Ratio

C

378 CAEN Costruzioni Apparecchiature Elettroniche Nucleari S.p.A.
379 CERN European Organization for Nuclear Research
380 CFD Constant Fraction Discriminator
381 CMS Compact Muon Solenoid
382 CSC Cathode Strip Chamber

D

387 DAQ Data Acquisition
388 DCS Detector Control Software
389 DQM Data Quality Monitoring
390 DT Drift Tube

F

395	FEE	Front-End Electronics
396	FEB	Front-End Board
397		
398		
399	G	
400		
401	GE-	Find a good description
402	GE1/1	Find a good description
403	GE2/1	Find a good description
404	GEANT	GEometry ANd Tracking - a series of software toolkit platforms developed by CERN
405		
406	GEM	Gas Electron Multiplier
407	GIF	Gamma Irradiation Facility
408	GIF++	new Gamma Irradiation Facility
409		
410		
411	H	
412		
413	HL-LHC	High Luminosity LHC
414	HPL	High-pressure laminate
415	HV	High Voltage
416		
417		
418	I	
419		
420	iRPC	improved RPC
421	IRQ	Interrupt Request
422	ISR	Intersecting Storage Rings
423		
424		
425	L	
426		
427	LEIR	Low Energy Ion Ring
428	LEP	Large Electron-Positron
429	LHC	Large Hadron Collider
430	LS1	First Long Shutdown
431	LS3	Third Long Shutdown
432	LV	Low Voltage
433	LVDS	Low-Voltage Differential Signaling
434		
435		
436	M	
437		
438	MC	Monte Carlo

439	MCNP	Monte Carlo N-Particle
440	ME-/	Find good description
441	ME0	Find good description
442	MRPC	Multigap RPC

443

444

N

446

447	NIM	Nuclear Instrumentation Module logic signals
-----	------------	----------------------------------------------

448

449

P

451

452	PS	Proton Synchrotron
453	PMT	PhotoMultiplier Tube

454

455

R

456

458	RE-/	Find a good description
459	RE2/2	Find a good description
460	RE3/1	Find a good description
461	RE3/2	Find a good description
462	RE4/1	Find a good description
463	RE4/2	Find a good description
464	RE4/3	Find a good description
465	RMS	Root Mean Square
466	ROOT	a framework for data processing born at CERN
467	RPC	Resistive Plate Chamber

468

469

S

470

472	SC	Synchrocyclotron
473	SM	Standard Model
474	SPS	Super Proton Synchrotron

475

476

T

477

478

479	TDC	Time-to-Digital Converter
480	ToF	Time-of-flight

481

482

483

484

485 webDCS

W

Web Detector Control System

1

Introduction

486

487

⁴⁸⁸ **1.1 A story of High Energy Physics**

⁴⁸⁹ **1.2 Organisation of this study**

2

490

491

Investigating the TeV scale

492 „We may regard the present state of the universe as the effect of the
493 past and the cause of the future. An intellect which at any given mo-
494 ment knew all of the forces that animate nature and the mutual posi-
495 tions of the beings that compose it, if this intellect were vast enough
496 to submit the data to analysis, could condense into a single formula
497 the movement of the greatest bodies of the universe and that of the
498 lightest atom; for such an intellect nothing could be uncertain and
499 the future just like the past would be present before its eyes.”

500

501 - Pierre Simon de Laplace, *A Philosophical Essay on Probabilities*, 1814

Throughout history, physics experiment became more and more powerful in order to investigate finer details of nature and helped understanding the elementary blocks of matter and the fundamental interactions that bond them in the microscopic world. Nowadays, the Standard Model (SM) of particle physics is the most accurate theory designed to explain the behaviour of particles and was able to make very precise predictions that are constantly verified, although some hints of new physics are visible as bricks are still missing to have a global comprehension of the Universe.

To highlight the limits of the SM and test the different alternative theories, ever more powerful machines are needed. This is in this context that the Large Hadron Collider (LHC) has been thought and built to accelerate and collide particles at energies exceeding anything that had been done before. Higher collision energies and high pile-up imply the use of enormous detectors to measure the properties of the interaction products. The Compact Muon Solenoid (CMS) is a multipurpose experiment that have been designed to study the proton-proton collisions of the LHC and give answers on various high energy physics scenari. Nevertheless, the luminosity delivered by the collider will in the future be increased to levels beyond the original plans to improve its discovery potential giving no choice to experiments such as CMS to upgrade their technologies to cope with the increased radiation levels and detection rates.

2.1 The Standard Model of Particle Physics

In this early 21st century it is now widely accepted that matter is made of elementary blocks referred to as *elementary particles*. The physics theory that classifies and describes the best the behaviour and interaction of such elementary particles is the so called Standard Model that formalizes 3 of the 4 fundamental interactions (electromagnetic, weak and strong interactions). It's development took place during the 20th century thanks to a strong collaboration in between the theoretical and experimental physicists.

525

2.1.1 A brief history of particle physics

The idea that nature is composed of elementary bricks, called *atomism*, is not contemporary as it was already discussed by Indian or Greek philosophers during antiquity. In Greece, atomism has been rejected by Aristotelianism as the existance of *atoms* would imply the existance of a void that would violate the physical principles of Aristotle philosophy. Aristotelianism has been considered as a reference in the european area until the 15th century and the italian *Rinascimento* where antic text and history started to be more deeply studied. The re-discovery of Platon's philosophy would allow to open the door to alternative theories and give a new approach to natural sciences where experimentation would become central. A new era of knowledge was starting. By the begining of the 17th century, atomism was re-discovered by philosophers and the very first attempt to estimate an *atom* size would be provided by Magnetus in 1646. Although his *atoms* correspond to what would nowadays be called *molecules*, Magnetus achieved feats by calculating that the number of molecules in a grain of incense would be of the order of 10^{18} simply by considering the time necessary to smell it everywhere in a large church after the stick was lit on. It is now known that this number only falls short by 1 order of magnitude.

541

An alternative philosophy to atomism popularized by Descartes was corpuscularianism. Built on ever divisible corpuscles, contrary to atoms, it's principles would be mainly used by alchemists like

543

544 Newton who would later develop a corpuscular theory of light. Boyle would combine together ideas
 545 of both atomism or corpuscularianism leading to mechanical philosophy. The 18th century have
 546 seen the development of engineering providing philosophical thought experiments with repeatable
 547 demonstration and a new point of view to explain the composition of matter and Lavoisier would
 548 greatly contribute to chemistry and atomism by publishing in 1789 a list of 33 chemical elements
 549 corresponding to what is now called *atoms*. In the early 19th century Dalton would summarize the
 550 knowledge on composition of matter and Fraunhofer would invent the spectrometer and discover
 551 the spectral lines. The rise of atomic physics, chemistry and mathematical formalism would unravel
 552 the different atomic elements and ultimately, the 20th century would see the very first sub-atomic
 553 particles.

554

555 The negative *electron* would be the first to be discovered in 1897 by Thompson after 3 decades
 556 of research on cathode rays and in 1900, Becquerel would show the *beta rays* emitted by radium had
 557 the same properties pointing to electrons as a constituent of atoms. In 1909, Rutherford and Royds
 558 showed that *alpha* particles could combine with 2 electrons to form a ${}^4\text{He}$ after they already con-
 559 strained the atom structure in 1907 through the gold foil experiment that highlighted atoms where
 560 mainly empty with nearly all its mass contained into a tiny positively charged *nucleus*. The link
 561 in between atomic number and number of positive charges contained into the nuclei would fast be
 562 understood and the different kind of element transmutation appeared to be purely nuclear processes
 563 making clear that the electromagnetic nature of chemical transformation could not possibly change
 564 nuclei. Thus a new branch in physics appeared to study nuclei exclusively: the nuclear physics
 565 which would in turn give birth to quantum physics.

566

567 By studying alpha emission, Rutherford reported in 1919 the very first nuclear reaction leading
 568 to the discovery that the hydrogen nucleus was composed of a single positively charged particle that
 569 was then baptised *proton*. This idea came from 1815 Prout's hypothesis proposing that all atoms
 570 are composed of "*protolytes*" (i.e. hydrogen atoms). By using scintillation detectors, Rutherford
 571 could highlight typical hydrogen nuclei signature and understand that the impact of alpha particles
 572 with nitrogen would knock out an hydrogen nucleus and produce an oxygen 17, as explicated in
 573 Formula 2.1 and would then postulate that protons are building bricks of all elements.

574



575 With this assumption and the discovery of isotopes together with Aston, elements with identical
 576 atomic number but different masses, Rutherford would propose that all elements' nuclei but hydro-
 577 gen's are composed of both charged particles, protons, and of chargeless particles, which he called
 578 *neutrons*, and that these neutral particles would help maintaining nuclei as one, as charged protons
 579 were likely to electrostatically repulse each other, and introduced the idea of a new force, a *nuclear*
 580 force. Though the first idea concerning neutrons was a bond state of protons and electrons as it was
 581 known that the beta decay, emitting electrons, was taking place in the nucleus, it was then showed
 582 that such a model would hardly be possible due to Heisenberg's uncertainty principle and by the
 583 recently measured *spin* of both protons and electrons. The spin, discovered through the study of
 584 the emission spectrum of alkali metals, would be understood as a "two-valued quantum degree of
 585 freedom" and formalized by Pauli and extended by Dirac, to take the relativist case into account.
 586 Measured to be $\frac{1}{2}\hbar$ for both, it was impossible to arrange an odd number of half integer spins and

587 obtain a global nucleus spin that would be integer. Finally, in 1932, following the discovery of a new
588 neutral radiation, Chadwick could discover the neutron as an uncharged particle with a mass similar
589 to that of the proton.

590

591 **2.1.2 Construction and test of the model**

592 **2.1.3 Investigating the TeV scale**

593 **2.2 The Large Hadron Collider & the Compact Muon Solenoid**

594 Throughout its history, CERN has played a leading role in high energy particle physics. Large re-
595 gional facilities such as CERN were thought after the second world war in an attempt to increase
596 international scientific collaboration and allows scientists to share the forever increasing costs of
597 experiment facilities required due to the need for increasing the energy in the center of mass to
598 deeper probe matter. The construction of the first accelerators at the end of the 50s, the Synchro-
599 cyclotron (SC) and the Proton Synchrotron (PS), was directly followed by the first observation of
600 antinuclei in 1965 [1]. Strong from the experience of the Intersecting Storage Rings (ISR), the very
601 first proton-proton collider that showed hints that protons are not elementary particles, the Super
602 Proton Synchrotron (SPS) was built in the 70s to investigate the structure of protons, the preference
603 for matter over antimatter, the state of matter in the early universe or exotic particles, and lead to
604 the discovery in 1983 of the W and Z bosons [2–5]. These newly discovered particles and the elec-
605 troweak interaction would then be studied in details by the Large Electron-Positron (LEP) collider
606 that will help to prove in 1989 that there only are three generations of elementary particles [6]. The
607 LEP would then be dismantled in 2000 to allow for the LHC to be constructed in the existing tunnel.

608 **2.2.1 LHC, the most powerful particle accelerator**

609 The LHC has always been considered as an option to the future of CERN. At the moment of the
610 construction of the LEP beneath the border between France and Switzerland, the tunnel was built in
611 order to accomodate what would be a Large Hadron Collider with a dipole field of 10 T and a beam
612 energy in between 8 and 9 TeV [7] directly followed in 1985 with the creation of a 'Working Group
613 on the Scientific and Technological Future of CERN' to investigate such a collider [8]. The decision
614 was finally taken almost 10 years later, in 1994, to construct the LHC in the LEP tunnel [9] and the
615 approval of the 4 main experiments that would take place at the 4 interaction points would come in
616 1997 [10] and 1998 [11]:

- 617 • ALICE [12] has been designed in the purpose of studying quark-gluon plasma that is believed
618 to have been a state of matter that existed in the very first moment of the universe.
- 619 • ATLAS [13] and CMS [14] are general purpose experiments that have been designed with
620 the goal of continuing the exploration of the Standard Model and investigate new physics.
- 621 • LHCb [15] has been designed to investigate the preference of matter over antimatter in the
622 universe through the CP violation.

623 These large scale experiments, as well as the full CERN accelerator complex, are displayed on
624 Figure 2.1.

CERN's Accelerator Complex

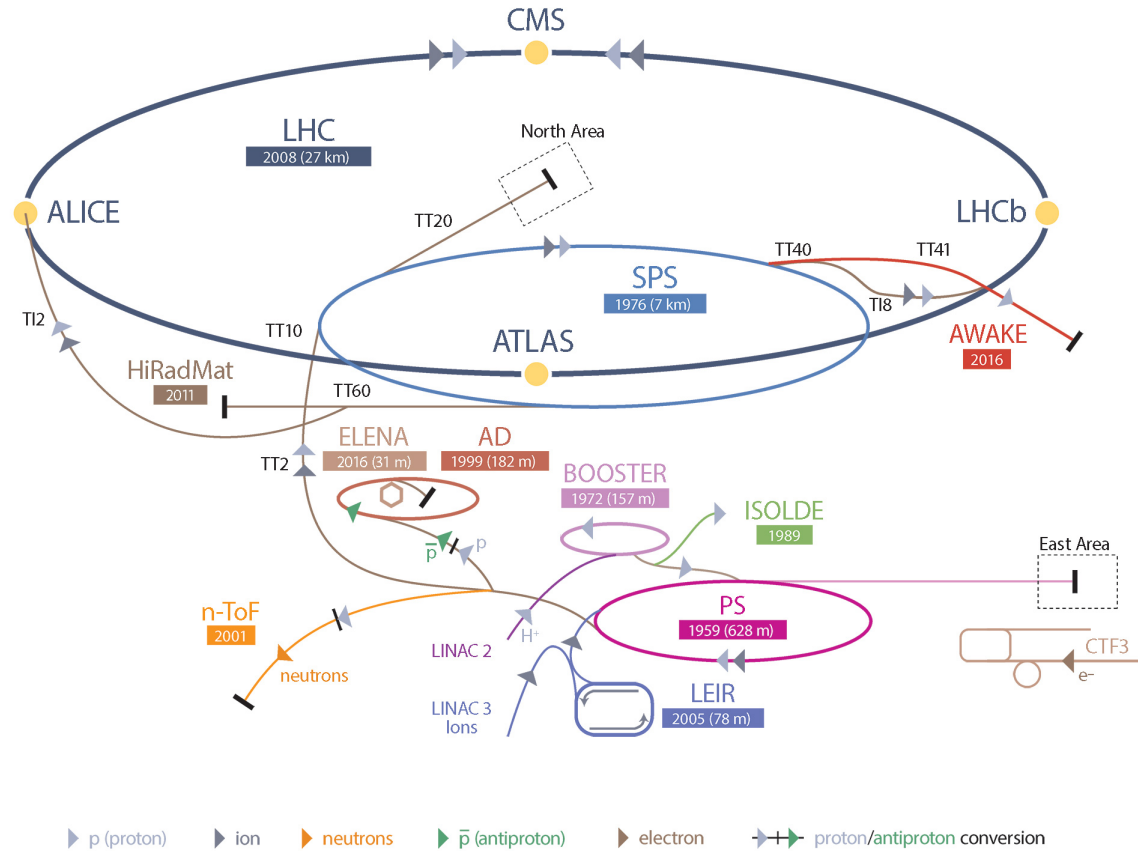


Figure 2.1: CERN accelerator complex.

The LHC is a 27 km long hadron collider and the most powerful accelerator used for particle physics since 2008 [16]. The LHC was originally designed to collide protons at a center-of-mass energy of 14 TeV and luminosity of $10^{34} \text{ cm}^{-2}\text{s}^{-1}$, as well as Pb ions at a center-of-mass energy of 2.8 TeV/A with a peak luminosity of $10^{27} \text{ cm}^{-2}\text{s}^{-1}$. Run 1 of LHC, when the center-of-mass energy only was half of the nominal LHC energy, was enough for both CMS and ATLAS to discover the Higgs boson [17] and for LHCb to discover pentaquarks [18] and confirm the existence of tetraquarks [19]. Nevertheless, after the Third Long Shutdown (LS3) (2024-2026), the accelerator will be in the so called High Luminosity LHC (HL-LHC) configuration [20], increasing its instantaneous luminosity to $10^{35} \text{ cm}^{-2}\text{s}^{-1}$ for pp collisions and to $4.5 \times 10^{27} \text{ cm}^{-2}\text{s}^{-1}$, boosting the discovery potential of the LHC.

2.2.1.1 Particle acceleration

The LHC is the last of a long series of accelerating devices. Before being accelerated by the LHC, the particles need to pass through different acceleration stages. All these acceleration stages are

638 visible on Figure 2.1 and pictures of the accelerators are showed in Figure 2.2.

639

640 The story of accelerated protons at CERN starts with a bottle of hydrogen gas injected into the
641 source chamber of the linear particle accelerator *LINAC 2* in which a strong electric field strips the
642 electron off the hygrodien molecules only to keep their nuclei, the protons. The cylindrical conductors,
643 alternatively positively or negatively charged by radiofrequency cavities, accelerate protons by
644 pushing them from behing and pulling them from the front and ultimately give them an energy of
645 50 MeV, increasing their mass by 5% in the process.

646

647 When exiting the LINAC 2, the protons are divided into 4 bunches and injected into the 4 su-
648 perimposed synchrotron rings of the *Booster* where they are then accelerated to reach an energy of
649 1.4 GeV before being injected into the *PS*. Before the Booster was operational in 1972, the protons
650 were directly injected into the PS from the LINAC 2 but the low injection energy limited the amount
651 of protons that could be accelerated at once by the PS. With the Booster, the PS accepts approxi-
652 mately 100 times more particles.

653

654 The 4 proton bunches are thus sent as one to the PS where their energy eventually reaches
655 26 GeV. Since the 70s, the main goal of this 628 m circumference synchrotron has been to sup-
656 ply other machines with accelerated particles. Nowadays, not only the PS accelerates protons, it also
657 accelerates heavy ions from the *Low Energy Ion Ring (LEIR)*. Indeed, the LHC experiments are not
658 only designed to study *pp*-collisions but also *Pb*-collisions. Lead is first injected into the dedicated
659 linear collider *LINAC 3*, that accelerate the ions using the same principle than LINAC 2. Electrons
660 are striped off the lead ions all along the acceleration process and eventually, only bare nuclei are
661 injected in the LEIR whose goal is to transform the long ion pulses received into short dense bunches
662 for LHC. Ions injected and stored in the PS were aceelerated by the LEIR from 4.2 MeV to 72 MeV.

663

664 Directly following the PS, is finally the last acceleration stage before the LHC, the 7 km long
665 *SPS*. The SPS accelerates the protons to 450 GeV and inject proton in both LHC accelerator rings
666 that will increase their energy up to 7 TeV. When the LHC runs with heavy lead ions for ALICE
667 and LHCb, ions are injected and accelerated to reach the energy of 2.8 TeV/A.

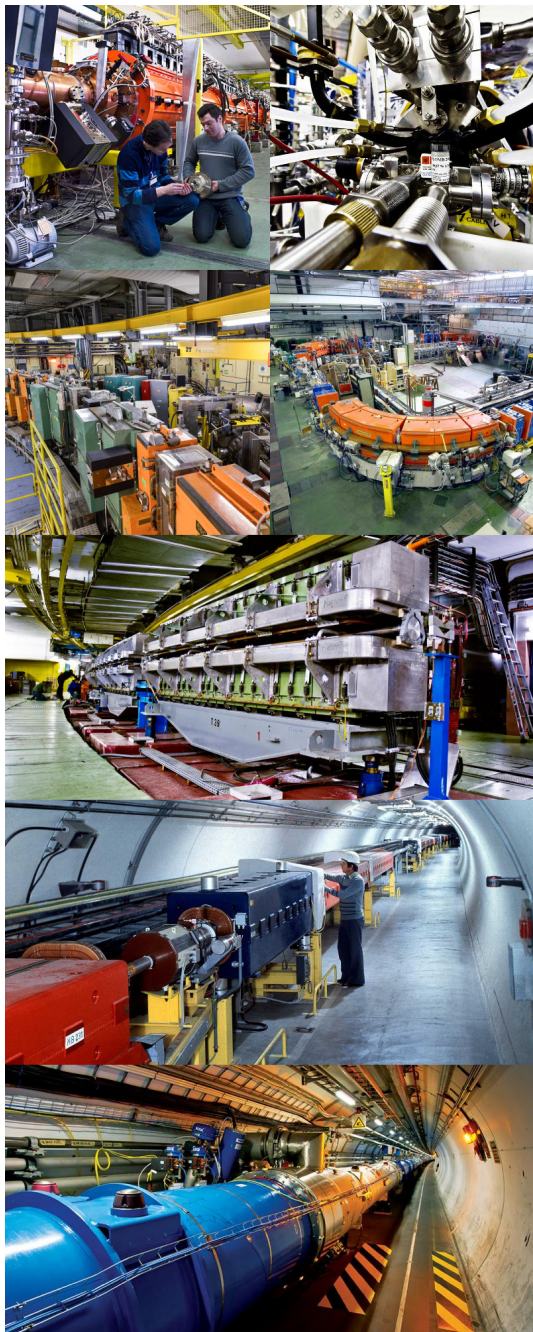


Figure 2.2: Pictures of the different accelerators. From top to bottom: first the LINAC 2 and the Pb source of LINAC 3. Then the Booster and the LEIR. Finally, the PS, the SPS and the LHC.

668 The LHC beams are not continuous and are rather organised in bunches of particles. When in pp -
 669 collision mode, the beams are composed of 2808 bunches of 1.15×10^{11} protons separated by 25 ns.
 670 When in Pb collision mode, the 592 Pb bunches are on the contrary composed of 2.2×10^8 ions
 671 separated by 100 ns. The two parallel proton beams of the LHC are contained in a single twin-

bore magnet due to the space restriction in the LEP tunnel. Indeed, building 2 completely separate accelerator rings next to each other was impossible. The dipoles of the 1232 twin-bore magnets are showed in Figure 2.3 alongside the magnetic field generated along the dipole section to accelerate the particles. The dipoles generate a nominal field of 8.33 T, needed to give protons and lead nucleons their nominal energy. Some 392 quadrupoles, presented in Figure 2.4, are also used to focus the beams, as well as other multipoles to correct smaller imperfections.

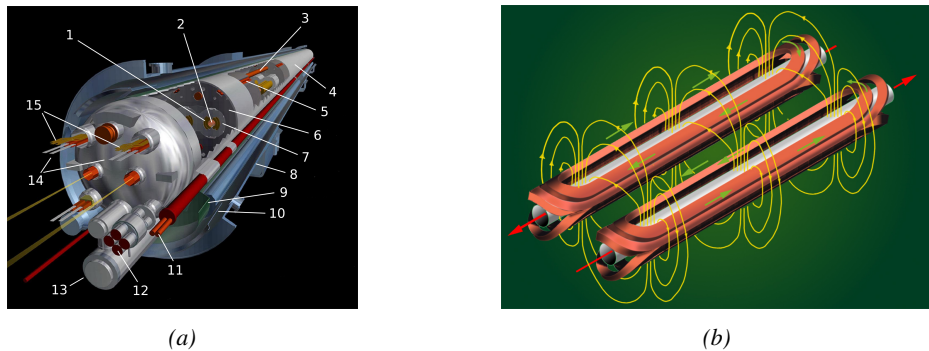


Figure 2.3: Figure 2.3a: schematics of the LHC cryodipoles. 1: Superconducting Coils, 2: Beam pipe, 3: Heat exchanger Pipe, 4: Helium-II Vessel, 5: Superconducting Bus-bar, 6: Iron Yoke, 7: Non-Magnetic Collars, 8: Vacuum Vessel, 9: Radiation Screen, 10: Thermal Shield, 11: Auxiliary Bus-bar Tube, 12: Instrumentation Feed Throughs, 13: Protection Diode, 14: Quadrupole Bus-bars, 15: Spool Piece Bus-bars. Figure 2.3b: magnetic field and resulting motion force applied on the beam particles.

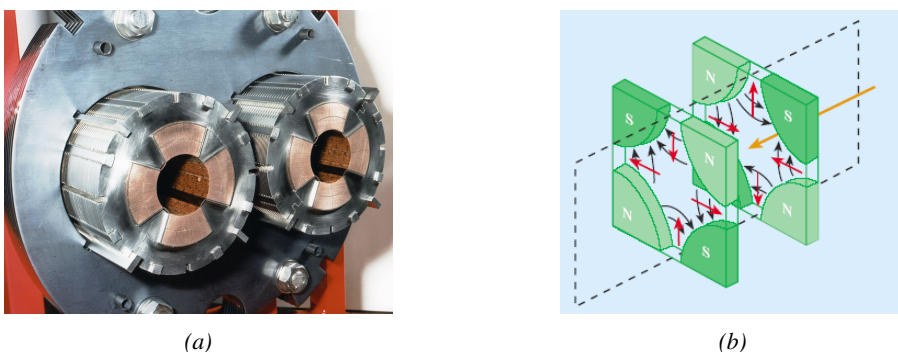


Figure 2.4: Figure 2.4a: picture of the LHC quadrupoles. Figure 2.4b: magnetic fields and resulting focussing force applied on the beam by 2 consecutive quadrupoles.

678 2.2.1.2 LHC discoveries and LHC physics program

679 The very first proton beam successfully circulated in the LHC in September 2008 directly followed
680 by an incident leading to mechanical damage that would delay the LHC program for a year until
681 November 2009.

682 **2.2.1.3 High Luminosity LHC**

683 **2.2.2 CMS, a multipurpose experiment**

684 **2.3 Muon Phase-II Upgrade**

685 After the more than two years lasting First Long Shutdown (LS1), the Large Hadron Collider (LHC)
 686 delivered its very first Run-II proton-proton collisions early 2015. LS1 gave the opportunity to the
 687 LHC and to the its experiments to undergo upgrades. The accelerator is now providing collisions
 688 at center-of-mass energy of 13 TeV and bunch crossing rate of 40 MHz, with a peak luminosity
 689 exceeding its design value. During the first and upcoming second LHC Long Shutdown, the Compact
 690 Muon Solenoid (CMS) detector is also undergoing a number of upgrades to maintain a high system
 691 performance [21].

692 From the LHC Phase-2 or High Luminosity LHC (HL-LHC) period onwards, i.e. past the Third
 693 Long Shutdown (LS3), the performance degradation due to integrated radiation as well as the average
 694 number of inelastic collisions per bunch crossing, or pileup, will rise substantially and become a
 695 major challenge for the LHC experiments, like CMS that are forced to address an upgrade program
 696 for Phase-II [22]. Simulations of the expected distribution of absorbed dose in the CMS detector
 697 under HL-LHC conditions, show in figure 4.16 that detectors placed close to the beamline will have
 698 to withstand high irradiation, the radiation dose being of the order of a few tens of Gy.

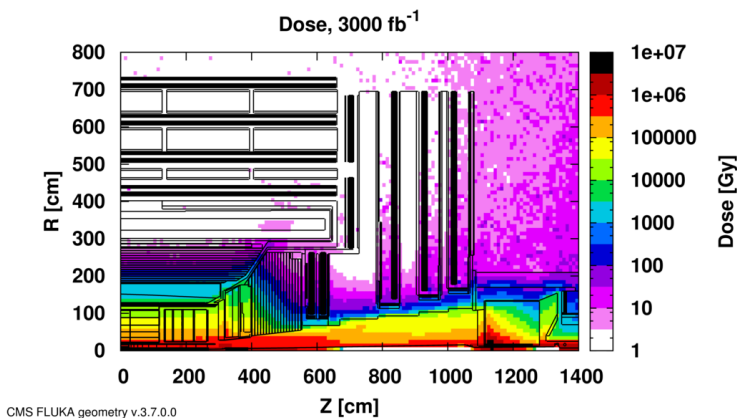


Figure 2.5: Absorbed dose in the CMS cavern after an integrated luminosity of 3000 fb. R is the transverse distance from the beamline and Z is the distance along the beamline from the Interaction Point at Z=0.

699 The measurement of small production cross-section and/or decay branching ratio processes, such
 700 as the Higgs boson coupling to charge leptons or the $B_s \rightarrow \mu^+ \mu^-$ decay, is of major interest and
 701 specific upgrades in the forward regions of the detector will be required to maximize the physics
 702 acceptance on the largest possible solid angle. To ensure proper trigger performance within the
 703 present coverage, the muon system will be completed with new chambers. In figure 2.6 one can
 704 see that the existing Cathode Strip Chambers (CSCs) will be completed by Gas Electron Multipliers
 705 (GEMs) and Resistive Plate Chambers (RPCs) in the pseudo-rapidity region $1.6 < |\eta| < 2.4$ to
 706 complete its redundancy as originally scheduled in the CMS Technical Proposal [23].

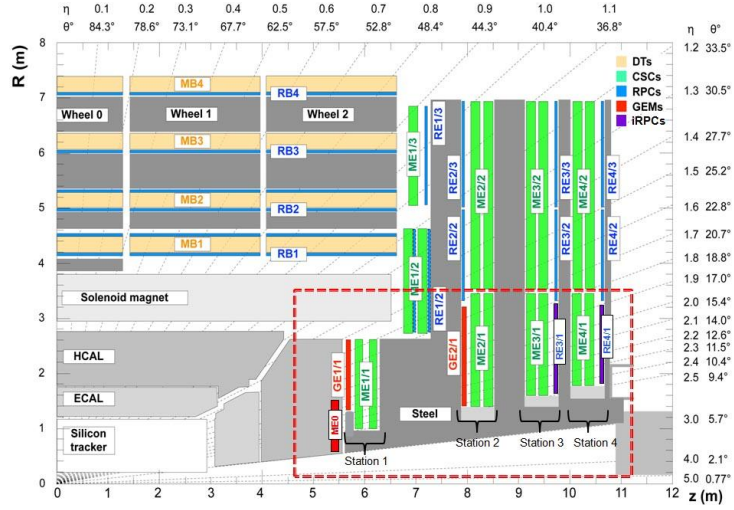


Figure 2.6: A quadrant of the muon system, showing DTs (yellow), RPCs (light blue), and CSCs (green). The locations of new forward muon detectors for Phase-II are contained within the dashed box and indicated in red for GEM stations (ME0, GE1/1, and GE2/1) and dark blue for improved RPC (iRPC) stations (RE3/1 and RE4/1).

707 RPCs are used by the CMS first level trigger for their good timing performances. Indeed, a very
 708 good bunch crossing identification can be obtained with the present CMS RPC system, given their
 709 fast response of the order of 1 ns. In order to contribute to the precision of muon momentum mea-
 710 surements, muon chambers should have a spatial resolution less or comparable to the contribution
 711 of multiple scattering [21]. Most of the plausible physics is covered only considering muons with
 712 $p_T < 100$ GeV thus, in order to match CMS requirements, a spatial resolution of $\mathcal{O}(\text{few mm})$ the
 713 proposed new RPC stations, as shown by the simulation in figure 2.7. According to preliminary
 714 designs, RE3/1 and RE4/1 readout pitch will be comprised between 3 and 6 mm and 5 η -partitions
 715 could be considered.

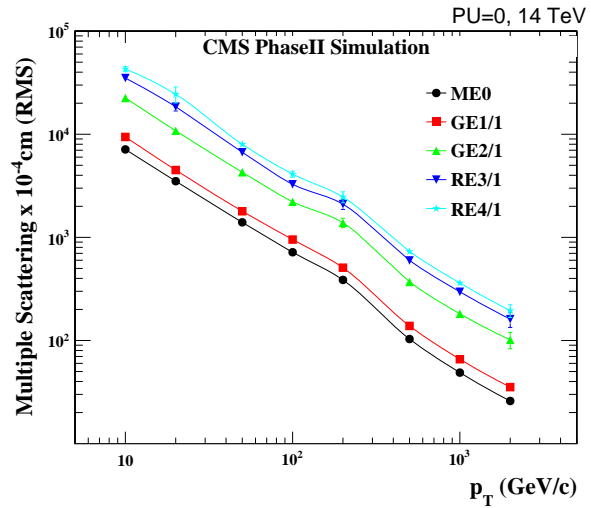


Figure 2.7: RMS of the multiple scattering displacement as a function of muon p_T for the proposed forward muon stations. All of the electromagnetic processes such as bremsstrahlung and magnetic field effect are included in the simulation.

3

716

717

Physics of Resistive plate chambers

718 A Resistive Plate Chamber (RPC) is a gaseous detector using the same physical processes described
719 in Chapter 3. It has been developed in 1981 by Santonico and Cardarelli [24], under the name of
720 *Resistive Plate Counter*, as an alternative to the local-discharge spark counters proposed in 1978
721 by Pestov and Fedotovich [25, 26]. Working with spark chambers implied using high-pressure gas
722 and high mechanical precision which the RPC simplified by formerly using a gas mixture of argon
723 and butane flowed at atmospheric pressure and a constant and uniform electric field propagated
724 in between two parallel electrode plates. Moreover, a significant increase in rate capability was
725 introduced by the use of electrode plate material with high bulk resistivity, preventing the discharge
726 from growing throughout the whole gas gap. Indeed, the effect of using resistive electrodes is that
727 the constant electric field is locally canceled out by the development of the discharge, limiting its
728 growth.

729 Through its development history, different operating modes [27–29] and new detector designs [30–
730 32] have been discovered, leading to further improvement of the rate capability of such a detector.
731 Moreover, the addition of SF_6 into the gas mix improved the stability of operation of the RPC [33,
732 34].

733 The low developing costs and easily achievable large detection areas offered by RPCs, as well as
734 the wide range of possible designs, made them a natural choice to as muon chambers and/or trigger
735 detectors in multipurpose experiments such as CMS [21] or ATLAS [35], time-of-flight detectors in
736 ALICE [36], calorimeter with CALICE [37] or even detectors for volcanic muography with ToMu-
737 Vol [38].

738 3.1 Principle

739 RPCs are ionisation detectors composed of two parallel resistive plate electrodes in between which
740 a constant electric field is set. The space in between the electrodes, referred as *gap*, is filled with a
741 dense gas that is used to generate primary ionization into the gas volume. The free charge carriers
742 (electrons and cations) created by the ionization of the gas molecules are then accelerated towards

743 the electrodes by the electric field, as shown in Figure 3.1 [39].

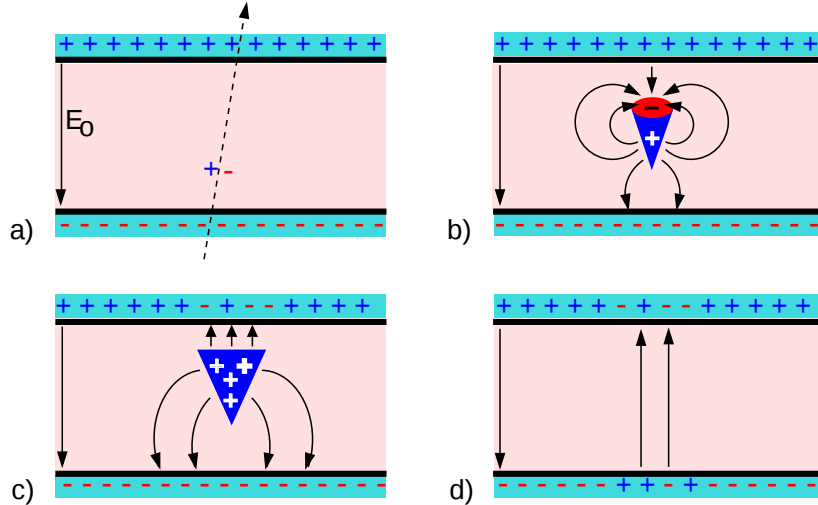


Figure 3.1: Different phases of the avalanche development in the RPC gas volume subjected to a constant electric field E_0 . a) An avalanche is initiated by the primary ionisation caused by the passage of a charged particle through the gas volume. b) Due to its growing size, the avalanche starts to locally influence the electric field. c) The electrons, lighter than the cations reach the anode first. d) The ions reach the cathode. While the charges have not recombined, the electric field in the small region around the avalanche stays affected and locally blind the detector.

744 RPCs being passive detectors, a current on pick-up copper read-out placed outside of the gas
 745 volume is induced by the charge accumulation during the growth of the avalanche. As a result,
 746 the time resolution of the detector is substantially increased as the output signal is generated while
 747 the electrons are still in movement. The advantage of a constant electric field, over multi-wire
 748 proportional chambers, is that the electrons are being fully accelerated from the moment charge
 749 carriers are freed and feel the full strength of the electric field that doesn't depend on the distance to
 750 the readout and that the output signal doesn't need for the electrons to be physically collected.

751 The typical gas mixture RPCs are operated with is generally composed of 3 gas compounds.

- 752 • Tetrafluoroethane ($C_2F_4H_2$), also referred to as *Freon*, is the principal compound of the RPC
 753 gas mixtures, with a typical fraction above 90%. It is used for it's high effective Townsend
 754 coefficient and the great average fast charge that allows to operate the detector with a high
 755 threshold with respect to argon, for example, that has similar effective Townsend coefficient
 756 but suffers from a lower fast charge. To operate with similar conditions, argon would require a
 757 higher electric field leading to a higher fraction of streamers, thus limiting the rate capability
 758 of the detector [40].
- 759 • Isobutane (i- C_4H_{10}), only present in a few percent in the gas mixtures, is used for its UV
 760 quenching properties [41] helping to prevent streamers due to UV photon emission during the
 761 avalanche growth.
- 762 • Sulfur hexafluoride, (SF_6), referred to simply as *SF6*, is used in very little quantities for its
 763 high electronegativity. Excess of electrons are being absorbed by the compound and streamers

are suppressed [34]. Nevertheless, a fraction of SF_6 higher than 1% will not bring any extra benefit in terms of streamer cancelation power but will lead to higher operating voltage [33], as can be understood through Figure 3.2.

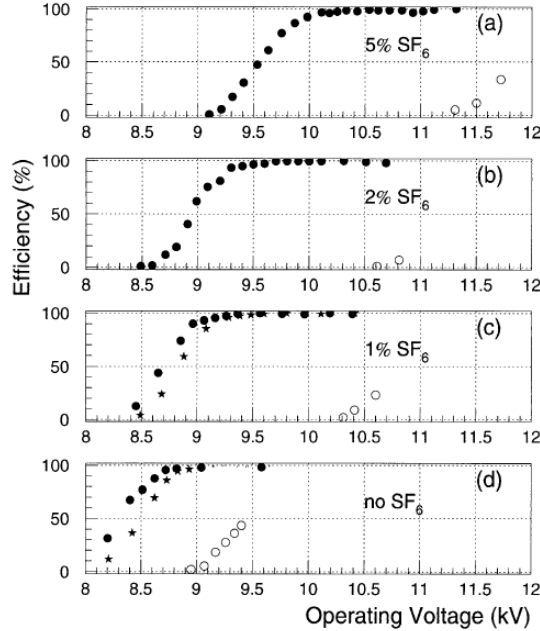


Figure 3.2: Effeciency (circles and stars with 30 mV and 100 mV thresholds respectively) and streamer probability (opened circles) as function of the operating voltatge of a 2 mm single gap HPL RPC flushed with a gas mixture containing (a) 5%, (b) 2%, (c) 1% and (d) no SF_6 [33].

After an avalanche developed in the gas, a time long compared to the development of a discharge is needed to recombine the charge carriers in the electrode material due to their resistivity. This property has the advantage of affecting the local electric field and avoiding sparks in the detector but, on the other hand, the rate capability is intrinsically limited by the time constant τ_{RPC} of the detector. Using a quasi-static approximation of Maxwell's equations for weakly conducting media, it can be shown that the time constant τ_{RPC} necessary to the charge recombination at the interface in between the electrode and the gas volume is given by the Formula 3.1 [42].

$$\tau_{RPC} = \frac{\epsilon_{electrode} + \epsilon_{gas}}{\sigma_{electrode} + \sigma_{gas}} \quad (3.1)$$

A gas can be assimilated to vacuum, leading to $\epsilon_{gas} = \epsilon_0$ and $\sigma_{gas} = 0$, and the electrodes permittivity and conductivity can be written as $\epsilon_{electrode} = \epsilon_r \epsilon_0$ and $\sigma_{electrode} = 1/\rho_{electrode}$, showing the strong dependence of the time constant to the electrodes resistivity in Formula 3.2.

$$\tau_{RPC} = (\epsilon_r + 1)\epsilon_0 \times \rho_{electrode} \quad (3.2)$$

Very few materials with a low enough resistivity exist in nature. The resistivity targeted to build RPCs ranges from 10^9 to $10^{12} \Omega \cdot \text{cm}$. The most common RPC electrode materials are displayed in Table 3.1. When the doped glass and ceramics can offer short time constants of the order of 1 ms,

780 the developing cost of such materials is quite high due to the very low demand. Thus, High-pressure
 781 laminate (HPL) is often the choice for high rate experiments using very large RPC detection areas.
 782 Other experiments working at cosmic muon fluxes can safely operate with ordinary float glass.

Material	$\rho_{electrode}$ ($\Omega \cdot \text{cm}$)	ϵ_r	τ_{RPC} (ms)
Float glass	10^{12}	~ 7	~ 700
High-pressure laminate	10^{10} to 10^{12}	~ 6	~ 6 to 600
Doped glass (LR S)	10^9 to 10^{11}	~ 10	~ 1 to 100
Doped ceramics (SiN/SiC)	10^9	~ 8.5	~ 1
Doped ceramics (Ferrite)	10^8 to 10^{12}	~ 20	~ 0.2 to 2000

Table 3.1: Properties of the most used electrode materials for RPCs.

783 3.1.1 Electron drift velocity

784 Talk about the electron drift velocity and mention the time resolution of RPCs.

785 3.2 Rate capability and time resolution of Resistive Plate Cham- 786 bers

787 As already previously discussed, the electrode material plays a key role in the max intrinsic rate
 788 capability of RPCs. R&D is being done to develop at always cheaper costs material with lower
 789 resistivity. Nevertheless, the amount of charge released, i.e. the size of the discharge, if reduced
 790 leads to a smaller blind area in the detector, increasing the rate capability of the detector.

791 3.2.1 Operation modes

792 RPCs where developed early 1980s. At that time it was using an operating mode now referred to
 793 as *streamer mode*. Streamers are large discharges that develop in between the 2 electrodes enough
 794 to locally discharge the electrodes. If the electric field inside of the gas volume is strong enough,
 795 with electrons being fast compared to ions, a large and dense cloud of positive ions will develop
 796 nearby the anode and extend toward the cathode while the electrons are being collected, eventually
 797 leading to a streamer discharge due to the increase of field seen at the cathode. the field is then strong
 798 enough so that electrons are pulled out of the cathode. Electrodes, though they are a unique volume
 799 of resistive material, can be assimilated to capacitors. At the moment an electric field is applied in
 800 between their outer surfaces, the charge carriers inside of the volume will start moving leading to
 801 a situation where there is no voltage across the electrodes and a higher density of negative charges,
 802 i.e. electrons, on the inner surface of the cathode. Finally, when a streamer discharge occurs, these
 803 electrons are partially released in the gas volume contributing to increase the discharge strength until
 804 the formation of a conductive plasma, the streamer. This can be understood through Figure 3.3 [27].
 805 Streamer signals are very convenient in terms of read-out as no amplification is required with output
 806 pulses amplitudes of the order of a few tens to few hundreds of mV as can be seen on Figure 3.4.

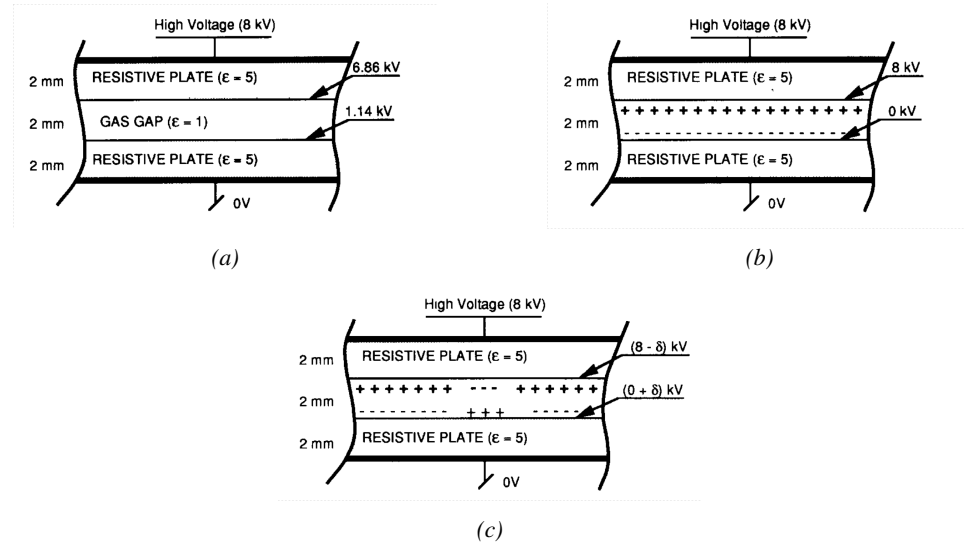


Figure 3.3: Movement of the charge carriers in an RPC. Figure 3.3a: Voltage across an RPC whose electrode have a relative permittivity of 5 at the moment the tension is applied. Figure 3.3b: After the charge carriers moved, the electrodes are charged and there is no voltage drop over the electrodes anymore. The full potential is applied on the gas gap only. Figure 3.3c: The streamer discharge initiated by a charged particle transports electrons and cations towards the anode and cathode respectively.

When the electric field is reduced though, the electronic gain is small until the electrons get close enough to the anode and the positive ion cloud is much smaller. The electric field cannot rise to the point a field emission of electrons on the cathode is possible. The resulting signal is weak, of the order of a few mv as shown on Figure 3.4, and requires amplification. This is the *avalanche mode* of RPC operation.

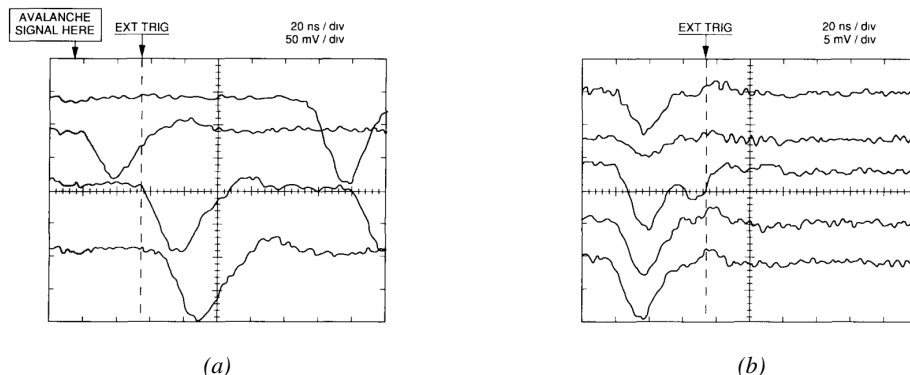


Figure 3.4: Typical oscilloscope pulses in streamer mode (Figure 3.4a) and avalanche mode (Figure 3.4b). In the case of streamer mode, the very small avalanche signal is visible.

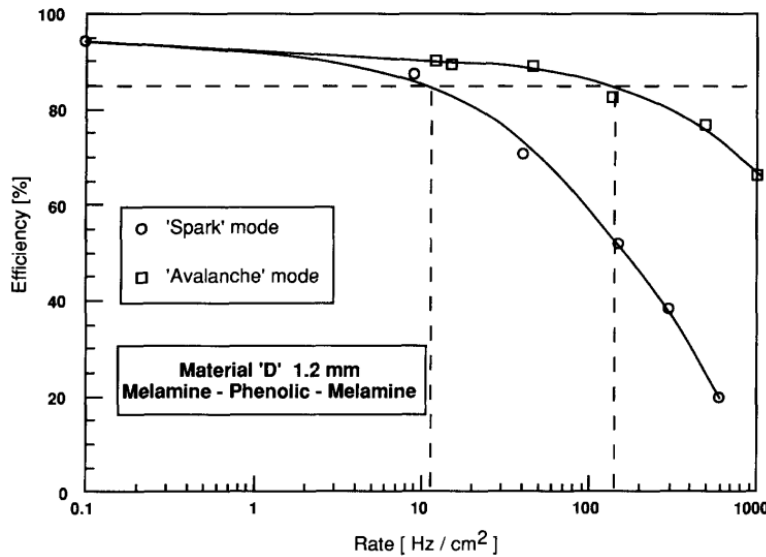


Figure 3.5: Rate capability comparison for the streamer and avalanche mode of operation. An order of magnitude in rate capability for a maximal efficiency drop of 10% is gained by using the avalanche mode over the streamer mode.

This mode offers a higher rate capability by providing smaller discharges that don't affect the electrodes charge and are more locally contained in the gas volume as was demonstrated by Crotty with Figure 3.5 [27]. The detector only stays locally blind the time the charge carriers are recombined and there is no need for electrode recharge which is a long process affecting a large portion of the detector. Another advantage of avalanche signals over streamer is the great time consistency. Figure 3.4 shows very clearly that avalanche signals have a very small time jitter. This is a natural choice for high rate experiments.

3.2.2 Detector designs and performance

Different RPC design have been used and each of them present its own advantages. Historically, the first type of RPC to have been developed is what is referred now to *narrow gap* RPC [24, 43]. After the avalanche mode has been discovered [27], it has been proven that increasing the width of the gas gap lead to higher rate capability, due to lower charge deposition per avalanche, and lower power dissipation [43]. Nevertheless, by increasing the gas gap width, the time resolution of the detector decreases. This is a natural result if the increase of active gas volume in the detector is taken into account. Indeed, for a given threshold, only the small fraction of gas closest to the cathode will provide enough gain to have a detectable signal. In the case of a wider gas volume, the active region is then larger and a larger time jitter is introduced with the variation of starting position of the avalanche, as discussed in [30]. To solve improve both the time resolution and the rate capability, different methods were used trying to get advantages of both narrow and wide gap RPCs.

831 **3.2.2.1 Double-gap RPC**

832 Double-gap RPCs are made out of 2 narrow RPC detectors. The 2 RPC gaps are stacked on top of
 833 each other as shown in Figure 3.6. This detector layout, popularized by the two multipurpose experiments
 834 CMS [21] and ATLAS [35] at LHC, can be used as an OR system in which each individual
 835 chamber participates in the output signal. The gain of such a detector is greatly reduced with respect
 836 to single-gap RPCs with an efficiency plateau reached at lower voltage, as visible on Figure 3.7.

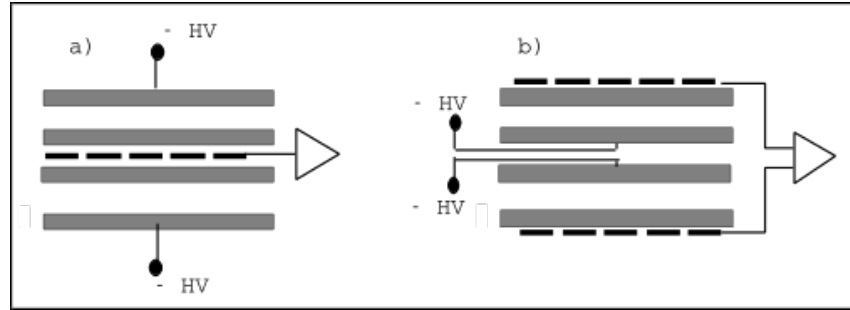


Figure 3.6: Possible double-gap RPC layouts: a) "standard" 1D double-gap RPC, as used in CMS experiment, where the anodes are facing each other and a 1D read-out plane is sandwiched in between them, b) double read-out double-gap RPC as used in ATLAS experiment, where the cathodes are facing each other and 2 read-out planes are used on the outer surfaces. This last layout can offer the possibility to use a 2D reconstruction by using orthogonal read-out planes.

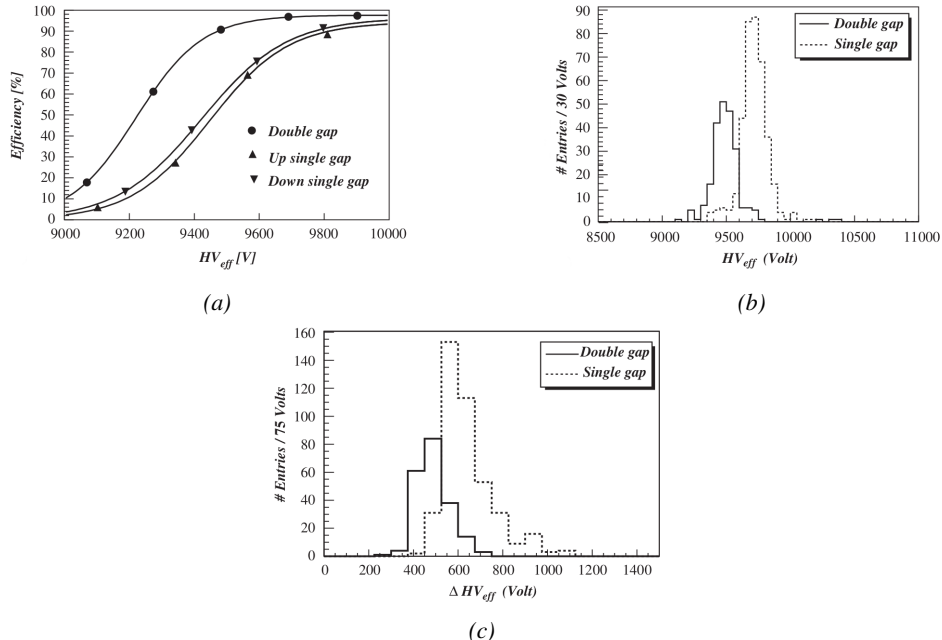


Figure 3.7: Comparison of performance of CMS double and single gap RPCs using cosmic muons [44]. Figure 3.7a: Comparison of efficiency sigmoids. Figure 3.7b: Voltage distribution at 95% of maximum efficiency. Figure 3.7c: $\Delta_{10\%}^{90\%}$ distribution.

837 **3.2.2.2 Multigap RPC (MRPC)**

838 MRPCs are layouts in which floating sub electrode plates are placed into a wide gap RPC to divide
 839 the gas volume and create a sum of narrow gaps [30, 31]. The time resolution of such a detector can
 840 reach of few tens of ps, with gas gaps of the order of a few hundred μm as shown in Figure 3.8
 841 representing ALICE Time-of-flight (ToF) MRPCs.

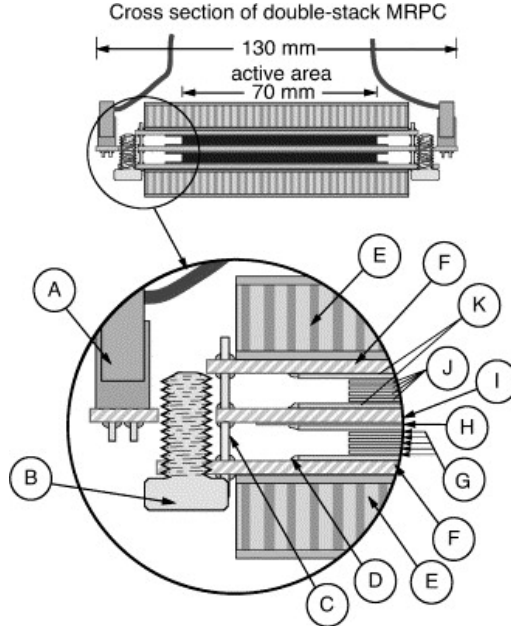


Figure 3.8: Presentation of ALICE MRPC using $250 \mu\text{m}$ gas gaps, $620 \mu\text{m}$ outer glass electrodes and $550 \mu\text{m}$ inner floating electrodes. More details on the labels are given in [45].

842 Sometimes used as a double multigap RPC, taking advantage of the OR of double gap RPCs,
 843 the MRPC is mainly used as ToF detector [45–49] due to its excellent timing properties that allow
 844 to perform particle identification as explained by Williams in [50]. The principle of particle iden-
 845 tification using ToF is simply the measurement of the velocity of a particle. Indeed, particles are
 846 defined by their mass (for the parameter of interest here, their electric charge being measured using
 847 the bending angle of the particles traveling through a magnetic field) and this mass can be calculated
 848 by measuring the velocity β and momentum of the particle:

$$\beta = \frac{p}{\sqrt{p^2 + m^2}} \quad (3.3)$$

849 Intuitively, it is trivial to understand that 2 different particles having the same momentum will
 850 have a different velocity due to the mass difference and thus a different flight time T_1 and T_2 through
 851 the detector and this is used to separate and identify particles. The better the time resolution of the
 852 ToF system used, the stronger will the separation be:

$$T = \frac{L}{v} = \frac{L}{c \cdot \beta}, \quad \Delta T = T_1 - T_2 = \frac{L}{c} \left(\sqrt{1 + m_1^2/p^2} - \sqrt{1 + m_2^2/p^2} \right) \cong (m_1^2 - m_2^2) \frac{L}{2cp^2} \quad (3.4)$$

853 An example of particle identification is given for the case of STAR experiment in Figure 3.9.

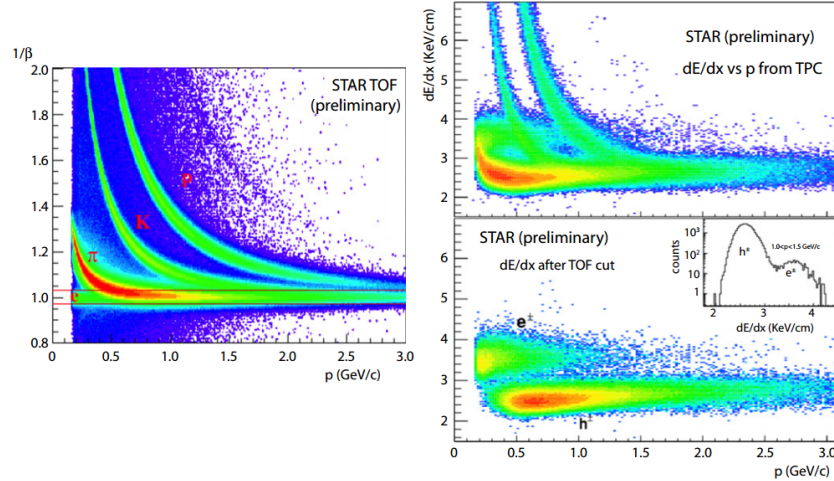


Figure 3.9: Particle identification applied to electrons in the STAR experiment. The identification is performed combining ToF and dE/dx measurements [50].

854 Another benefice of using such small gas gaps is the strong reduction of the average avalanche
855 volume and thus of the blind spot on MRPCs leading to an improved rate capability. Multigaps can
856 sustain backgrounds of several kHz/cm² as demonstrated in Figure 3.10.

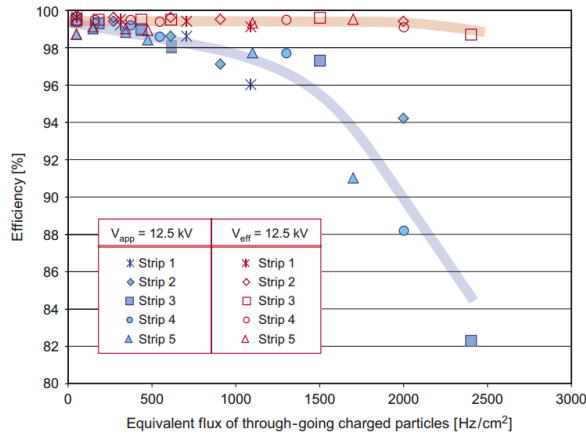


Figure 3.10: Comparison of the detector performance of ALICE ToF MRPC [51] at fixed applied voltage (in blue) and at fixed effective voltage (in red). The effective voltage is kept fixed by increasing the applied voltage accordingly to the current drawn by the detector.

857 3.2.2.3 Charge distribution and performance limitations

858 The direct consequence of the different RPC layouts is a variation of intrinsic time resolution of the
859 RPC as the gap size decreases. An advantage is given to multigaps whose design use sub-millimeter
860 gas volumes providing very consistent signals.

861 On the charge spectrum point of view, each layout has its own advantages. When the double-gap
 862 has the highest induced over drifting charge ratio, as seen in Figure 3.11, the multigap has a charge
 863 spectrum strongly detached from the origin, as visible in Figure 3.12. A high induced over drifting
 864 charge ratio means that the double gap can be safely operated at high threshold or that at similar
 865 threshold it can be operated with a twice smaller drifting charge, meaning a higher rate capability.
 866 On the other hand, the strong detachment of the charge spectrum from the origin in the MRPC case
 867 allows to reach a higher efficiency with increasing threshold as most of the induced charge is not low
 868 due to the convolution of several single gap spectra. The range of stable efficiency increases with
 869 the number of gap, as presented in Figure 3.13.

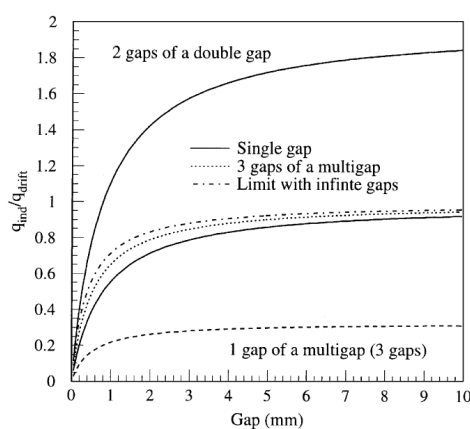


Figure 3.11: Ratio between total induced and drifting charge have been simulated for single gap, double-gap and multigap layouts [52]. The total induced charge for a double-gap RPC is a factor 2 higher than for a multigap.

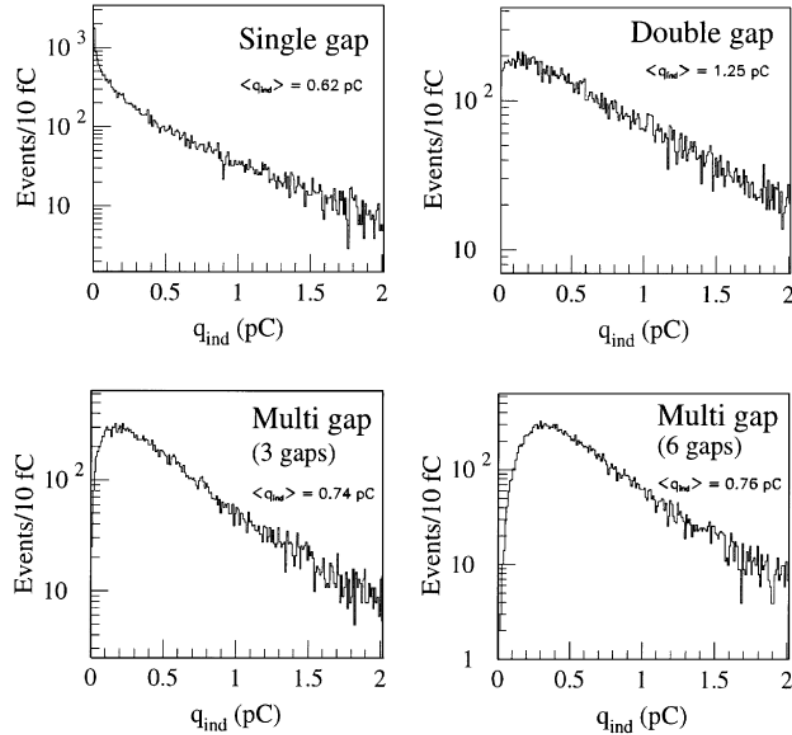


Figure 3.12: Charge spectra have been simulated for single gap, double-gap and multigap layouts [52]. It appears that when single gap shows a decreasing spectrum, double and multigap layouts exhibit a spectrum whose peak is detached from the origin. The detachment gets stronger as the number of gaps increases.

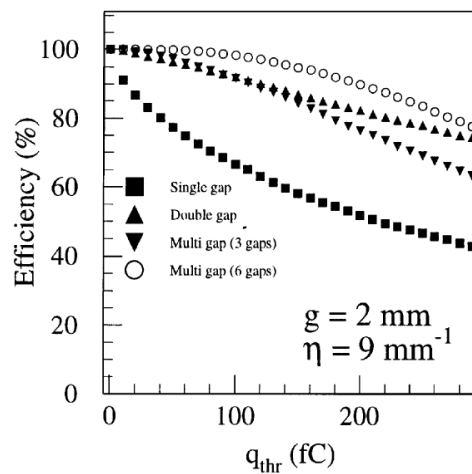


Figure 3.13: The maximal theoretical efficiency is simulated for single gap, double-gap and multigap layouts [52] at a constant gap thickness of 2 mm and using an effective Townsend coefficient of 9 mm^{-1} .

⁸⁷⁰ **3.3 Signal formation**

⁸⁷¹ **3.4 Gas transport parameters**

4

872

873

874

Longevity studies and Consolidation of the present CMS RPC subsystem

875 4.1 Resistive Plate Chambers at CMS

876 4.1.1 Overview

877 The Resistive Plate Chambers (RPC) system, located in both barrel and endcap regions, provides a
878 fast, independent muon trigger with a looser p_T threshold over a large portion of the pseudorapidity
879 range ($|\eta| < 1.6$) [add reconstruction].

880

881 During High-Luminosity LHC (HL-LHC) operations the expected conditions in terms of back-
882 ground and pile-up will make the identification and correct P_T assignment a challenge for the Muon
883 system. The goal of RPC upgrade is to provide additional hits to the Muon system with precise tim-
884 ing. All these informations will be elaborated by the trigger system in a global way enhancing the
885 performance of the trigger in terms of efficiency and rate control. The RPC Upgrade is based on two
886 projects: an improved Link Board System and the extension of the RPC coverage up to $|\eta| = 2.4$.
887 [FIXME 2.4 or 2.5?]

888 The Link Board system, that will be described in section xxx, is responsible to process, syn-
889 chronize and zero-suppress the signals coming from the RPC front end boards. The Link Board
890 components have been produced between 2006 and 2007 and will be subjected to aging and failure
891 in the long term. The upgraded Link Board system will overcome the aging problems described in
892 section xxx and will allow for a more precise timing information to the RPC hits from 25 to 1 ns [ref
893 section xxx].

894 The extension of the RPC system up to $|\eta| = 2.1$ was already planned in the CMS TDR [ref
895 cmstdr] and staged because of budget limitations and expected background rates higher than the rate
896 capability of the present CMS RPCs in that region. An extensive R&D program has been done in
897 order to develop an improved RPC that fulfills the CMS requirements. Two new RPC layers in the
898 innermost ring of stations 3 and 4 will be added with benefits to the neutron-induced background

899 reduction and efficiency improvement for both trigger and offline reconstruction.

900 4.1.2 The present RPC system

901 The RPC system is organized in 4 stations called RB1 to RB4 in the barrel region, and RE1 to RE4
 902 in the endcap region. The innermost barrel stations, RB1 and RB2, are instrumented with 2 layers
 903 of RPCs facing the innermost (RB1in and RB2in) and outermost (RB1out and RB2out) sides of the
 904 DT chambers. Every chamber is then divided from the read-out point of view into 2 or 3 η partitions
 905 called “rolls”. The RPC system consist of 480 barrel chambers and 576 endcap chambers. Details
 906 on the geometry are discussed in the paper [ref to geo paper].

907 The CMS RPC chamber is a double-gap, operated in avalanche mode to ensure reliable operation
 908 at high rates. Each RPC gap consists of two 2-mm-thick resistive High-Pressure Laminate (HPL)
 909 plates separated by a 2-mm-thick gas gap. The outer surface of the HPL plates is coated with a thin
 910 conductive graphite layer, and a voltage is applied. The RPCs are operated with a 3-component,
 911 non-flammable gas mixture consisting of 95.2% freon ($C_2H_2F_4$, known as R134a), 4.5% isobutane
 912 ($i-C_4H_{10}$), and 0.3% sulphur hexafluoride (SF_6) with a relative humidity of 40% - 50%. Readout
 913 strips are aligned in η between the 2 gas gaps. [\[Add a sentence on FEBs.\]](#)

914 The discriminated signals coming from the Front End boards feed via twisted cables (10 to 20 m
 915 long) the Link Board System located in UXC on the balconies around the detector. The Link System
 916 consist of the 1376 Link Boards (LBs) and the 216 Control Boards (CBs), placed in 108 Link Boxes.
 917 The Link Box is a custom crate (6U high) with 20 slots (for two CBs and eighteen LBs). The Link
 918 Box contains custom backplane to which the cables from the chambers are connected, as well as the
 919 cables providing the LBs and CBs power supply and the cables for the RPC FEBs control with use
 920 of the I2C protocol (trough the CB). The backplane itself contains only connectors (and no any other
 921 electronic devices).

922 The Link Board has 96 input channels (one channel corresponds to one RPC strip). The input
 923 signals are the ~ 100 ns binary pulses which are synchronous to the RPC hits, but not to the LHC
 924 clock (which drives the entire CMS electronics). Thus the first step of the FEB signals processing
 925 is synchronization, i.e. assignment of the signals to the BXes (25 ns periods). Then the data are
 926 compressed with a simple zero-suppressing algorithm (the input channels are grouped into 8 bit
 927 partitions, only the partitions with at least one nonzero bit are selected for each BX). Next, the non-
 928 empty partitions are time-multiplexed i.e. if there are more than one such partition in a given BX,
 929 they are sent one-by-one in consecutive BXes. The data from 3 neighbouring LBs are concentrated
 930 by the middle LB which contains the optical transmitter for sending them to the USC over a fiber at
 931 1.6 Gbps.

932 The Control Boards provide the communication of the control software with the LBs via the
 933 FEC/CCU system. The CBs are connected into token rings, each ring consists of 12 CBs of one
 934 detector tower and a FEC mezzanine board placed on the CCS board located in the VME crate in
 935 the USC. In total, there are 18 rings in the entire Link System. The CBs also perform automatic
 936 reloading of the LB's firmware which is needed in order to avoid accumulation of the radiation
 937 induced SEUs in the LBs firmware.

938 Both LBs and CB are based on the Xilinx Spartan III FPGAs, the CB additionally contains
 939 radiation-tolerant (FLASH based) FPGA Actel ProAsicPlus.

940 The High Voltage power system is located in USC, not exposed to radiation and easily accessible
 941 for any reparation. A single HV channel powers 2 RPC chambers both in the barrel and endcap
 942 regions. The Low Voltage boards are located in UXC on the balconies and provide the voltage to the

⁹⁴³ front end electronics.

⁹⁴⁴ 4.1.3 Pulse processing of CMS RPCs

⁹⁴⁵ Signals induced by cosmic particle in the RPC strips are shaped by standard CMS RPC Front-End
⁹⁴⁶ Electronics (FEE) following the scheme of Figure 4.1. On a first stage, analogic signals are amplified
⁹⁴⁷ and then sent to the Constant Fraction Discriminator (CFD) described in Figure 4.2. At the end of
⁹⁴⁸ the chain, 100 ns long pulses are sent in the LVDS output. These output signal are sent on one side to
⁹⁴⁹ a V1190A Time-to-Digital Converter (TDC) module from CAEN and on the other to an OR module
⁹⁵⁰ to count the number of detected signals. Trigger and hit coïncidences are monitored using scalers.
⁹⁵¹ The TDC is used to store the data into ROOT files. These files are thus analysed to understand the
⁹⁵² detectors performance.

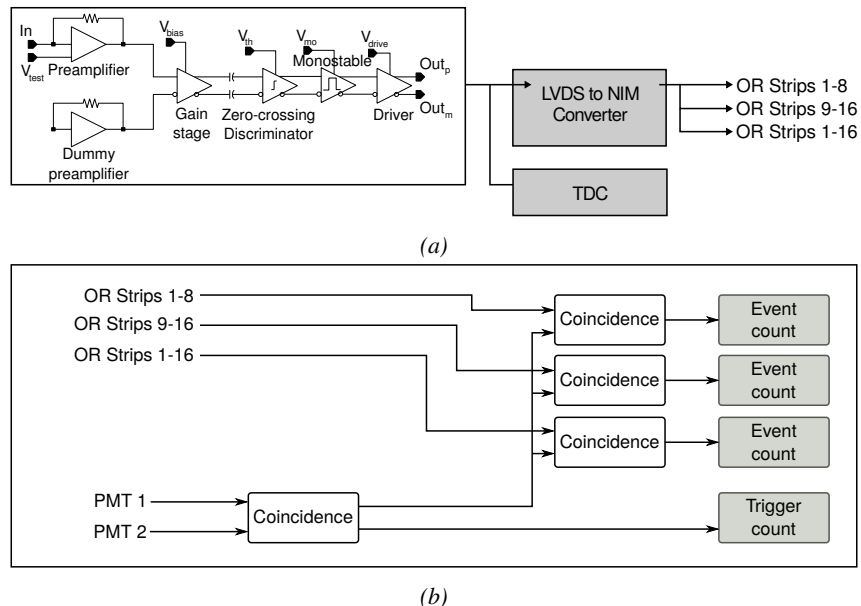


Figure 4.1: Signals from the RPC strips are shaped by the FEE described on Figure 4.1a. Output LVDS signals are then read-out by a TDC module connected to a computer or converted into NIM and sent to scalers. Figure 4.1b describes how these converted signals are put in coincidence with the trigger.

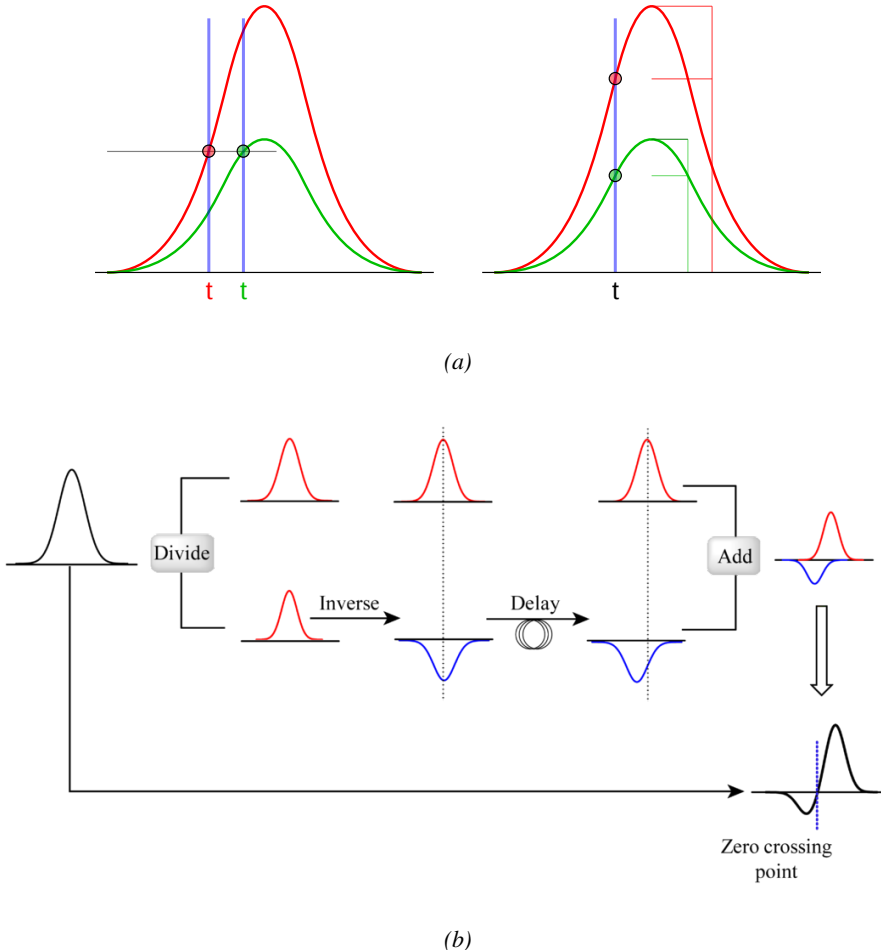


Figure 4.2: Description of the principle of a CFD. A comparison of threshold triggering (left) and constant fraction triggering (right) is shown in Figure 4.2a. Constant fraction triggering is obtained thanks to zero-crossing technique as explained in Figure 4.2b. The signal arriving at the input of the CFD is split into three components. A first one is delayed and connected to the inverting input of a first comparator. A second component is connected to the noninverting input of this first comparator. A third component is connected to the noninverting input of another comparator along with a threshold value connected to the inverting input. Finally, the output of both comparators is fed through an AND gate.

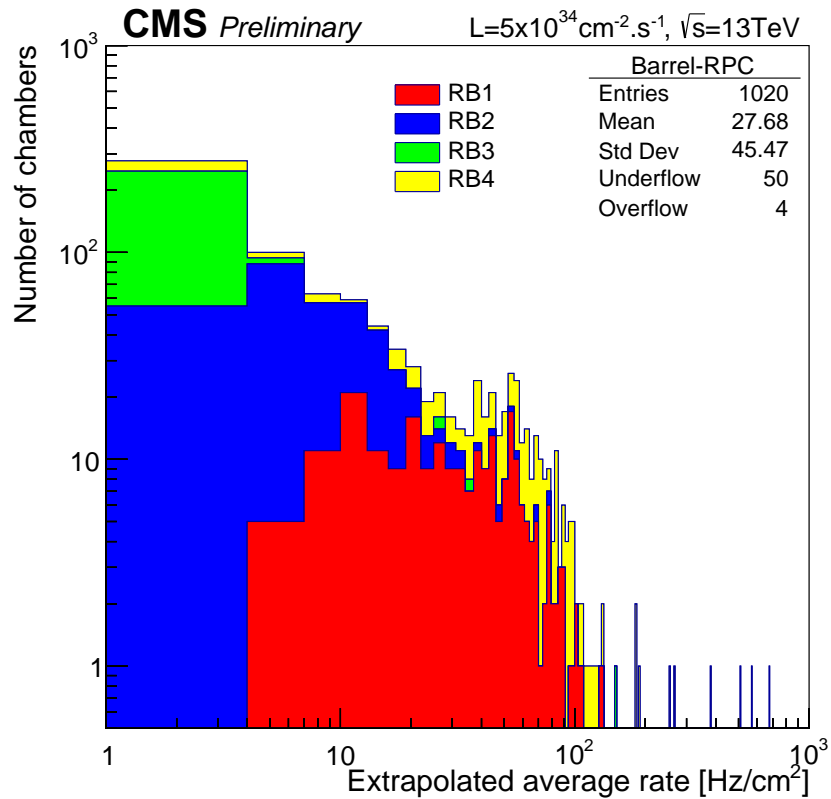
953 4.2 Testing detectors under extreme conditions

954 The upgrade from LHC to HL-LHC will increase the peak luminosity from $10^{34} \text{ cm}^{-2} \text{ s}^{-1}$ to reach
 955 $5 \times 10^{34} \text{ cm}^{-2} \text{ s}^{-1}$, increasing in the same way the total expected background to which the RPC
 956 system will be subjected to. Composed of low energy gammas and neutrons from $p\text{-}p$ collisions, low
 957 momentum primary and secondary muons, puch-through hadrons from calorimeters, and particles
 958 produced in the interaction of the beams with collimators, the background will mostly affect the
 959 regions of CMS that are the closest to the beam line, i.e. the RPC detectors located in the endcaps.
 960 [To update.]

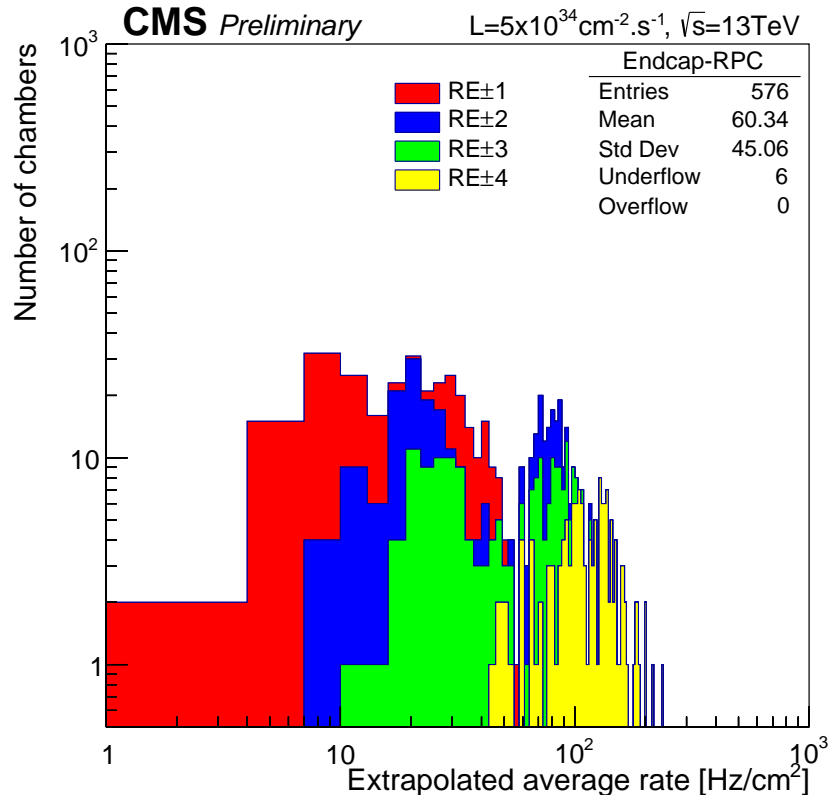
961

962 The 2016 data allowed to study the values of the background rate in all RPC system. In Fig-
963 ure 4.3, the distribution of the chamber background hit rate per unit area is shown at a luminosity
964 of $5 \times 10^{34} cm^{-2}.s^{-1}$ linearly extrapolating from data collected in 2016 [ref mentioning the linear
965 dependency of rate vs lumi]. The maximum rate per unit area at HL-LHC conditions is expected to
966 be of the order of $600 Hz/cm^2$ (including a safety factor 3). Nevertheless, Fluka simulations have
967 conducted in order to understand the background at HL-LHC conditions. The comparison to the
968 data has shown, in Figure 4.4, a discrepancy of a factor 2 even though the order of magnitude is
969 consistent. [Understand mismatch.]

970



(a)



(b)

Figure 4.3: (4.3a) Extrapolation from 2016 data of single hit rate per unit area in the barrel region. (4.3b) Extrapolation from 2016 data of single hit rate per unit area in the endcap region.

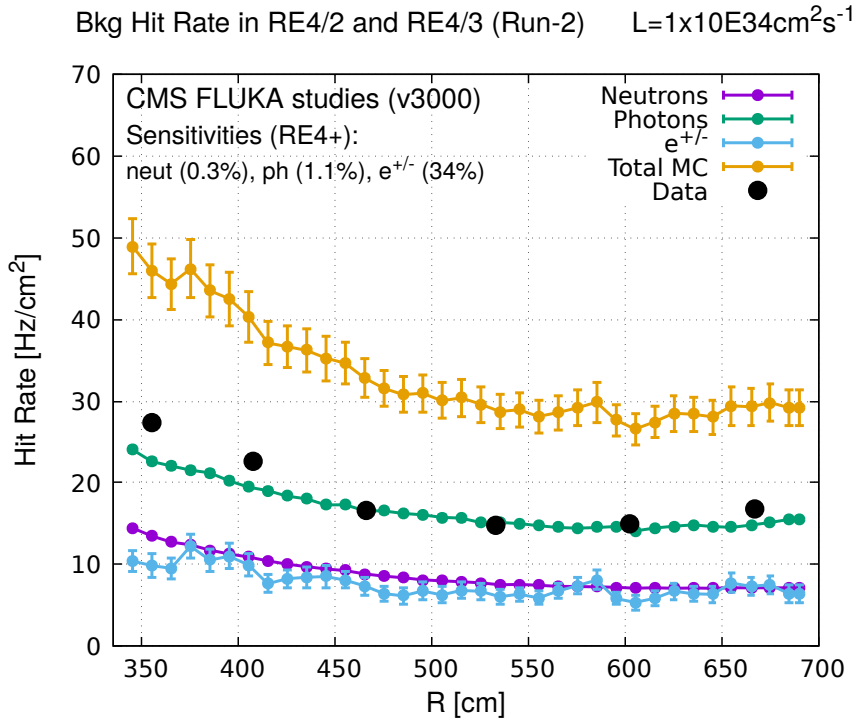


Figure 4.4: Background Fluka simulation compared to 2016 Data at $L = 10^{34} \text{ cm}^{-2} \cdot \text{s}^{-1}$ in the fourth endcap disk region. A mismatch in between simulation and data can be observed. [\[To be understood.\]](#)

In the past, extensive long-term tests were carried out at several gamma and neutron facilities certifying the detector performance. Both full size and small prototype RPCs have been irradiated with photons up to an integrated charge of $\sim 0.05C/\text{cm}^2$ and $\sim 0.4C/\text{cm}^2$, respectively [53, 54]. During Run-I, the RPC system provided stable operation and excellent performance and did not show any aging effects for integrated charge of the order of $0.01C/\text{cm}^2$. Projections on currents from 2016 Data, has allowed to determine that the total integrated charge, by the end of HL-LHC, would be of the order of $1C/\text{cm}^2$ (including a safety factor 3). [\[Corresponding figure needed.\]](#)

978

979 4.2.1 The Gamma Irradiation Facilities

980 4.2.1.1 GIF

981 Located in the SPS West Area at the downstream end of the X5 test beam, the Gamma Irradiation
 982 Facility (GIF) was a test area in which particle detectors were exposed to a particle beam in presence
 983 of an adjustable gamma background [55]. Its goal was to reproduce background conditions these
 984 detectors would suffer in their operating environment at LHC. GIF layout is shown in Figure 4.5.
 985 Gamma photons are produced by a strong ^{137}Cs source installed in the upstream part of the zone
 986 inside a lead container. The source container includes a collimator, designed to irradiate a $6 \times 6 \text{ m}^2$
 987 area at 5 m maximum to the source. A thin lens-shaped lead filter helps providing with a uniform
 988 outgoing flux in a vertical plane, orthogonal to the beam direction. The principal collimator hole
 989 provides a pyramidal aperture of $74^\circ \times 74^\circ$ solid angle and provides a photon flux in a pyramidal vol-

ume along the beam axis. The photon rate is controled by further lead filters allowing the maximum rate to be limited and to vary within a range of four orders of magnitude. Particle detectors under test are then placed within the pyramidal volume in front of the source, perpendicularly to the beam line in order to profit from the homogeneous photon flux. Adjusting the background flux of photons can then be done by using the filters and choosing the position of the detectors with respect to the source.

995

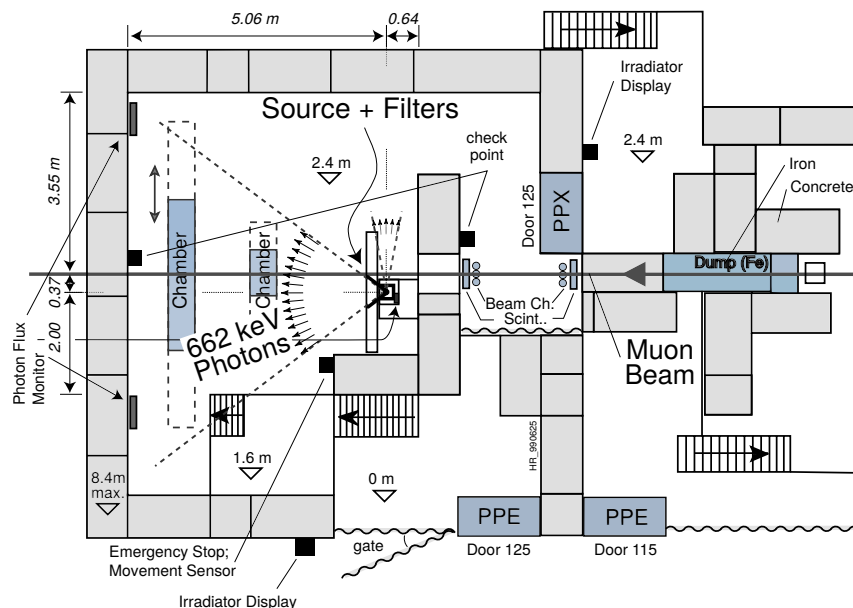


Figure 4.5: Layout of the test beam zone called X5c GIF at CERN. Photons from the radioactive source produce a sustained high rate of random hits over the whole area. The zone is surrounded by 8 m high and 80 cm thick concrete walls. Access is possible through three entry points. Two access doors for personnel and one large gate for material. A crane allows installation of heavy equipment in the area.

As described on Figure 4.6, the ^{137}Cs source emits a 662 keV photon in 85% of the decays. An activity of 740 GBq was measured on the 5th March 1997. To estimate the strength of the flux in 2014, it is necessary to consider the nuclear decay through time assiciated to the Cesium source whose half-life is well known ($t_{1/2} = (30.05 \pm 0.08)$ y). The GIF tests where done in between the 20th and the 31st of August 2014, i.e. at a time $t = (17.47 \pm 0.02)$ y resulting in an attenuation of the activity from 740 GBq in 1997 to 494 GBq in 2014.

1002

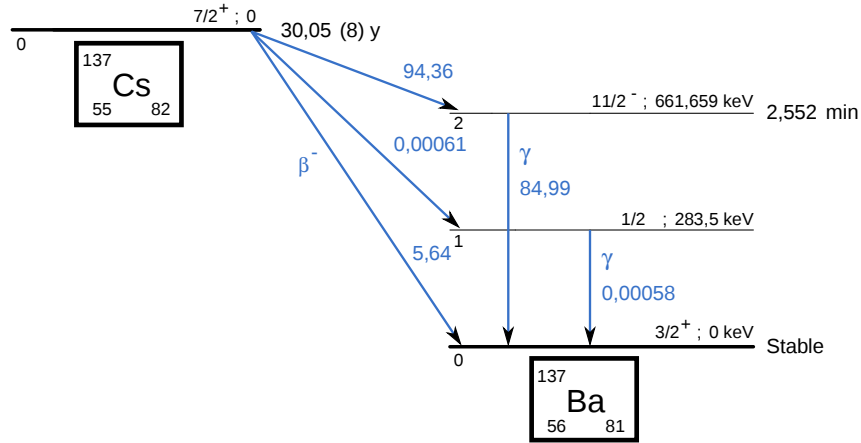


Figure 4.6: ^{137}Cs decays by β^- emission to the ground state of ^{137}Ba ($BR = 5.64\%$) and via the 662 keV isomeric level of ^{137}Ba ($BR = 94.36\%$) whose half-life is 2.55 min.

1003 4.2.1.2 GIF++

1004 The new Gamma Irradiation Facility (GIF++), located in the SPS North Area at the downstream end
 1005 of the H4 test beam, has replaced its predecessor during LS1 and has been operational since spring
 1006 2015 [56]. Like GIF, GIF++ features a ^{137}Cs source of 662 keV gamma photons, their fluence being
 1007 controlled with a set of filters of various attenuation factors. The source provides two separated large
 1008 irradiation areas for testing several full-size muon detectors with continuous homogeneous irradiation,
 1009 as presented in Figure 4.7.

1010

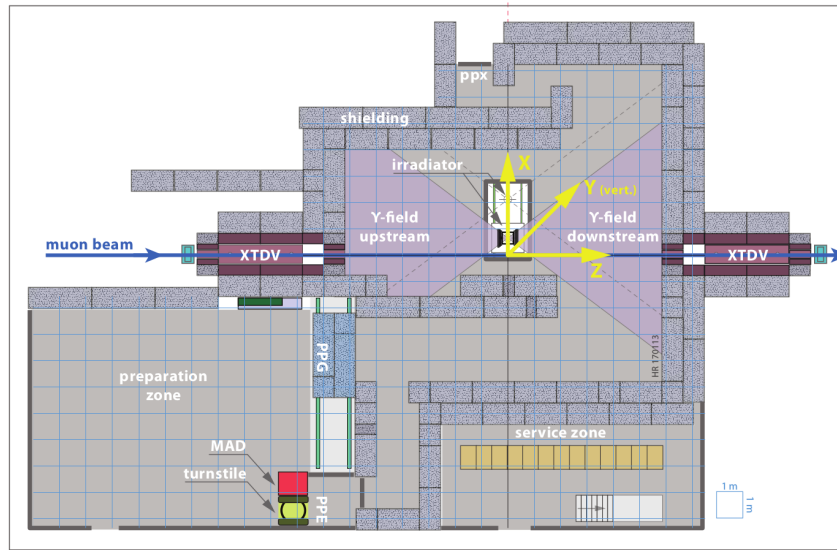


Figure 4.7: Floor plan of the GIF++ facility. When the facility downstream of the GIF++ takes electron beam, a beam pipe is installed along the beam line (z -axis). The irradiator can be displaced laterally (its center moves from $x = 0.65$ m to 2.15 m), to increase the distance to the beam pipe.

1011 The source activity was measured to be about 13.5 TBq in March 2016. The photon flux being
 1012 far greater than HL-LHC expectations, GIF++ provides an excellent facility for accelerated aging
 1013 tests of muon detectors.

1014

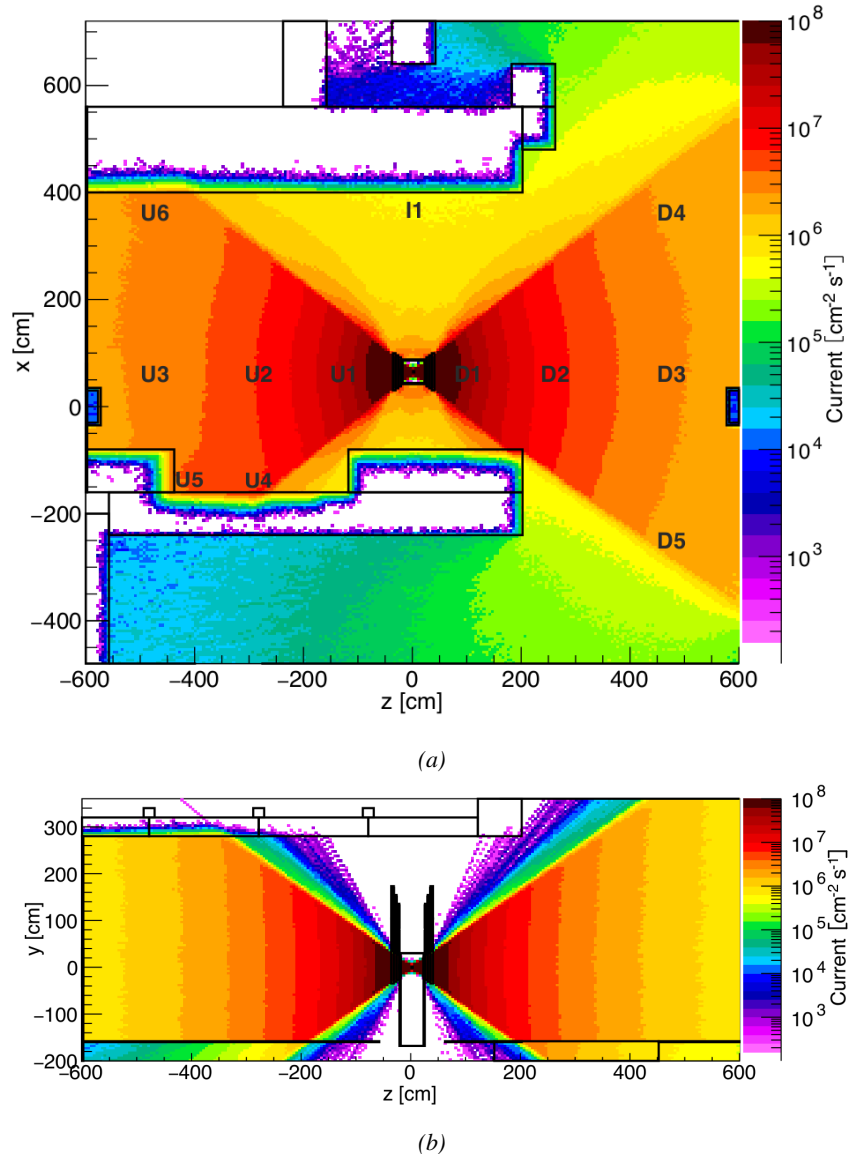


Figure 4.8: Simulated unattenuated current of photons in the xz plane (Figure 4.8a) and yz plane (Figure 4.8b) through the source at $x = 0.65$ m and $y = 0$ m. With angular correction filters, the current of 662 keV photons is made uniform in xy planes.

1015 The source is situated in the muon beam line with the muon beam being available a few times a
 1016 year. The H4 beam, composed of muons with a momentum of about 150 GeV/c, passes through the
 1017 GIF++ zone and is used to study the performance of the detectors. Its flux is of 104 particles/ s cm^2

1018 focused in an area similar to $10 \times 10 \text{ cm}^2$. Therefore, with properly adjusted filters, one can imitate
 1019 the HL-LHC background and study the performance of muon detectors with their trigger/readout
 1020 electronics in HL-LHC environment.

1021

1022 4.3 Preliminary tests at GIF

1023 4.3.1 Resistive Plate Chamber test setup

1024 During summer 2014, preliminary tests have been conducted in the GIF area on a newly produced
 1025 RE4/2 chamber labelled RE-4-2-BARC-161. This chamber has been placed into a trolley covered
 1026 with a tent. The position of the RPC inside the tent and of the tent related to the source is described
 1027 in Figure 4.9. To test this CMS RPC, three different absorber settings were used. First of all,
 1028 measurements were done with fully opened source. Then, to complete this preliminary study, the
 1029 gamma flux has been attenuated from a factor 2 and a factor 5. The expected gamma flux at the level
 1030 of our detector will be discussed in subsection ??.

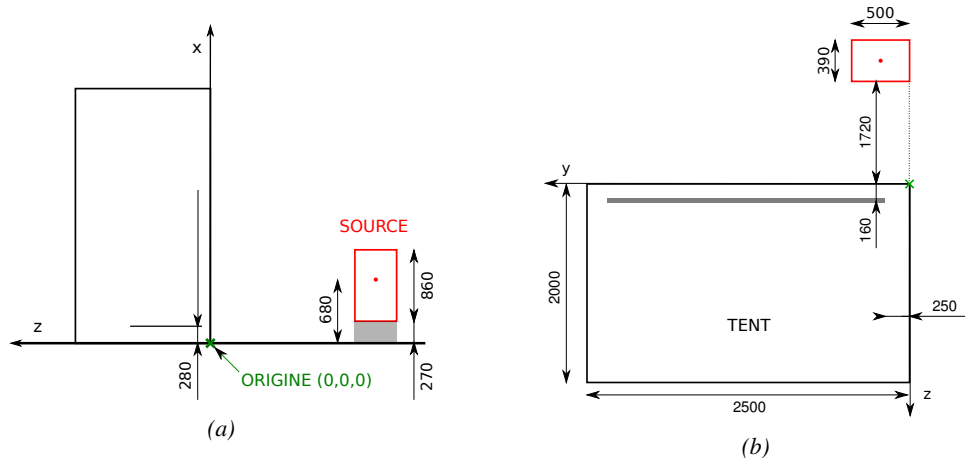


Figure 4.9: Description of the RPC setup. Dimensions are given in mm. A tent containing RPCs is placed at 1720 mm from the source container. The source is situated in the center of the container. RE-4-2-BARC-161 chamber is 160 mm inside the tent. This way, the distance between the source and the chambers plan is 2060 mm. Figure 4.9a provides a side view of the setup in the xz plane while Figure 4.9b shows a top view in the yz plane.



Figure 4.10: RE-4-2-BARC-I61 chamber is inside the tent as described in Figure 4.9. In the top right, the two scintillators used as trigger can be seen. This trigger system has an inclination of 10° relative to horizontal and is placed above half-partition B2 of the RPCs. PMT electronics are shielded thanks to lead blocks placed in order to protect them without stopping photons from going through the scintillators and the chamber.

1031 At the time of the tests, the beam not being operational anymore, a trigger composed of 2 plastic
 1032 scintillators has been placed in front of the setup with an inclination of 10 deg with respect to the
 1033 detector plane in order to look at cosmic muons. Using this particular trigger layout, shown on Fig-
 1034 ure 4.10, leads to a cosmic muon hit distribution into the chamber similar to the one in Figure 4.11.
 1035 Measured without gamma irradiation, two peaks can be seen on the profile of partition B, centered
 1036 on strips 52 and 59. Section ?? will help us understand that these two peaks are due respectively to
 1037 forward and backward coming cosmic particles where forward coming particles are first detected by
 1038 the scintillators and then the RPC while the backward coming muons are first detected in the RPC.

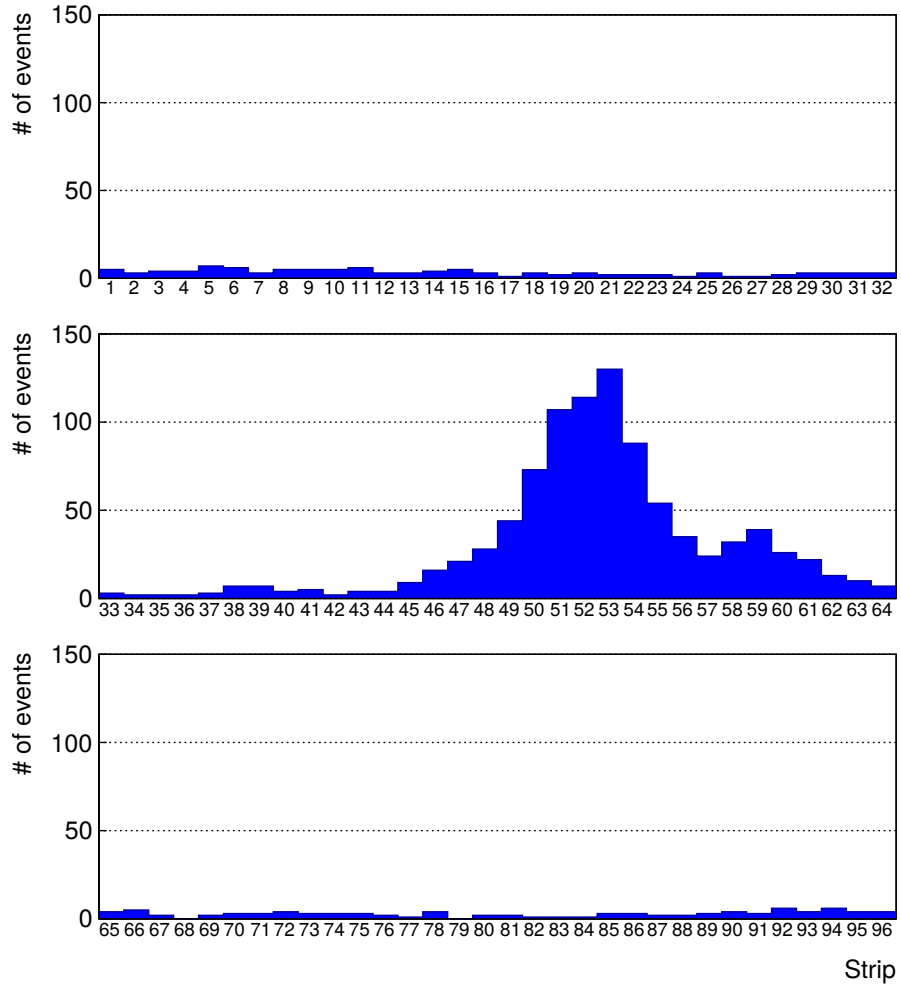


Figure 4.11: Hit distributions over all 3 partitions of RE-4-2-BARC-161 chamber is showed on these plots. Top, middle and bottom figures respectively correspond to partitions A, B, and C. These plots show that some events still occur in other half-partitions than B2, which corresponds to strips 49 to 64, in front of which the trigger is placed, contributing to the inefficiency of detection of cosmic muons. In the case of partitions A and C, the very low amount of data can be interpreted as noise. On the other hand, it is clear that a little portion of muons reach the half-partition B1, corresponding to strips 33 to 48.

1039 4.3.2 Data Acquisition

1040 4.3.3 Geometrical acceptance of the setup layout to cosmic muons

1041 In order to profit from a constant gamma irradiation, the detectors inside of the GIF bunker need
 1042 to be placed in a plane orthogonal to the beam line. The muon beam that used to be available was
 1043 meant to test the performance of detectors under test. This beam not being active anymore, another
 1044 solution to test detector performance had to be used. Thus, it has been decided to use cosmic muons
 1045 detected through a telescope composed of two scintillators. Lead blocks were used as shielding to

1046 protect the photomultipliers from gammas as can be seen from Figure 4.10.

1047 An inclination has been given to the cosmic telescope to maximize the muon flux. A good com-
 1048 promise had to be found between good enough muon flux and narrow enough hit distribution to
 1049 be sure to contain all the events into only one half partitions as required from the limited available
 1050 readout hardware. Nevertheless, a consequence of the misplaced trigger, that can be seen as a loss
 1051 of events in half-partition B1 in Figure 4.11, is an inefficiency. Nevertheless, the inefficiency of ap-
 1052 proximately 20 % highlighted in Figure 4.12 by comparing the performance of chamber BARC-161
 1053 in 904 and at GIF without irradiation seems too important to be explained only by the geometri-
 1054 cal acceptance of the setup itself. Simulations have been conducted to show how the setup brings
 1055 inefficiency.

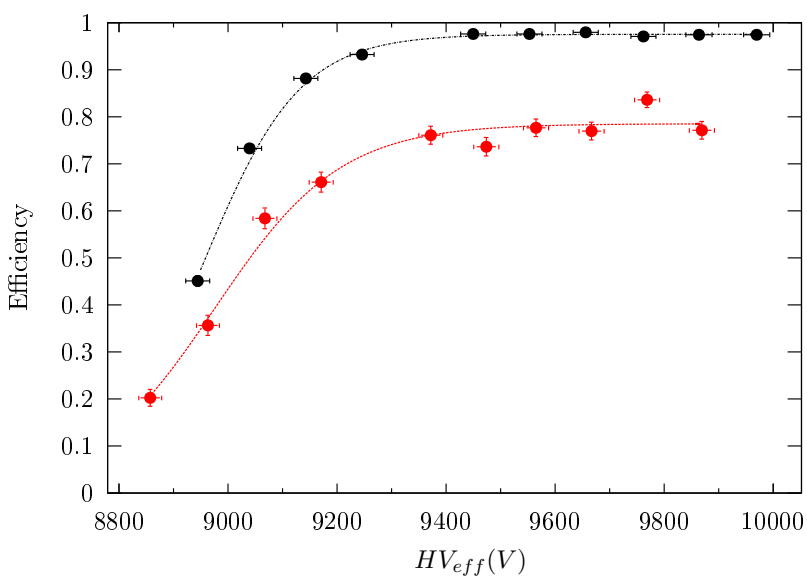


Figure 4.12: Results are derived from data taken on half-partition B2 only. On the 18th of June 2014, data has been taken on chamber RE-2-BARC-161 at building 904 (Prevessin Site) with cosmic muons providing us a reference efficiency plateau of $(97.54 \pm 0.15)\%$ represented by a black curve. A similar measurement has been done at GIF on the 21st of July with the same chamber giving a plateau of $(78.52 \pm 0.94)\%$ represented by a red curve.

1056 4.3.3.1 Description of the simulation layout

1057 The layout of GIF setup has been reproduced and incorporated into a Monte Carlo (MC) simulation
 1058 to study the influence of the disposition of the telescope on the final distribution measured by the
 1059 RPC. A 3D view of the simulated layout is given into Figure 4.13. Muons are generated randomly
 1060 in a horizontal plane located at a height corresponding to the lowest point of the PMTs. This way,
 1061 the needed size of the plane in order to simulate events happening at very big azimuthal angles (i.e.
 1062 $\theta \approx \pi$) can be kept relatively small. The muon flux is designed to follow the usual $\cos^2\theta$ distribution
 1063 for cosmic particle. The goal of the simulation is to look at muons that pass through the muon
 1064 telescope composed of the two scintillators and define their distribution onto the RPC plane. During
 1065 the reconstruction, the RPC plane is then divided into its strips and each muon track is assigned to a
 1066 strip.

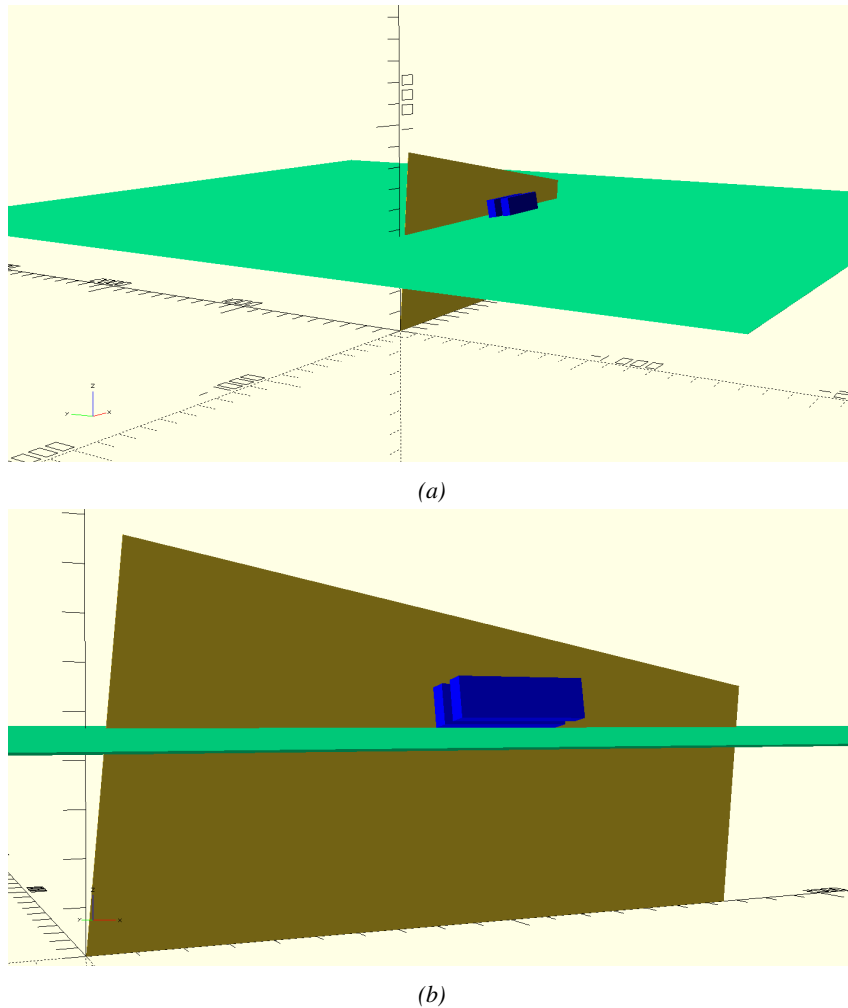


Figure 4.13: Representation of the layout used for the simulations of the test setup. The RPC is represented as a yellow trapezoid while the two scintillators as blue cuboids looking at the sky. A green plane corresponds to the muon generation plane within the simulation. Figure 4.9a shows a global view of the simulated setup. Figure 4.9b shows a zoomed view that allows to see the 2 scintillators as well as the full RPC plane.

1067 In order to further refine the quality of the simulation and understand deeper the results the
 1068 dependance of the distribution has been studied for a range of telescope inclinations. Moreover,
 1069 the threshold applied on the PMT signals has been included into the simulation in the form of a
 1070 cut. In the approximation of uniform scintillators, it has been considered that the threshold can be
 1071 understood as the minimum distance particles need to travel through the scintillating material to give
 1072 a strong enough signal. Particles that travel a distance smaller than the set "threshold" are thus not
 1073 detected by the telescope and cannot trigger the data taking. Finally, the FEE threshold also has
 1074 been considered in a similar way. The mean momentum of horizontal cosmic rays is higher than
 1075 those of vertical ones but the stopping power of matter for momenta ranging from 1 GeV to 1 TeV
 1076 stays comparable. It is then possible to assume that the mean number of primary e^- /ion pairs per
 1077 unit length will stay similar and thus, depending on the applied discriminator threshold, muons with

1078 the shortest path through the gas volume will deposit less charge and induce a smaller signal on the
 1079 pick-up strips that could eventually not be detected. These two thresholds also restrain the overall
 1080 geometrical acceptance of the system.

1081 4.3.3.2 Simulation procedure

1082 The simulation software has been designed using C++ and the output data is saved into ROOT
 1083 histograms. Simulations start for a threshold T_{scint} varying in a range from 0 to 45 mm in steps
 1084 of 5 mm, where $T_{scint} = 0$ mm corresponds to the case where there isn't any threshold apply on
 1085 the input signal while $T_{scint} = 45$ mm, which is the scintillator thickness, is the case where muons
 1086 cannot arrive orthogonally onto the scintillator surface. For a given T_{scint} , a set of RPC thresholds
 1087 are considered. The RPC threshold, T_{RPC} varies from 2 mm, the thickness of the gas volume, to
 1088 3 mm in steps of 0.25 mm. For each $(T_{scint}; T_{RPC})$ pair, $N_\mu = 10^8$ muons are randomly generated
 1089 inside the muon plane described in the previous paragraph with an azimuthal angle θ chosen to follow
 1090 a $\cos^2\theta$ distribution.

1091 Planes are associated to each surface of the scintillators. Knowing muon position into the muon
 1092 plane and its direction allows us, by assuming that muons travel in a straight line, to compute the
 1093 intersection of the muon track with these planes. Applying conditions to the limits of the surfaces
 1094 of the scintillator faces then gives us an answer to whether or not the muon passed through the
 1095 scintillators. In the case the muon has indeed passed through the telescope, the path through each
 1096 scintillator is computed and muons whose path was shorter than T_{scint} are rejected and are thus
 1097 considered as having not interacted with the setup.

1098 On the contrary, if the muon is labeled as good, its position within the RPC plane is computed
 1099 and the corresponding strip, determined by geometrical tests in the case the distance through the
 1100 gas volume was enough not to be rejected because of T_{RPC} , gets a hit and several histograms
 1101 are filled in order to keep track of the generation point on the muon plane, the intersection points
 1102 of the reconstructed muons within the telescope, or on the RPC plane, the path traveled through
 1103 each individual scintillator or the gas volume, as well as other histograms. Moreover, muons fill
 1104 different histograms whether they are forward or backward coming muons. They are discriminated
 1105 according to their direction components. When a muon is generated, an (x, y, z) position is assigned
 1106 into the muon plane as well as a $(\theta; \phi)$ pair that gives us the direction it's coming from. This way,
 1107 muons satisfying the condition $0 \leq \phi < \pi$ are designated as backward coming muons while muons
 1108 satisfying $\pi \leq \phi < 2\pi$ as forward coming muons.

1109 This simulation is then repeated for different telescope inclinations ranging in between 4 and 20°
 1110 and varying in steps of 2°. Due to this inclination and to the vertical position of the detector under
 1111 test, the muon distribution reconstructed in the detector plane is asymmetrical. The choice as been
 1112 made to chose a skew distribution formula to fit the data built as the multiplication of gaussian and
 1113 sigmoidal curves together. A typical gaussian formula is given as 4.1 and has three free parameters
 1114 as A_g , its amplitude, \bar{x} , its mean value and σ , its root mean square. Sigmoidal curves as given by
 1115 formula 4.2 are functions converging to 0 and A_s as x diverges. The inflection point is given as x_i
 1116 and λ is proportional to the slope at $x = x_i$. In the limit where $\lambda \rightarrow \infty$, the sigmoid becomes a
 1117 step function.

$$g(x) = A_g e^{-\frac{(x-\bar{x})^2}{2\sigma^2}} \quad (4.1)$$

$$s(x) = \frac{A_s}{1 + e^{-\lambda(x-x_i)}} \quad (4.2)$$

Finally, a possible representation of a skew distribution is given by formula 4.3 and is the product of 4.1 and 4.2. Naturally, here $A_{sk} = A_g \times A_s$ and represents the theoretical maximum in the limit where the skew tends to a gaussian function.

$$sk(x) = g(x) \times s(x) = A_{sk} \frac{e^{\frac{-(x-\bar{x})^2}{2\sigma^2}}}{1 + e^{-\lambda(x-x_i)}} \quad (4.3)$$

4.3.3.3 Results

Influence of T_{scint} on the muon distribution

Influence of T_{RPC} on the muon distribution

Influence of the telescope inclination on the muon distribution

Comparison to data taken at GIF without irradiation

4.3.4 Photon flux at GIF

4.3.4.1 Expectations from simulations

In order to understand and evaluate the γ flux in the GIF area, simulations had been conducted in 1999 and published by S. Agosteo et al [55]. Table 4.1 presented in this article gives us the γ flux for different distances D to the source. This simulation was done using GEANT and a Monte Carlo N-Particle (MCNP) transport code, and the flux F is given in number of γ per unit area and unit time along with the estimated error from these packages expressed in %.

Nominal ABS	Photon flux F [$s^{-1}cm^{-2}$]			
	at $D = 50$ cm	at $D = 155$ cm	at $D = 300$ cm	at $D = 400$ cm
1	$0.12 \cdot 10^8 \pm 0.2\%$	$0.14 \cdot 10^7 \pm 0.5\%$	$0.45 \cdot 10^6 \pm 0.5\%$	$0.28 \cdot 10^6 \pm 0.5\%$
2	$0.68 \cdot 10^7 \pm 0.3\%$	$0.80 \cdot 10^6 \pm 0.8\%$	$0.25 \cdot 10^6 \pm 0.8\%$	$0.16 \cdot 10^6 \pm 0.6\%$
5	$0.31 \cdot 10^7 \pm 0.4\%$	$0.36 \cdot 10^6 \pm 1.2\%$	$0.11 \cdot 10^6 \pm 1.2\%$	$0.70 \cdot 10^5 \pm 0.9\%$

Table 4.1: Total photon flux ($E\gamma \leq 662$ keV) with statistical error predicted considering a ^{137}Cs activity of 740 GBq at different values of the distance D to the source along the x -axis of irradiation field [55].

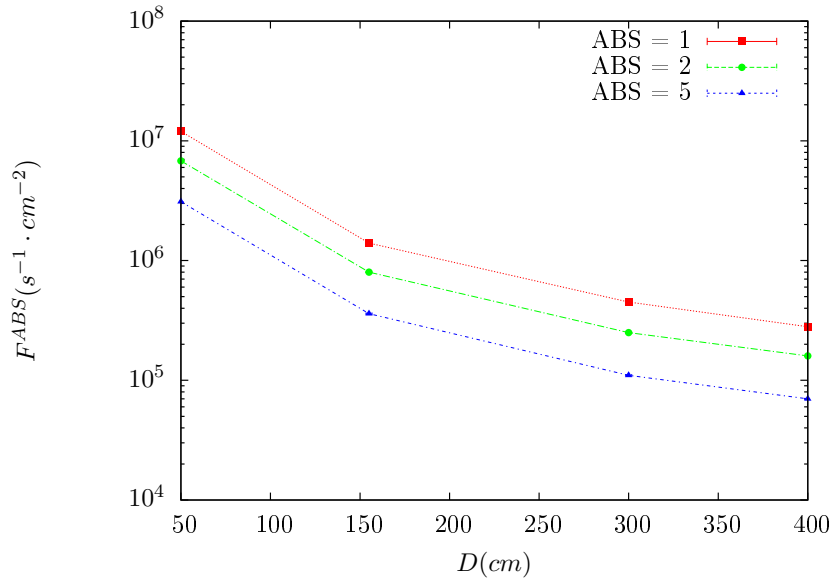


Figure 4.14: γ flux $F(D)$ is plot using values from table 4.1. As expected, the plot shows similar attenuation behaviours with increasing distance for each absorption factors.

The simulation doesn't directly provides us with an estimated flux at the level of our RPC. First of all, it is needed to extract the value of the flux from the available data contained in the original paper and then to estimate the flux in 2014 at the time the experimentation took place. Figure 4.14 that contains the data from Table 4.1. In the case of a pointlike source emitting isotropic and homogeneous gamma radiations, the gamma flux F at a distance D to the source with respect to a reference point situated at D_0 where a known flux F_0 is measured will be expressed like in Equation 4.4, assuming that the flux decreases as $1/D^2$, where c is a fitting factor.

$$F^{ABS} = F_0^{ABS} \times \left(\frac{cD_0}{D} \right)^2 \quad (4.4)$$

By rewriting Equation 4.4, it comes that :

$$c = \frac{D}{D_0} \sqrt{\frac{F^{ABS}}{F_0^{ABS}}} \quad (4.5)$$

$$\Delta c = \frac{c}{2} \left(\frac{\Delta F^{ABS}}{F^{ABS}} + \frac{\Delta F_0^{ABS}}{F_0^{ABS}} \right) \quad (4.6)$$

Finally, using Equation 4.5 and the data in Table 4.1 with $D_0 = 50$ cm as reference point, we can build Table 4.2. It is interesting to note that c for each value of D doesn't depend on the absorption factor.

Nominal ABS	Correction factor c		
	at $D = 155$ cm	at $D = 300$ cm	at $D = 400$ cm
1	$1.059 \pm 0.70\%$	$1.162 \pm 0.70\%$	$1.222 \pm 0.70\%$
2	$1.063 \pm 1.10\%$	$1.150 \pm 1.10\%$	$1.227 \pm 0.90\%$
5	$1.056 \pm 1.60\%$	$1.130 \pm 1.60\%$	$1.202 \pm 1.30\%$

Table 4.2: Correction factor c is computed thanks to formulae 4.5 taking as reference $D_0 = 50$ cm and the associated flux F_0^{ABS} for each absorption factor available in table 4.1.

1144 For the range of D/D_0 values available, it is possible to use a simple linear fit to get the evolution
 1145 of c . The linear fit will then use only 2 free parameters, a and b , as written in Equation 4.7. This gives
 1146 us the results showed in Figure 4.15. Figure 4.15b confirms that using only a linear fit to extract c is
 1147 enough as the evolution of the rate that can be obtained superimposes well on the simulation points.

$$c \left(\frac{D}{D_0} \right) = a \frac{D}{D_0} + b \quad (4.7)$$

$$F^{ABS} = F_0^{ABS} \left(a + \frac{b D_0}{D} \right)^2 \quad (4.8)$$

$$\Delta F^{ABS} = F^{ABS} \left[\frac{\Delta F_0^{ABS}}{F_0^{ABS}} + 2 \frac{\Delta a + \Delta b \frac{D_0}{D}}{a + \frac{b D_0}{D}} \right] \quad (4.9)$$

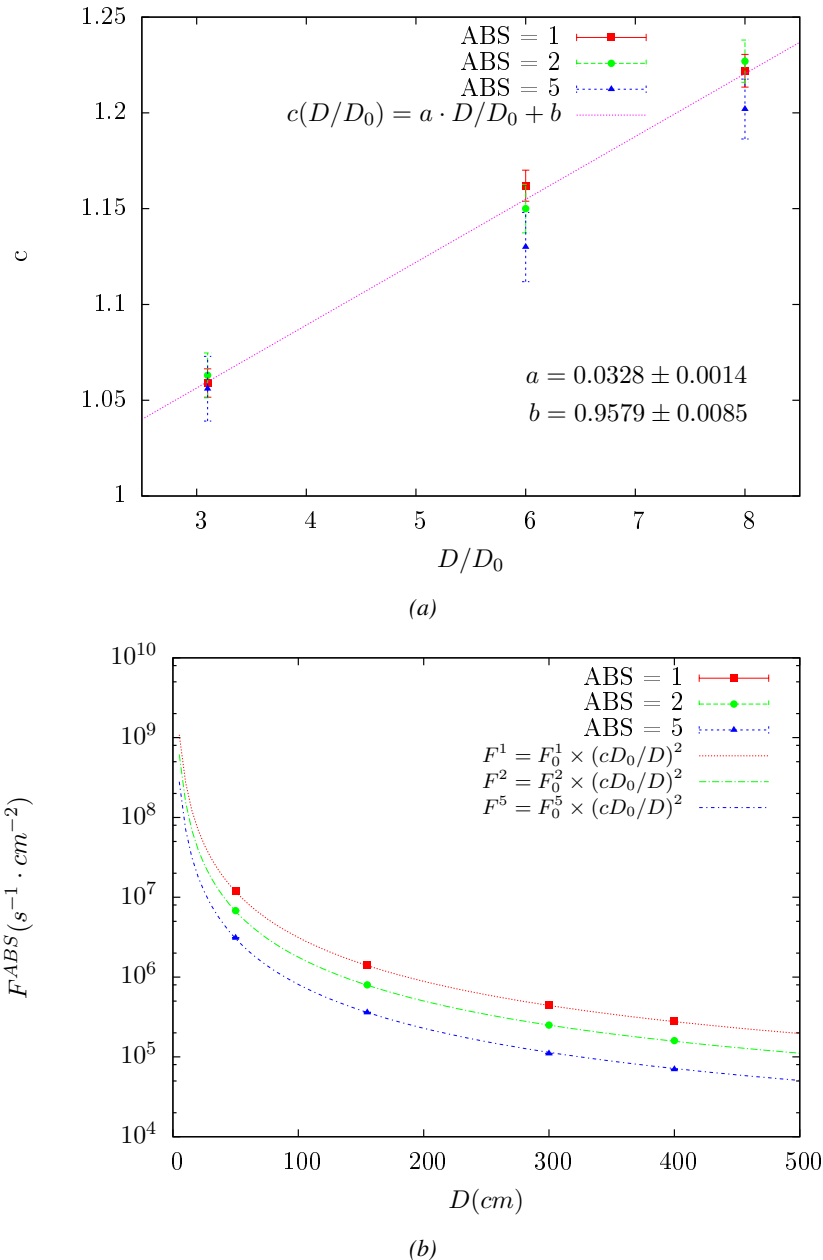


Figure 4.15: Figure 4.15a shows the linear approximation fit done via formulae 4.7 on data from table 4.2. Figure 4.15b shows a comparison of this model with the simulated flux using a and b given in figure 4.15a in formulae 4.4 and the reference value $D_0 = 50\text{cm}$ and the associated flux for each absorption factor F_0^{ABS} from table 4.1

In the case of the 2014 GIF tests, the RPC plane is located at a distance $D = 206\text{ cm}$ to the source.
 Moreover, to estimate the strength of the flux in 2014, it is necessary to consider the nuclear decay through time associated to the Cesium source whose half-life is well known ($t_{1/2} = (30.05 \pm 0.08)\text{ y}$).
 The very first source activity measurement has been done on the 5th of March 1997 while the GIF

¹¹⁴⁸ In the case of the 2014 GIF tests, the RPC plane is located at a distance $D = 206\text{ cm}$ to the source.

¹¹⁴⁹ Moreover, to estimate the strength of the flux in 2014, it is necessary to consider the nuclear decay through time associated to the Cesium source whose half-life is well known ($t_{1/2} = (30.05 \pm 0.08)\text{ y}$).

¹¹⁵¹ The very first source activity measurement has been done on the 5th of March 1997 while the GIF

1152 tests where done in between the 20th and the 31st of August 2014, i.e. at a time $t = (17.47 \pm 0.02)$ y
 1153 resulting in an attenuation of the activity from 740 GBq in 1997 to 494 GBq in 2014. All the needed
 1154 information to extrapolate the flux through our detector in 2014 has now been assembled, leading
 1155 to the Table 4.3. It is interesting to note that for a common RPC sensitivity to γ of $2 \cdot 10^{-3}$, the
 1156 order of magnitude of the estimated hit rate per unit area is of the order of the kHz for the fully
 1157 opened source. Moreover, taking profit of the two working absorbers, it will be possible to scan
 1158 background rates at 0 Hz, ~ 300 Hz as well as ~ 600 Hz. Without source, a good estimate of the
 1159 intrinsic performance will be available. Then at 300 Hz, the goal will be to show that the detectors
 1160 fulfill the performance certification of CMS RPCs. Then a first idea of the performance of the
 1161 detectors at higher background will be provided with absorption factors 2 (~ 600 Hz) and 1 (no
 1162 absorption). [Here I will also put a reference to the plot showing the estimated background rate at
 1163 the level of RE3/1 in the case of HL-LHC but this one being in another chapter, I will do it later.]

Nominal ABS	Photon flux F [$s^{-1}cm^{-2}$]			Hit rate/unit area [$Hz cm^{-2}$] at $D^{2014} = 206$ cm
	at $D_0^{1997} = 50$ cm	at $D^{1997} = 206$ cm	at $D^{2014} = 206$ cm	
1	$0.12 \cdot 10^8 \pm 0.2\%$	$0.84 \cdot 10^6 \pm 0.3\%$	$0.56 \cdot 10^6 \pm 0.3\%$	1129 ± 32
2	$0.68 \cdot 10^7 \pm 0.3\%$	$0.48 \cdot 10^6 \pm 0.3\%$	$0.32 \cdot 10^6 \pm 0.3\%$	640 ± 19
5	$0.31 \cdot 10^7 \pm 0.4\%$	$0.22 \cdot 10^6 \pm 0.3\%$	$0.15 \cdot 10^6 \pm 0.3\%$	292 ± 9

Table 4.3: The data at D_0 in 1997 is taken from [55]. In a second step, using Equations 4.8 and 4.9, the flux at D can be estimated in 1997. Then, taking into account the attenuation of the source activity, the flux at D can be estimated at the time of the tests in GIF in 2014. Finally, assuming a sensitivity of the RPC to γ $s = 2 \cdot 10^{-3}$, an estimation of the hit rate per unit area is obtained.

¹¹⁶⁴ **4.3.4.2 Dose measurements**

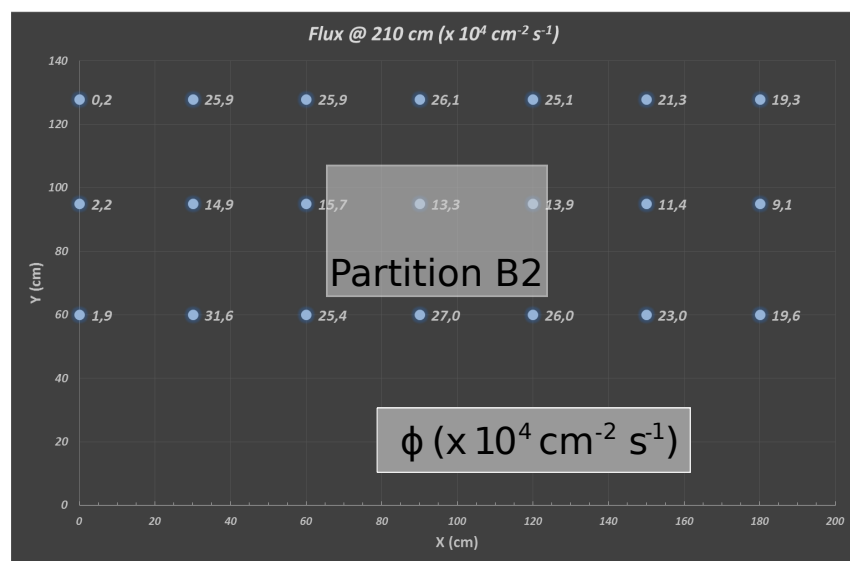


Figure 4.16: Dose measurements has been done in a plane corresponding to the tents front side. This plan is 1900 mm away from the source. As explained in the first chapter, a lens-shaped lead filter provides a uniform photon flux in the vertical plan orthogonal to the beam direction. If the second line of measured fluxes is not taken into account because of lower values due to experimental equipments in the way between the source and the tent, the uniformity of the flux is well showed by the results.

¹¹⁶⁵ **4.3.5 Results and discussions**

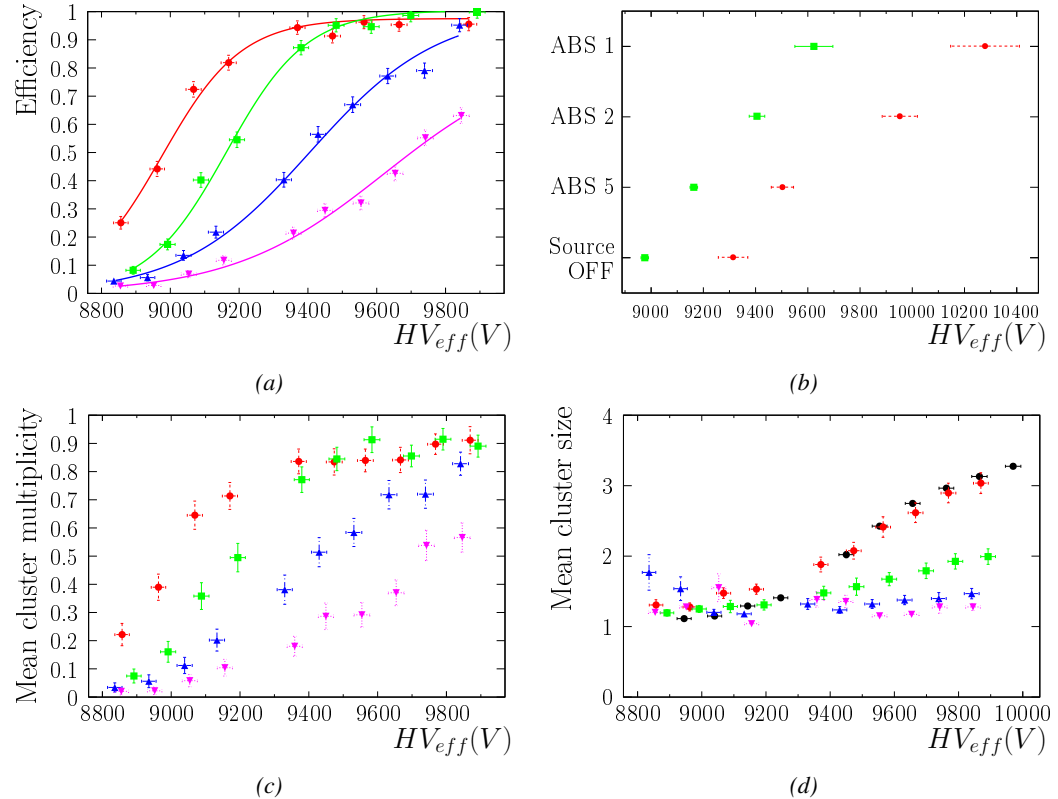


Figure 4.17

1166 4.4 Longevity tests at GIF++

1167 Longevity studies imply a monitoring of the performance of the detectors probed using a high inten-
1168 sity muon beam in a irradiated environment by periodically measuring their rate capability, the dark
1169 current running through them and the bulk resistivity of the Bakelite composing their electrodes.
1170 GIF++, with its very intense ^{137}Cs source, provides the perfect environment to perform such kind
1171 of tests. Assuming a maximum acceleration factor of 3, it is expected to accumulate the equivalent
1172 charge in 1.7 years.

1173 As the maximum background is found in the endcap, the choice naturally was made to focus the
1174 GIF++ longevity studies on endcap chambers. Most of the RPC system was installed in 2007. Nev-
1175 ertheless, the large chambers in the fourth endcap (RE4/2 and RE4/3) have been installed during
1176 LS1 in 2014. The Bakelite of these two different productions having different properties, four spare
1177 chambers of the present system were selected, two RE2,3/2 spares and two RE4/2 spares. Having
1178 two chambers of each type allows to always keep one of them non irradiated as reference, the per-
1179 formance evolution of the irradiated chamber being then compared through time to the performance
1180 of the non irradiated one.

1181 The performance of the detectors under different level of irradiation is measured periodically dur-
1182 ing dedicated test beam periods using the H4 muon beam. In between these test beam periods, the
1183 two RE2,3/2 and RE4/2 chambers selected for this study are irradiated by the ^{137}Cs source in order
1184 to accumulate charge and the gamma background is monitored, as well as the currents. The two
1185 remaining chambers are kept non-irradiated as reference detectors. Due to the limited gas flow in
1186 GIF++, the RE4 chamber remained non-irradiated until end of November 2016 where a new mass
1187 flow controller has been installed allowing for bigger volumes of gas to flow in the system.

1188 Figures 4.18 and 4.19 give us for different test beam periods, and thus for increasing integrated
1189 charge through time, a comparison of the maximum efficiency, obtained using a sigmoid-like func-
1190 tion, and of the working point of both irradiated and non irradiated chambers [**SIGMOID2005**]. No
1191 aging is yet to see from this data, the shifts in γ rate per unit area in between irradiated and non
1192 irradiated detectors and RE2 and RE4 types being easily explained by a difference of sensitivity due
1193 to the various Bakelite resistivities of the HPL electrodes used for the electrode production.

1194 Collecting performance data at each test beam period allows us to extrapolate the maximum effi-
1195 ciency for a background hit rate of $300\text{ Hz}/\text{cm}^2$ corresponding to the expected HL-LHC conditions.
1196 Aging effects could emerge from a loss of efficiency with increasing integrated charge over time,
1197 thus Figure 4.20 helps us understand such degradation of the performance of irradiated detectors in
1198 comparison with non irradiated ones. The final answer for an eventual loss of efficiency is given in
1199 Figure 4.21 by comparing for both irradiated and non irradiated detectors the efficiency sigmoids
1200 before and after the longevity study. Moreover, to complete the performance information, the Bake-
1201 lite resistivity is regularly measured thanks to Ag scans (Figure 4.22) and the noise rate is monitored
1202 weekly during irradiation periods (Figure 4.23). At the end of 2016, no signs of aging were observed
1203 and further investigation is needed to get closer to the final integrated charge requirements proposed
1204 for the longevity study of the present CMS RPC sub-system.

1205

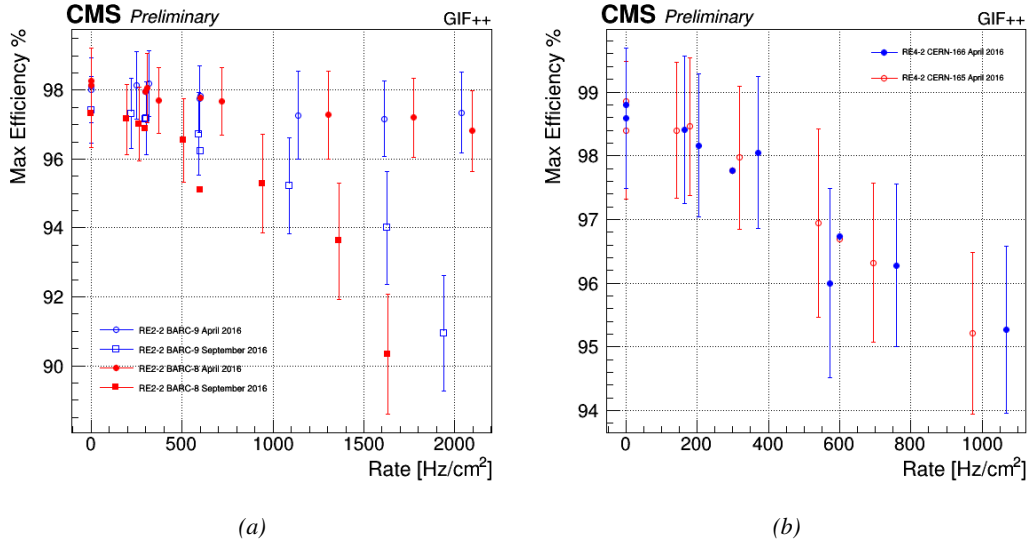


Figure 4.18: Evolution of the maximum efficiency for RE2 (4.18a) and RE4 (4.18b) chambers with increasing extrapolated γ rate per unit area at working point. Both irradiated (blue) and non irradiated (red) chambers are shown.

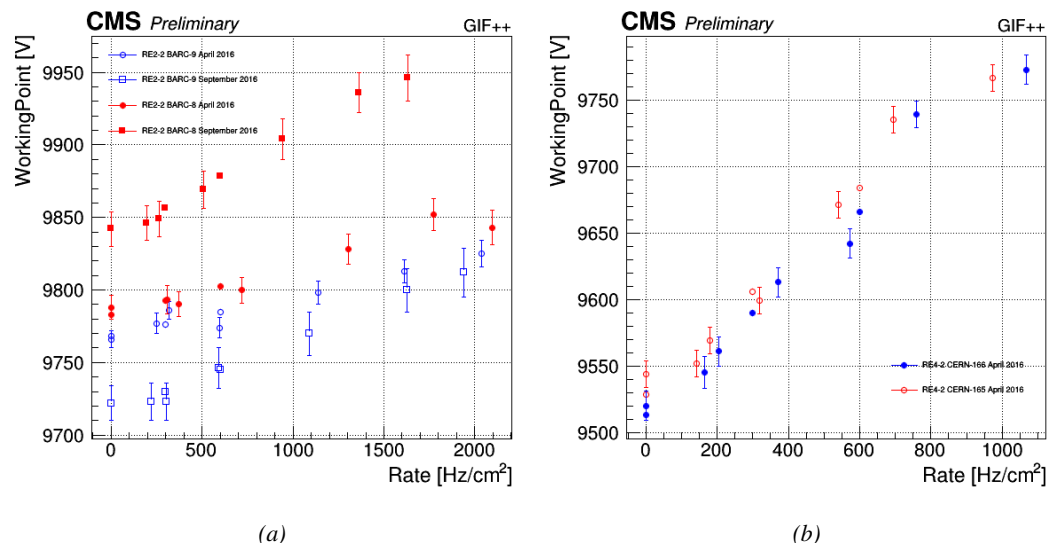


Figure 4.19: Evolution of the working point for RE2 (4.19a) and RE4 (4.19b) with increasing extrapolated γ rate per unit area at working point. Both irradiated (blue) and non irradiated (red) chambers are shown.

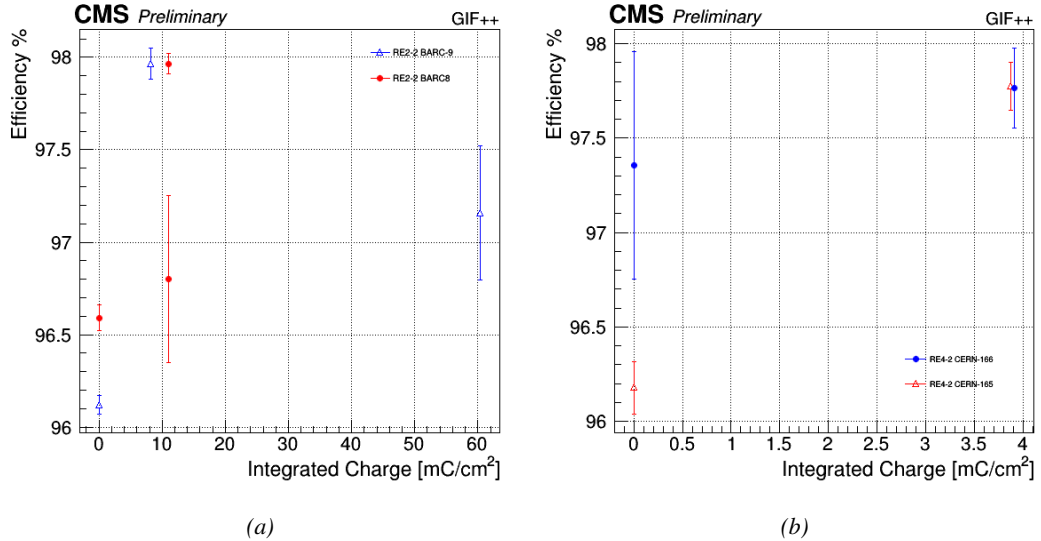


Figure 4.20: Evolution of the maximum efficiency at HL-LHC conditions, i.e. a background hit rate per unit area of 300 Hz/cm², with increasing integrated charge for RE2 (4.20a) and RE4 (4.20b) detectors. Both irradiated (blue) and non irradiated (red) chambers are shown. The integrated charge for non irradiated detectors is recorded during test beam periods and stays small with respect to the charge accumulated in irradiated chambers.

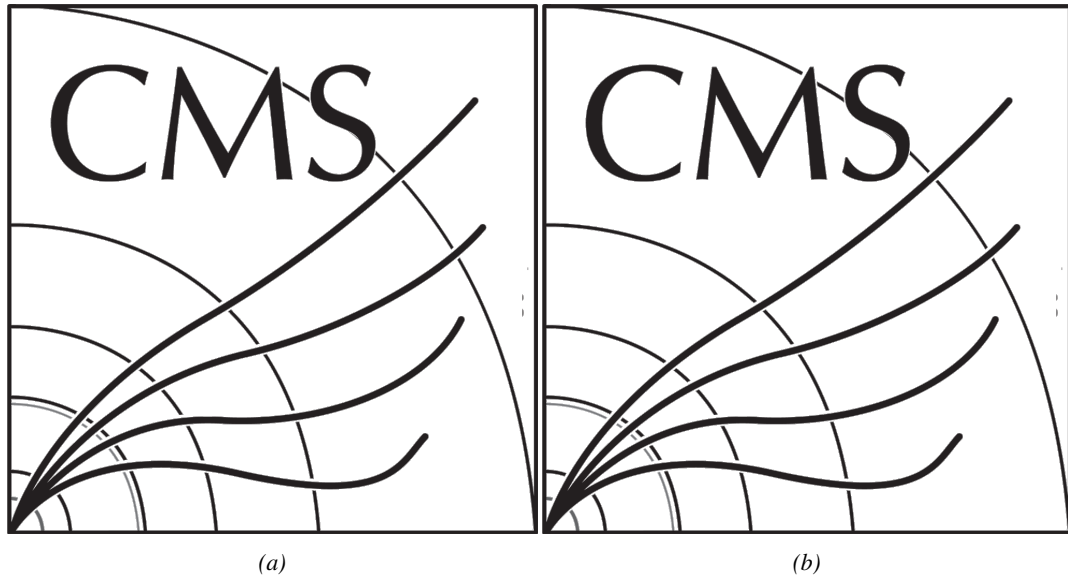


Figure 4.21: Comparison of the efficiency sigmoid before (triangles) and after (circles) irradiation for RE2 (4.21a) and RE4 (4.21b) detectors. Both irradiated (blue) and non irradiated (red) chambers are shown.

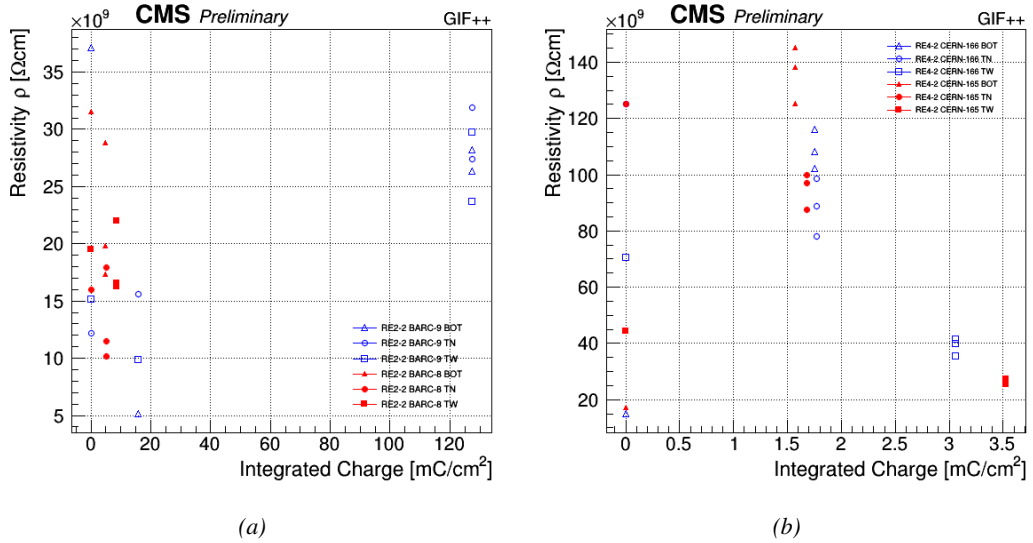


Figure 4.22: Evolution of the Bakelite resistivity for RE2 (4.22a) and RE4 (4.22b) detectors. Both irradiated (blue) and non-irradiated (red) chambers are shown.

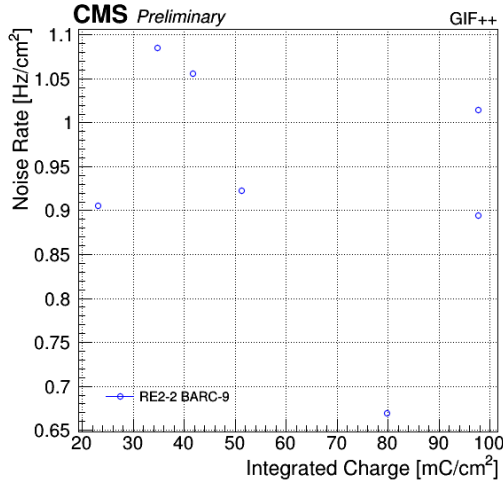


Figure 4.23: Evolution of the noise rate per unit area for the irradiated chamber RE2-2-BARC-9 only.

4.4.1 Description of the Data Acquisition

For the longevity studies, four spare chambers of the present system are used. Two spare RPCs of the RE2,3 stations as well as two spare RPCs from the new RE4 stations have been mounted in a Trolley. Six RE4 gaps are also placed in the trolley. The trolley is placed inside the GIFT++ in the upstream region of the bunker, taking the cesium source as a reference. The trolley is oriented for the detection surface of the chambers to be orthogonal to the beam line. The system can be moved along the orthogonal plane in order to have the beam in all η -partitions. For the aging the trolley is

1213 moved outside the beam line and is placed in a distance of 5.2 m to the source, which irradiates the
 1214 bunker using an attenuation filter of 2.2 which corresponds to a fluence of 10^7 gamma/cm^2 .

1215 During GIF++ operation, the data collected can be divided into different categories as several
 1216 parameters are monitored in addition to the usual RPC performance data. On one hand, to know
 1217 the performance of a chamber, it is need to measure its efficiency and to know the background
 1218 conditions in which it is operated. To do this, the hit signals from the chamber are recorded and
 1219 stored in a ROOT file via a Data Acquisition (DAQ) software. On the other hand, it is also very
 1220 important to monitor parameters such as environmental pressure and temperature, gas temperature
 1221 and humidity, RPC HV, LV, and currents, or even source and beam status. This is done through the
 1222 GIF++ web Detector Control Software (DCS) that stores this information in a database.

1223 Two different types of tests are conducted on RPCs via the DAQ. Indeed, the performance of the
 1224 detectors is measured periodically during dedicated test beam periods using the H4 muon beam. In
 1225 between these test beam periods, when the beam is not available, the chambers are irradiated by the
 1226 ^{137}Cs in order to accumulate deposited charge and the gamma background is measured.

1227 RPCs under test are connected through LVDS cables to V1190A Time-to-Digital Converter
 1228 (TDC) modules manufactured by CAEN. These modules, located in the rack area outside of the
 1229 bunker, get the logic signals sent by the chambers and save them into their buffers. Due to the
 1230 limited size of the buffers, the collected data is regularly erased and replaced. A trigger signal is
 1231 needed for the TDC modules to send the useful data to the DAQ computer via a V1718 CAEN USB
 1232 communication module.

1233 In the case of performance test, the trigger signal used for data acquisition is generated by the
 1234 coincidence of three scintillators. A first one is placed upstream outside of the bunker, a second one
 1235 is placed downstream outside of the bunker, while a third one is placed in front of the trolley, close by
 1236 the chambers. Every time a trigger is sent to the TDCs, i.e. every time a muon is detected, knowing
 1237 the time delay in between the trigger and the RPC signals, signals located in the right time window
 1238 are extracted from the buffers and saved for later analysis. Signals are taken in a time window of
 1239 400 ns centered on the muon peak (here we could show a time spectrum). On the other hand, in the
 1240 case of background rate measurement, the trigger signal needs to be "random" not to measure muons
 1241 but to look at gamma background. A trigger pulse is continuously generated at a rate of 300 Hz using
 1242 a dual timer. To integrate an as great as possible time, all signals contained within a time window of
 1243 10us prior to the random trigger signal are extracted form the buffers and saved for further analysis
 1244 (here another time spectrum to illustrate could be useful, maybe even place both spectrum together
 1245 as a single Figure).

1246 The signals sent to the TDCs correspond to hit collections in the RPCs. When a particle hits
 1247 a RPC, it induce a signal in the pickup strips of the RPC readout. If this signal is higher than the
 1248 detection threshold, a LVDS signal is sent to the TDCs. The data is then organised into 4 branches
 1249 keeping track of the event number, the hit multiplicity for the whole setup, and the time and channel
 1250 profile of the hits in the TDCs.

1251 **4.4.2 RPC current, environmental and operation parameter monitoring**

1252 In order to take into account the variation of pressure and temperature between different data taking
 1253 periods the applied voltage is corrected following the relationship :

$$1254 \quad HV_{eff} = HV_{app} \times \left(0.2 + 0.8 \cdot \frac{P_0}{P} \times \frac{T}{T_0} \right) \quad (4.10)$$

1254 where T_0 (=293 K) and P_0 (=990 mbar) are the reference values.

1255 **4.4.3 Measurement procedure**

1256 Insert a short description of the online tools (DAQ, DCS, DQM).

1257 Insert a short description of the offline tools : tracking and efficiency algorithm.

1258 Identify long term aging effects we are monitoring the rates per strip.

1259 **4.4.4 Longevity studies results**

5

1260

1261

Investigation on high rate RPCs

1262 **5.1 Rate limitations and ageing of RPCs**

1263 **5.1.1 Low resistivity electrodes**

1264 **5.1.2 Low noise front-end electronics**

1265 **5.2 Construction of prototypes**

1266 **5.3 Results and discussions**

6

1267

1268

Conclusions and outlooks

¹²⁶⁹ **6.1 Conclusions**

¹²⁷⁰ **6.2 Outlooks**

A

1271

A data acquisition software for CAEN VME TDCs

1272

1273 Certifying detectors in the perspective of HL-LHC required to develop tools for the GIF++ experiment. Among them was the C++ Data Acquisition (DAQ) software that allows to make the communications in between a computer and TDC modules in order to retrieve the RPC data [57]. In this 1274 appendix, details about this software, as of how the software was written, how it functions and how 1275 it can be exported to another similar setup, will be given.

A.1 GIF++ DAQ file tree

1276 GIF++ DAQ source code is fully available on github at https://github.com/afagot/GIF_DAQ. The software requires 3 non-optional dependencies:

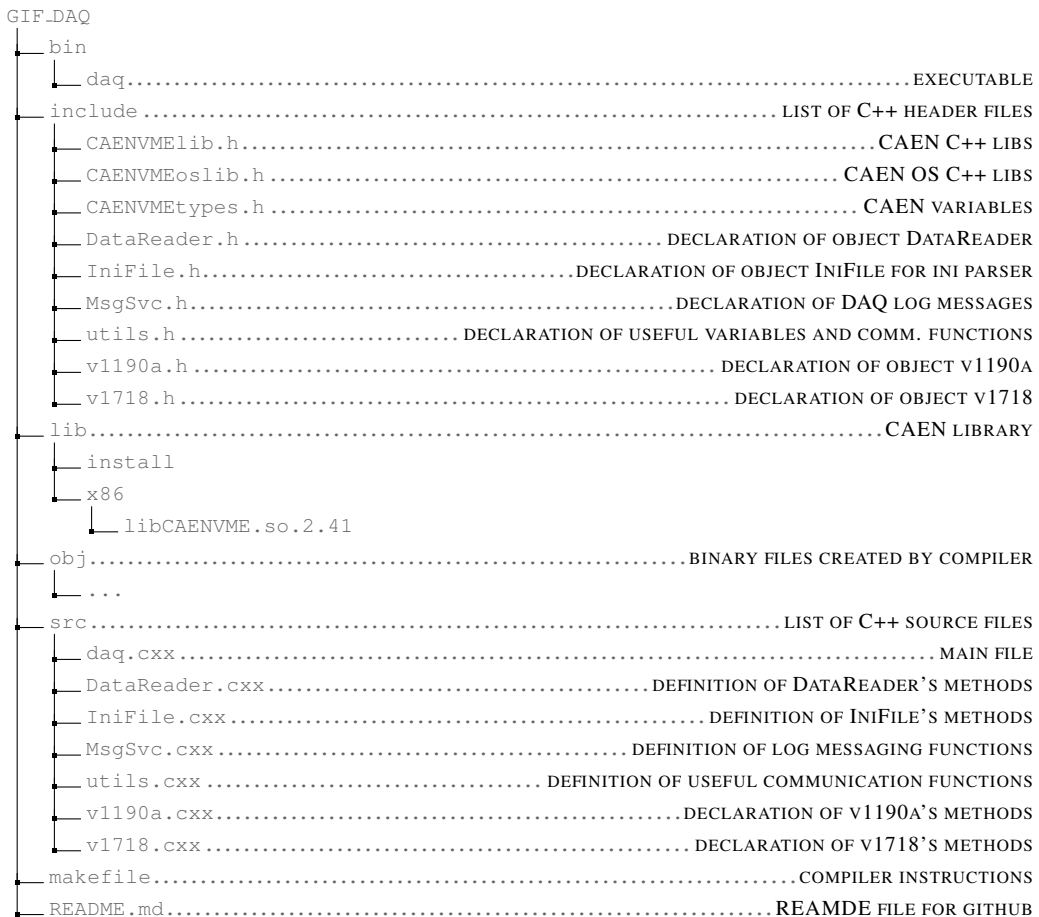
- 1277
- 1278 • CAEN USB Driver, to mount the VME hardware,
 - 1279 • CAEN VME Library, to communicate with the VME hardware, and
 - 1280 • ROOT, to organize the collected data into a TTree.

1281 The CAEN VME library will not be packaged by distributions and will need to be installed man-
1282 ually. To compile the GIF++ DAQ project via a terminal, from the DAQ folder use the command:

1283
1284 make

1285 The source code tree is provided below along with comments to give an overview of the files' con-
1286 tent. The different objects created for this project (`v1718`, `v1190a`, `IniFile` & `DataReader`) will be
1287 described in details in the following sections.

1288



1293 A.2 Usage of the DAQ

1294 GIF++ DAQ, as used in GIF++, is not a standalone software. Indeed, the system being more complexe,
 1295 the DAQ only is a sub-layer of the software architecture developped to control and monitor
 1296 the RPCs that are placed into the bunker for performance study in an irradiated environment. The top
 1297 layer of GIF++ is a Web Detector Control System (webDCS) application. The DAQ is only called
 1298 by the webDCS when data needs to be acquired. The webDCS operates the DAQ through command
 1299 line. To start the DAQ, the webDCS calls:

1300
 1301 bin/daq /path/to/the/log/file/in/the/output/data/folder

1302 where /path/to/the/log/file/in/the/output/data/folder is the only argument required. This
 1303 log file is important for the webDCS as this file contains all the content of the communication of the
 1304 webDCS and the different systems monitored by the webDCS. Its content is constantly displayed
 1305 during data taking for the users to be able to follow the operations. The communication messages
 1306 are normally sent to the webDCS log file via the functions declared in file MsgSvc.h, typically
 1307 MSG_INFO(string message).

1308

1309 A.3 Description of the readout setup

1310 The CMS RPC setup at GIF++ counts 5 V1190A Time-to-Digital Converter (TDC) manufactured
 1311 by CAEN [58]. V1190A are VME units accepting 128 independent Multi-Hit/Multi-Event TDC
 1312 channels whose signals are treated by 4 100 ps high performance TDC chips developed by CERN
 1313 / ECP-MIC Division. The communication between the computer and the TDCs to transfer data is
 1314 done via a V1718 VME master module also manufactured by CAEN and operated from a USB
 1315 port [59]. These VME modules are all hosted into a 6U VME 6021 powered crate manufactured by
 1316 W-Ie-Ne-R than can accommodate up to 21 VME bus cards [60]. These 3 components of the DAQ
 1317 setup are shown in Figure A.1.

1318

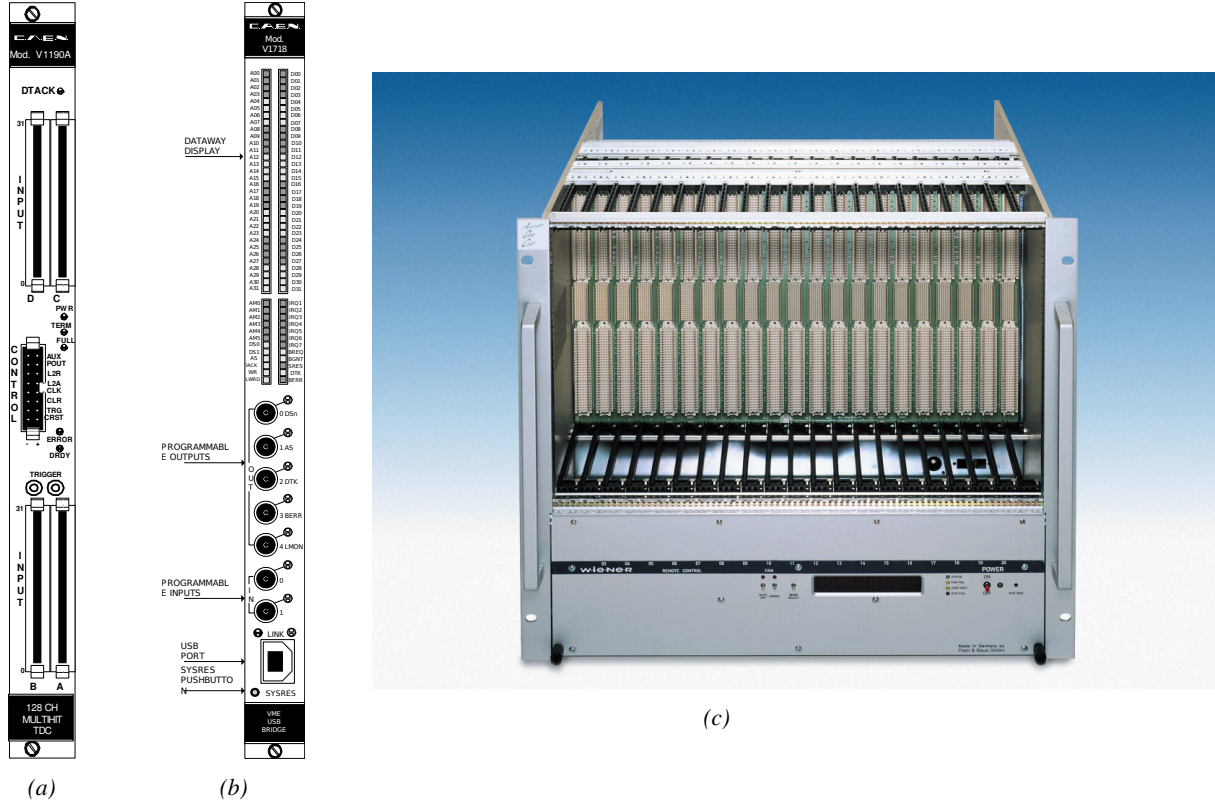


Figure A.1: (A.1a) View of the front panel of a V1190A TDC module [58]. (A.1b) View of the front panel of a V1718 Bridge module [59]. (A.1c) View of the front panel of a 6U 6021 VME crate [60].

1319

A.4 Data read-out

1320 To efficiently perform a data readout algorithm, C++ objects to handle the VME modules (TDCs
 1321 and VME bridge) have been created along with objects to store data and read the configuration file

1322 that comes as an input of the DAQ software.

1323

1324 A.4.1 V1190A TDCs

1325 The DAQ used at GIF takes profit of the *Trigger Matching Mode* offered by V1190A modules.
 1326 This setting is enabled through the method `v1190a::SetTrigMatching (int ntdcs)` where `ntdcs`
 1327 is the total number of TDCs in the setup this setting needs to be enabled for (Source Code A.1). A
 1328 trigger matching is performed in between a trigger time tag, a trigger signal sent into the TRIGGER
 1329 input of the TDC visible on Figure A.1a, and the channel time measurements, signals recorded from
 1330 the detectors under test in our case. Control over this data acquisition mode, explained through
 1331 Figure A.2, is offered via 4 programmable parameters:

- 1332 • **match window:** the matching between a trigger and a hit is done within a programmable time
 1333 window. This is set via the method

1334 `void v1190a::SetTrigWindowWidth(Uint windowHeight, int ntdcs)`

- 1335 • **window offset:** temporal distance between the trigger tag and the start of the trigger matching
 1336 window. This is set via the method

1337 `void v1190a::SetTrigWindowWidth(Uint windowHeight, int ntdcs)`

- 1338 • **extra search margin:** an extended time window is used to ensure that all matching hits are
 1339 found. This is set via the method

1340 `void v1190a::SetTrigSearchMargin(Uint searchMargin, int ntdcs)`

- 1341 • **reject margin:** older hits are automatically rejected to prevent buffer overflows and to speed
 1342 up the search time. This is set via the method

1343 `void v1190a::SetTrigRejectionMargin(Uint rejectMargin, int ntdcs)`

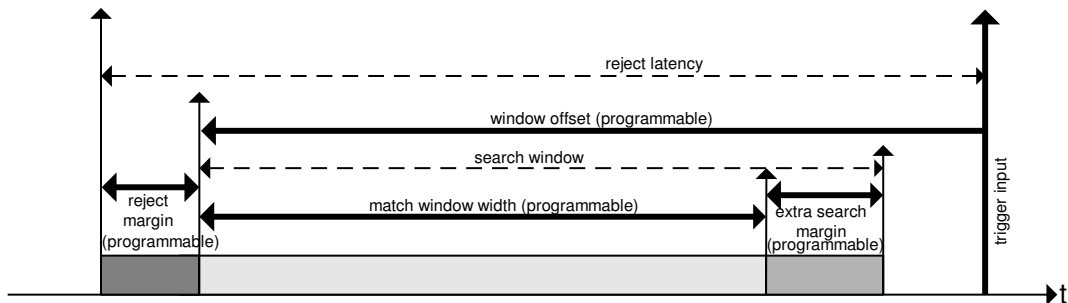


Figure A.2: Module V1190A Trigger Matching Mode timing diagram [58].

1344 Each of these 4 parameters are given in number of clocks, 1 clock being 25 ns long. It is easy to
 1345 understand at this level that there are 3 possible functioning settings:

- 1346 • **1:** the match window is entirely contained after the trigger signal,

- 1347 • **2:** the match window overlaps the trigger signal, or

- 1348 • **3:** the match window is entirely contained before the trigger signal as displayed on Figure A.2.

1349 In both the first and second cases, the sum of the window width and of the offset can be set to
1350 a maximum of 40 clocks, which corresponds to 1 μ s. Evidently, the offset can be negative, allowing
1351 for a longer match window, with the constraint of having the window ending at most 1 μ s after the
1352 trigger signal. In the third case, the maximum negative offset allowed is of 2048 clocks (12 bit) cor-
1353 responding to 51.2 μ s, the match window being strictly smaller than the offset. In the case of GIF++,
1354 the choice has been made to use this last setting by delaying the trigger signal. During the studies
1355 performed in GIF++, both the efficiency of the RPCs, probed using a muon beam, and the noise or
1356 gamma background rate are monitored. The extra search and reject margins are left unused.
1357 To probe the efficiency of RPC detectors, the trigger time tag is provided by the coïncidence of
1358 scintillators when a bunch of muons passes through GIF++ area is used to trigger the data acquisi-
1359 tion. For this measurement, it is useful to reduce the match window width only to contain the muon
1360 information. Indeed, the delay in between a trigger signal and the detection of the corresponding
1361 muon in the RPC being very contant (typically a few tens of ns due to jitter and cable length), the
1362 muon signals are very localised in time. Thus, due to a delay of approximalety 325 ns in between
1363 the muons and the trigger, the settings where chosen to have a window width of 24 clocks (600 ns)
1364 centered on the muon peak thanks to a negative offset of 29 clocks (725 ns).
1365 On the otherhand, monitoring the rates don't require for the DAQ to look at a specific time window.
1366 It is important to integrate enough time to have a robust measurement of the rate as the number of
1367 hits per time unit. The triggerring signal is provided by a pulse generator at a frequency of 300 Hz
1368 to ensure that the data taking occurs in a random way, with respect to beam physics, to probe only
1369 the irradiation spectrum on the detectors. The match window is set to 400 clocks (10 μ s) and the
1370 negative offset to 401 clocks as it needs to exceed the value of the match window.

```

1371
class v1190a
{
    private :
        long             Handle;
        vector<Data32>   Address;
        CVDataWidth      DataWidth;
        CVAddressModifier AddressModifier;

    public:

        v1190a(long handle, IniFile *inifile, int ntdcs);
        ~v1190a();
        Data16 write_op_reg(Data32 address, int code, string error);
        Data16 read_op_reg(Data32 address, string error);
        void Reset(int ntdcs);
        void Clear(int ntdcs);
        void TestWR(Data16 value,int ntdcs);
        void CheckTDCStatus(int ntdcs);
        void CheckCommunication(int ntdcs);
        void SetTDCTestMode(Data16 mode,int ntdcs);
        void SetTrigMatching(int ntdcs);
        void SetTrigTimeSubtraction(Data16 mode,int ntdcs);
        void SetTrigWindowWidth(Uint windowHeight,int ntdcs);
        void SetTrigWindowOffset(Uint windowOffset,int ntdcs);
        void SetTrigSearchMargin(Uint searchMargin,int ntdcs);
        void SetTrigRejectionMargin(Uint rejectMargin,int ntdcs);
        void GetTrigConfiguration(int ntdcs);
        void SetTrigConfiguration(IniFile *inifile,int ntdcs);
        void SetTDCDetectionMode(Data16 mode,int ntdcs);
        void SetTDCResolution(Data16 lsb,int ntdcs);
        void SetTDCDeadTime(Data16 time,int ntdcs);
        void SetTDCHeadTrailer(Data16 mode,int ntdcs);
        void SetTDCEventSize(Data16 size,int ntdcs);
        void SwitchChannels(IniFile *inifile,int ntdcs);
        void SetIRQ(Data32 level, Data32 count,int ntdcs);
        void SetBlockTransferMode(Data16 mode,int ntdcs);
        void Set(IniFile *inifile,int ntdcs);
        void CheckStatus(CVErrorCodes status) const;
        int ReadBlockD32(Uint tdc, const Data16 address,
                         Data32 *data, const Uint words, bool ignore_berr);
        Uint Read(RAWData *DataList,int ntdcs);
};

1372

```

1373 *Source Code A.1: Description of C++ object v1190a.*

1374 The v1190a object, defined in the DAQ software as in Source Code A.1, offers the possibility to
 1375 concatenate all TDCs in the readout setup into a single object containing a list of hardware addresses
 1376 (addresses to access the TDCs' buffer through the VME crate) and each constructor and method acts
 1377 on the list of TDCs.

1378

1379 A.4.2 DataReader

1380 Enabled thanks to v1190a::SetBlockTransferMode(Data16 mode, int ntdcs), the data transfer
 1381 is done via Block Transfer (BLT). Using BLT allows to tranfer a fixed number of events called a
 1382 *block*. This is used together with an Almost Full Level (AFL) of the TDCs' output buffers, defined

1383 through `v1190a::SetIRQ(Data32 level, Data32 count, int ntdcs)`. This AFL gives the maximum amount of 32735 words (16 bits, corresponding to the depth of a TDC output buffer) that can
 1384 written in a buffer before an Interrupt Request (IRQ) is generated and seen by the VME Bridge,
 1385 stopping the data acquisition to transfer the content of each TDC buffers before resuming. For each
 1386 trigger, 6 words or more are written into the TDC buffer:

- 1388 • a **global header** providing information of the event number since the beginning of the data
 1389 acquisition,
- 1390 • a **TDC header**,
- 1391 • the **TDC data** (*if any*), 1 for each hit recorded during the event, providing the channel and the
 1392 time stamp associated to the hit,
- 1393 • a **TDC error** providing error flags,
- 1394 • a **TDC trailer**,
- 1395 • a **global trigger time tag** that provides the absolute trigger time relatively to the last reset,
 1396 and
- 1397 • a **global trailer** providing the total word count in the event.

1398 As previously described in Section ??, CMS RPC FEEs provide us with 100 ns long LVDS output
 1399 signals that are injected into the TDCs' input. Any avalanche signal that gives a signal above the
 1400 FEEs threshold is thus recorded by the TDCs as a hit within the match window. Each hit is assigned
 1401 to a specific TDC channel with a time stamp, with a precision of 100 ps. The reference time, $t_0 = 0$,
 1402 is provided by the beginning of the match window. Thus for each trigger, coming from a scintillator
 1403 coïncidence or the pulse generator, a list of hits is stored into the TDCs' buffers and will then be
 1404 transferred into a ROOT Tree.

1405 When the BLT is used, it is easy to understand that the maximum number of words that have
 1406 been set as ALF will not be a finite number of events or, at least, the number of events that would
 1407 be recorded into the TDC buffers will not be a multiple of the block size. In the last BLT cycle to
 1408 tranfer data, the number of events to transfer will most probably be lower than the block size. In that
 1409 case, the TDC can add fillers at the end of the block but this option requires to send more data to the
 1410 computer and is thus a little slower. Another solution is to finish the transfer after the last event by
 1411 sending a bus error that states that the BLT reached the last event in the pile. This method has been
 1412 chosen in GIF++.

1414 Due to irradiation, an event in GIF++ can count up to 300 words per TDC. A limit of 4096 words
 1415 (12 bits) has been set to generate IRQ which represent from 14 to almost 700 events depending on
 1416 the average of hits collected per event. Then the block size has been set to 100 events with enabled
 1417 bus errors. When an AFL is reached for one of the TDCs, the VME bridge stops the acquisition by
 1418 sending a BUSY signal.

1420

```
1421 The data is then transferred one TDC at a time into a structure called RAWData (Source Code A.2).  
1422  
1423 struct RAWData{  
    vector<int> *EventList;  
    vector<int> *NHitsList;  
    vector<int> *QFlagList;  
    vector<vector<int> > *ChannelList;  
    vector<vector<float> > *TimeStampList;  
};
```

Source Code A.2: Description of data holding C++ structure RAWData.

In order to organize the data transfer and the data storage, an object called `DataReader` was created (Source Code A.3). On one hand, it has `v1718` and `v1190a` objects as private members for communication purposes, such as VME modules settings via the configuration file `*iniFile` or data read-out through `v1190a::Read()` and on the other hand, it contains the struture `RAWData` that allows to organise the data in vectors reproducing the tree structure of a ROOT file.

```
1430
class DataReader
{
    private:
        bool      StopFlag;
        IniFile *iniFile;
        Data32   MaxTriggers;
        v1718   *VME;
        int       nTDCs;
        v1190a  *TDCs;
        RAWData  TDCData;

    public:
        DataReader();
        virtual ~DataReader();
        void     SetIniFile(string inifilename);
        void     SetMaxTriggers();
        Data32   GetMaxTriggers();
        void     SetVME();
        void     SetTDC();
        int      GetQFlag(Uint it);
        void     Init(string inifilename);
        void     FlushBuffer();
        void     Update();
        string   GetFileName();
        void     WriteRunRegistry(string filename);
        void     Run();
};

1431
```

Source Code A.3: Description of C++ object DataReader.

1433 Each event is transferred from `TDCData` and saved into branches of a ROOT `TTree` as 3 integers
1434 that represent the event ID (`EventCount`), the number of hits read from the TDCs (`nHits`), and the
1435 quality flag that provides information for any problem in the data transfer (`qflag`), and 2 lists of
1436 `nHits` elements containing the fired TDC channels (`TDCCH`) and their respective time stamps (`TDCTS`),
1437 as presented in Source Code A.4. The ROOT file file is named using information contained into
1438 the configuration file, presented in section A.5.2. The needed information is extracted using method
1439 `DataReader::GetFileName()` and allow to build the output filename format `ScanXXXXXX_HVX_DAQ.root`

1440 where ScanXXXXXX is a 6 digit number representing the scan number into GIFT++ database and HVX
 1441 the HV step within the scan that can be more than a single digit. An example of ROOT data file is
 1442 provided with Figure A.3.

```
1443
RAWData TDCData;
TFile *outputFile = new TFile(outputFileName.c_str(),"recreate");
TTree *RAWDataTree = new TTree("RAWData","RAWData");

int EventCount = -9;
int nHits = -8;
int qflag = -7;
vector<int> TDCCh;
vector<float> TDCTS;

RAWDataTree->Branch("EventNumber",&EventCount, "EventNumber/I");
RAWDataTree->Branch("number_of_hits",&nHits,"number_of_hits/I");
RAWDataTree->Branch("Quality_flag",&qflag,"Quality_flag/I");
RAWDataTree->Branch("TDC_channel",&TDCCh);
RAWDataTree->Branch("TDC_TimeStamp",&TDCTS);

1444
//...
//Here read the TDC data using v1190a::Read() and place it into
//TDCData for as long as you didn't collect the requested amount
//of data.
//...

for(Uint i=0; i<TDCData.EventList->size(); i++){
    EventCount = TDCData.EventList->at(i);
    nHits = TDCData.NHitsList->at(i);
    qflag = TDCData.QFlagList->at(i);
    TDCCh = TDCData.ChannelList->at(i);
    TDCTS = TDCData.TimeStampList->at(i);
    RAWDataTree->Fill();
}
```

1445 *Source Code A.4: Highlight of the data transfer and organisation within DataReader::Run() after the data has been collected into TDCData.*

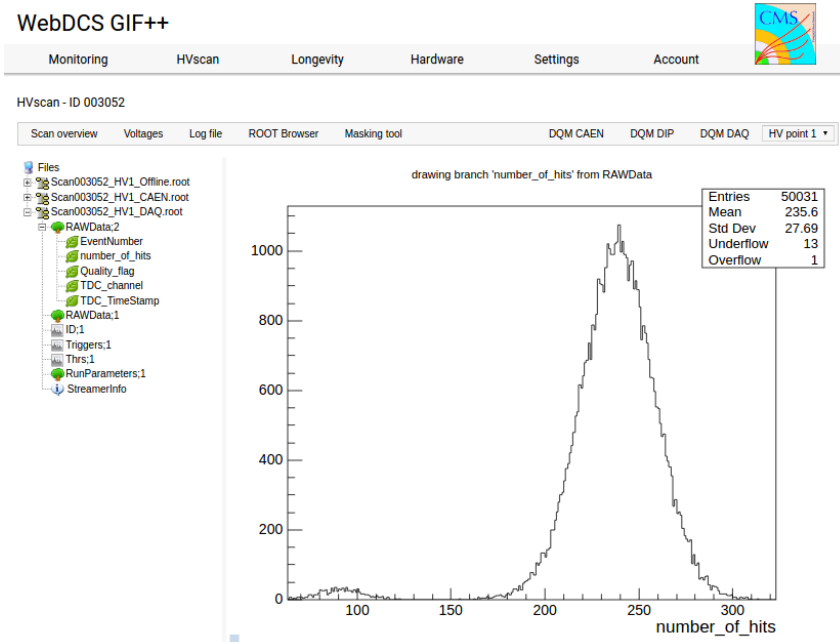


Figure A.3: Structure of the ROOT output file generated by the DAQ. The 5 branches (EventNumber, number_of_hits, Quality_flag, TDC_channel and TDC_TimeStamp) are visible on the left panel of the ROOT browser. On the right panel is visible the histogram corresponding to the variable nHits. In this specific example, there were approximately 50k events recorded to measure the gamma irradiation rate on the detectors. Each event is stored as a single entry in the TTree.

1446 A.4.3 Data quality flag

1447 Among the parameters that are recorded for each event, the quality flag, defined in Source Code A.5,
 1448 is determined on the fly by checking the data recorded by every single TDC. From method `v1190a::Read()`,
 1449 it can be understood that the content of each TDC buffer is readout one TDC at a time. Entries are
 1450 created in the data list for the first TDC and then, when the second buffer is readout, events corre-
 1451 sponding to entries that have already been created to store data for the previous TDC are added to
 1452 the existing list element. On the contrary, when an event entry has not been yet created in the data
 1453 list, a new entry is created.

```
1454
 1455 typedef enum _QualityFlag {
    GOOD      = 1,
    CORRUPTED = 0
} QualityFlag;
```

1456 *Source Code A.5: Definition of the quality flag `enum`.*

1457 It is possible that each TDC buffer contains a different number of events. In cases where the first
 1458 element in the buffer list is an event for corresponds to a new entry, the difference in between the
 1459 entry from the buffer and the last entry in the data list is recorded and checked. If it is greater than 1,
 1460 what should never be the case, the quality flag is set to CORRUPTED for this TDC and an empty entry
 1461 is created in the place of the missing ones. Missing entries are believe to be the result of a bad hold

1462 on the TDC buffers at the moment of the readout. Indeed, the software hold is effective only on 1
 1463 TDC at a time and no solution as been found yet to completely block the writting in the buffers when
 1464 an IRQ is received.

1465 At the end of each BLT cycle, the ID of the last entry stored for each TDC buffer is not recorded.
 1466 When starting the next cycle, if the first entry in the pile corresponds to an event already existing
 1467 in the list, the readout will start from this list element and will not be able to check the difference
 1468 in between this entry's ID and the one of the last entry that was recorded for this TDC buffer in
 1469 the previous cycle. In the case events were missing, the flag stays at its initial value of 0, which is
 1470 similar to CORRUPTED and it is assumed that then this TDC will not contribute to `number_of_hits`,
 1471 `TDC_channel` or `TDC_TimeStamp`.

1472 Finally, since there will be 1 `RAWData` entry per TDC for each event (meaning `nTDCs` entries,
 1473 referring to `DataReader` private attribute), the individual flags of each TDC will be added together.
 1474 The final format is an integer composed `nTDCs` digits where each digit is the flag of a specific TDC.
 1475 This is constructed using powers of 10 like follows:

```
1476     TDC 0: QFlag = 100 × _QualityFlag
1477     TDC 1: QFlag = 101 × _QualityFlag
1478     ...
1479     TDC N: QFlag = 10N × _QualityFlag
```

1480 and the final flag to be with N digits:

```
1481     QFlag = n....3210
```

1482 each digit being 1 or 0. Below is given an example with a 4 TDCs setup.

1483 If all TDCs were good : `QFlag = 1111`,

1484 but if TDC 2 was corrupted : `QFlag = 1011`.

1485 When data taking is over and the data contained in the dynamical `RAWData` structure is transferred
 1486 to the ROOT file, all the 0s are changed into 2s by calling the method `DataReader::GetQFlag()`.
 1487 This will help translating the flag without knowing the number of TDCs beforehand. Indeed, a flag
 1488 111 could be due to a 3 TDC setup with 3 good individual TDC flags or to a more than 3 TDC setup
 1489 with TDCs those ID is greater than 2 being CORRUPTED, thus giving a 0.

1490 The quality flag has been introduced quite late, in October 2017 only, to the list of GIFT++ DAQ
 1491 parameters to be recorded into the output ROOT file. Before this addition, the missing data, corrupting
 1492 the quality for the offline analysis, was contributing to artificially fill data with lower multiplicity.
 1493 Looking at `TBranch number_of_hits` provides an information about the data of the full GIFT++
 1494 setup. When a TDC is not able to transfer data for a specific event, the effect is a reduction of the
 1495 total number of hits recorded in the full setup, this is what can be seen from Figure A.4. After offline
 1496 reconstruction detector by detector, the effect of missing events can be seen in the artificially filled
 1497 bin at multiplicity 0 shown in Figure A.5. Nonetheless, for data with high irradiation levels, as it is
 1498 the case for Figure A.5a, discarding the fake multiplicity 0 data can be done easily during the offline
 1499 analysis. At lower radiation, the missing events contribution becomes more problematic as the multi-
 1500 tiplicity distribution overlaps the multiplicity 0 and that in the same time the proportion of missing

1501 events decreases. Attempts to fit the distribution with a Poisson or skew distribution function were
 1502 not conclusive and this very problem has been at the origin of the quality flag that allows to give a
 1503 non ambiguous information about each event quality.

1504

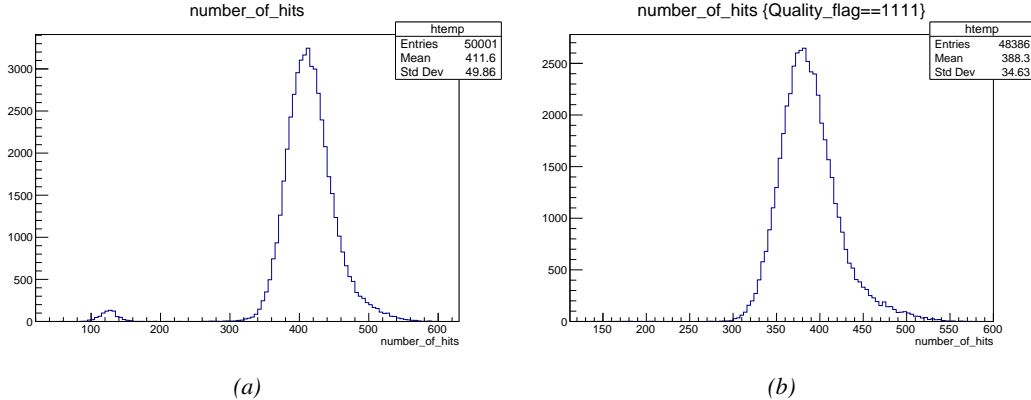


Figure A.4: The effect of the quality flag is explained by presenting the content of TBranch `number_of_hits` of a data file without `Quality_flag` in Figure A.4a and the content of the same TBranch for data corresponding to a `Quality_flag` where all TDCs were labelled as `GOOD` in Figure A.4b taken with similar conditions. It can be noted that the number of entries in Figure A.4b is slightly lower than in Figure A.4a due to the excluded events.

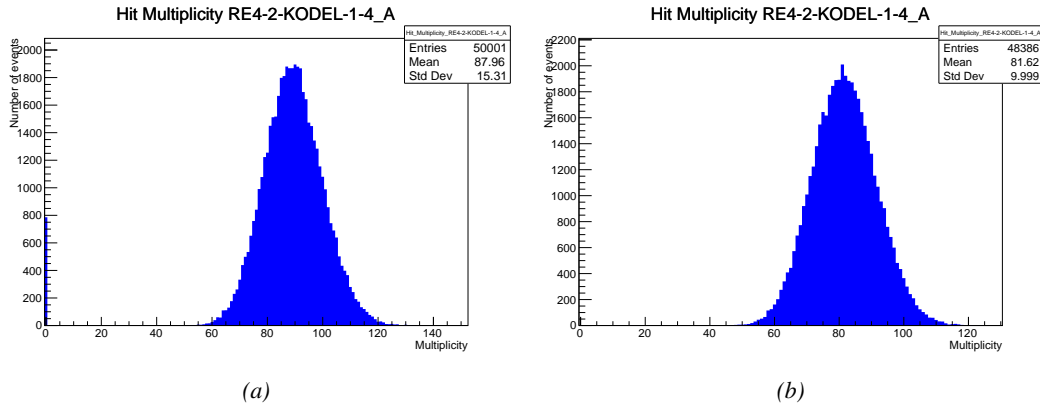


Figure A.5: Using the same data as previously showed in Figure A.4, the effect of the quality flag is explained by presenting the reconstructed hit multiplicity of a data file without `Quality_flag` in Figure A.5a and the reconstructed content of the same RPC partition for data corresponding to a `Quality_flag` where all TDCs were labelled as `GOOD` in Figure A.5b taken with similar conditions. The artificial high content of bin 0 is completely suppressed.

1505

A.5 Communications

1506 To ensure data readout and dialog in between the machine and the TDCs or in between the webDCS
 1507 and the DAQ, different communication solutions were used. First of all, it is important to have a

1508 module to allow the communication in between the TDCs and the computer from which the DAQ
 1509 operates. When this communication is effective, shifters using the webDCS to control data taking
 1510 can thus send instructions to the DAQ.

1511

1512 A.5.1 V1718 USB Bridge

1513 In the previous section, the data transfer has been discussed. The importance of the `v1718` object
 1514 (Source Code A.6), used as private member of `DataReader`, was not explicated. VME master
 1515 modules are used for communication purposes as they host the USB port that connects the pow-
 1516 ered crate buffer to the computer where the DAQ is installed. From the source code point of view,
 1517 this object is used to control the communication status, by reading the returned error codes with
 1518 `v1718::CheckStatus()`, or to check for IRQs coming from the TDCs through `v1718::CheckIRQ()`.
 1519 Finally, to ensure that triggers are blocked at the hardware level, a NIM pulse is sent out of one of the
 1520 5 programmable outputs (`v1718::SendBUSY()`) to the VETO of the coincidence module where the
 1521 trigger signals originate from. As long as this signal is ON, no trigger can reach the TDCs anymore.
 1522

```
1523
  class v1718{
    private:
      int Handle;
      Data32 Data;           // Data
      CVIRQLevels Level;    // Interrupt level
      CVAddressModifier AM;   // Addressing Mode
      CVDataWidth dataSize;  // Data Format
      Data32 BaseAddress;    // Base Address

    public:
      v1718(IniFile *inifile);
      ~v1718();
      long GetHandle(void) const;
      int GetData(Data16 data);
      Data16 GetData(void);
      int SetLevel(CVIRQLevels level);
      CVIRQLevels GetLevel(void);
      int SetAM(CVAddressModifier am);
      CVAddressModifier GetAM(void);
      int SetDatasize(CVDataWidth datasize);
      CVDataWidth GetDataSize(void);
      int SetBaseAddress(Data16 baseaddress);
      Data16 GetBaseAddress(void);
      void CheckStatus(CVErrorCodes status) const;
      void CheckIRQ();
      void SetPulsers();
      void SendBUSY(BusyLevel level);
  };

```

1524 *Source Code A.6: Description of C++ object v1718.*

1525 A.5.2 Configuration file

1526 The DAQ software takes as input a configuration file written using INI standard [61]. This file is
 1527 partly filled with the information provided by the shifters when starting data acquisition using the
 1528 webDCS, as shown by Figure A.6. This information is written in section [`General`] and will later

1529 be stored in the ROOT file that contains the DAQ data as can be seen from Figure A.3. Indeed,
 1530 another `TTree` called `RunParameters` as well as the 2 histograms `ID`, containing the scan number,
 1531 start and stop time stamps, and `Triggers`, containing the number of triggers requested by the shifter,
 1532 are available in the data files. Moreover, `ScanID` and `HV` are then used to construct the file name
 1533 thanks to the method `DataReader::GetFileName()`.

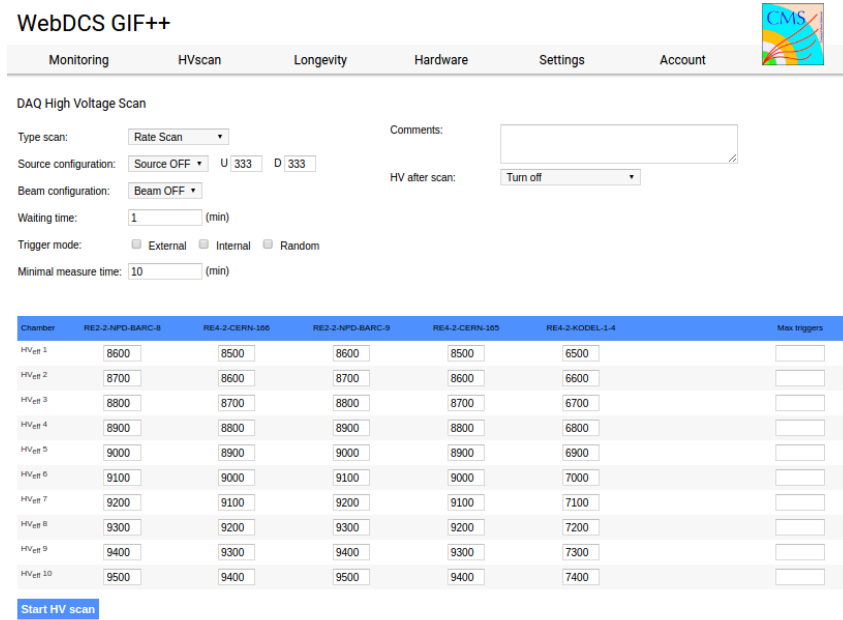


Figure A.6: WebDCS DAQ scan page. On this page, shifters need to choose the type of scan (Rate, Efficiency or Noise Reference scan), the gamma source configuration at the moment of data taking, the beam configuration, and the trigger mode. These information will be stored in the DAQ ROOT output. Are also given the minimal measurement time and waiting time after ramping up of the detectors is over before starting the data acquisition. Then, the list of HV points to scan and the number of triggers for each run of the scan are given in the table underneath.

1534 The rest of the information is written beforehand in the configuration file template, as explicated
 1535 in Source Code A.7, and contains the hardware addresses to the different VME modules in the
 1536 setup as well as settings for the TDCs. As the TDC settings available in the configuration file are not
 1537 supposed to be modified, an improvement would be to remove them from the configuration file and
 1538 to hardcode them inside of the DAQ code itself or to place them into a different INI file that would
 1539 host only the TDC settings to lower the probability for a bad manipulation of the configuration file
 1540 that can be modified from one of webDCS' menus.

1541

```

[General]
TdcS=4
ScanID=$scanid
HV=$HV
RunType=$runtype
MaxTriggers=$maxtriggers
Beam=$beam
[VMEInterface]
Type=V1718
BaseAddress=0xFF0000
Name=VmeInterface
[TDC0]
Type=V1190A
BaseAddress=0x00000000
Name=Tdc0
StatusA00-15=1
StatusA16-31=1
StatusB00-15=1
StatusB16-31=1
StatusC00-15=1
StatusC16-31=1
StatusD00-15=1
StatusD16-31=1
[TDC1]
Type=V1190A
BaseAddress=0x11110000
Name=Tdc1
StatusA00-15=1
StatusA16-31=1
StatusB00-15=1
StatusB16-31=1
StatusC00-15=1
StatusC16-31=1
StatusD00-15=1
StatusD16-31=1
[TDC2]
Type=V1190A
BaseAddress=0x22220000
Name=Tdc2
StatusA00-15=1
StatusA16-31=1
StatusB00-15=1
StatusB16-31=1
StatusC00-15=1
StatusC16-31=1
StatusD00-15=1
StatusD16-31=1
[TDC3]
Type=V1190A
BaseAddress=0x44440000
Name=Tdc3
StatusA00-15=1
StatusA16-31=1
StatusB00-15=1
StatusB16-31=1
StatusC00-15=1
StatusC16-31=1
StatusD00-15=1
StatusD16-31=1
[TDCSettings]
TriggerExtraSearchMargin=0
TriggerRejectMargin=0
TriggerTimeSubtraction=0b1
TdcDetectionMode=0b01
TdcResolution=0b10
TdcDeadTime=0b00
TdcHeadTrailer=0b1
TdcEventSize=0b1001
TdcTestMode=0b0
BLTMode=1

```

1542

Source Code A.7: INI configuration file template for 4 TDCs. In section [General], the number of TDCs is explicitated and information about the ongoing run is given. Then, there are sections for each and every VME modules. There buffer addresses are given and for the TDCs, the list of channels to enable is given. Finally, in section [TDCSettings], a part of the TDC settings are given.

1544 In order to retrieve the information of the configuration file, the object `IniFile` has been developed
 1545 to provide an INI parser, presented in Source Code A.8. It contains private methods returning a
 1546 boolean to check the type of line written in the file, whether a comment, a group header or a key line
 1547 (`IniFile::CheckIfComment()`, `IniFile::CheckIfGroup()` and `IniFile::CheckIfToken()`). The
 1548 key may sometimes be referred to as *token* in the source code. Moreover, the private element
 1549 `FileData` is a map of `const string` to `string` that allows to store the data contained inside the
 1550 configuration file via the public method `IniFile::GetFileData()` following the formatting (see
 1551 method `IniFile::Read()`):

```
1552
  1553     string group, token, value;
  // Get the field values for the 3 strings.
  // Then concatenate group and token together as a single string
  // with a dot separation.
  token = group + "." + token;
  FileData[token] = value;
```

1554 More methods have been written to translate the different keys into the right variable format
 1555 when used by the DAQ. For example, to get a `float` value out of the configuration file data, knowing
 1556 the group and the key needed, the method `IniFile::floatType()` can be used. It takes 3 arguments
 1557 being the group name and key name (both `string`), and a default `float` value used as exception in
 1558 the case the expected combination of group and key cannot be found in the configuration file. This
 1559 default value is then used and the DAQ continues on working after sending an alert in the log file for
 1560 further debugging.

```

1561 typedef map< const string, string > IniFileData;
1562
class IniFile{
    private:
        bool          CheckIfComment (string line);
        bool          CheckIfGroup(string line, string& group);
        bool          CheckIfToken(string line, string& key, string& value);
        string         FileName;
        IniFileData   FileData;
        int           Error;

    public:
        IniFile();
        IniFile(string filename);
        virtual      ~IniFile();

        // Basic file operations
        void          SetFileName(string filename);
        int           Read();
        int           Write();
        IniFileData GetFileData();

        // Data readout methods
        Data32         addressType (string groupname, string keyname, Data32
→     defaultvalue);
        long          intType     (string groupname, string keyname, long
→     defaultvalue);
        long long    longType    (string groupname, string keyname, long long
→     defaultvalue );
        string         stringType  (string groupname, string keyname, string
→     defaultvalue );
        float         floatType   (string groupname, string keyname, float
→     defaultvalue );

        // Error methods
        string         GetErrorMsg();
    };

```

1563 *Source Code A.8: Description of C++ object `IniFile` used as a parser for INI file format.*

1564 A.5.3 WebDCS/DAQ intercommunication

1565 When shifters send instructions to the DAQ via the configuration file, it is the webDCS itself that
 1566 gives the start command to the DAQ and then the 2 softwares use inter-process communication
 1567 through file to synchronise themselves. This communication file is represented by the variable **const**
 1568 string __runstatuspath.

1569 On one side, the webDCS sends commands or status that are readout by the DAQ:

- 1570 • INIT, status sent when launching a scan and read via function `CtrlRunStatus(...)`,
- 1571 • START, command to start data taking and read via function `CheckSTART()`,
- 1572 • STOP, command to stop data taking at the end of the scan and read via function `CheckSTOP()`,
 1573 and
- 1574 • KILL, command to kill data taking sent by user and read via function `CheckKILL()`

1575 and on the other, the DAQ sends status that are controled by the webDCS:

- 1576 ● `DAQ_RDY`, sent with `SendDAQReady()` to signify that the DAQ is ready to receive commands
1577 from the webDCS,
- 1578 ● `RUNNING`, sent with `SendDAQRunning()` to signify that the DAQ is taking data,
- 1579 ● `DAQ_ERR`, sent with `SendDAQError()` to signify that the DAQ didn't receive the expected com-
1580 mand from the webDCS or that the launch command didn't have the right number of argu-
1581 ments,
- 1582 ● `RD_ERR`, sent when the DAQ wasn't able to read the communication file, and
- 1583 ● `WR_ERR`, sent when the DAQ wasn't able to write into the communication file.

1584 **A.5.4 Example of inter-process communication cycle**

1585 Under normal conditions, the webDCS and the DAQ processes exchange commands and status via
1586 the file hosted at the address `__runstatuspath`, as explained in subsection A.5.3. An example of
1587 cycle is given in Table A.1. In this example, the steps 3 to 5 are repeated as long as the webDCS tells
1588 the DAQ to take data. A data taking cycle is the equivalent as what is called a *Scan* in GIFT++ jargon,
1589 referring to a set a runs with several HV steps. Each repetition of steps 3 to 5 is then equivalent to a
1590 single *Run*.

1591

1592 At any moment during the data taking, for any reason, the shifter can decide that the data taking
1593 needs to be stopped before it reached the end of the scheduled cycle. Thus at any moment on the
1594 cycle, the content of the inter-process communication file will be changed to `KILL` and the DAQ will
1595 shut down right away. The DAQ checks for `KILL` signals every 5s after the TDCs configuration is
1596 over. So far, the function `CheckKILL()` has been used only inside of the data taking loop of method
1597 `DataReader::Run()` and thus, if the shifter decides to KILL the data taking during the TDC con-
1598 figuration phase or the HV ramping in between 2 HV steps, the DAQ will not be stopped smoothly
1599 and a *force kill* command will be sent to stop the DAQ process that is still awake on the computer.
1600 Improvements can be brought on this part of the software to make sure that the DAQ can safely
1601 shutdown at any moment.

1602

1603 **A.6 Software export**

1604 In section A.2 was discussed the fact that the DAQ as written in its last version is not a standalone
1605 software. It is possible to make it a standalone program that could be adapted to any VME setup
1606 using V1190A and V1718 modules by creating a GUI for the software or by printing the log mes-
1607 sages that are normally printed in the webDCS through the log file, directly into the terminal. This
1608 method was used by the DAQ up to version 3.0 moment where the webDCS was completed. Also, it
1609 is possible to check branches of DAQ v2.X to have example of communication through a terminal.

1610

1611 DAQ v2.X is nonetheless limited in it's possibilities and requires a lot of offline manual interven-
1612 tions from the users. Indeed, there is no communication of the software with the detectors' power
1613 supply system that would allow for a user a predefine a list of voltages to operate the detectors at

step	actions of webDCS	status of DAQ	__runstatuspath
1	launch DAQ ramp voltages ramping over wait for currents stabilization	readout of IniFile configuration of TDCs	INIT
2		configuration done send DAQ ready wait for START signal	DAQ_RDY
3	waiting time over send START		START
4	wait for run to end monitor DAQ run status	data taking ongoing check for KILL signal	RUNNING
5		run over send DAQ_RDY wait for next DCS signal	DAQ_RDY
6	ramp voltages ramping over wait for currents stabilization		DAQ_RDY
3	waiting time over send START		START
4	wait for run to end monitor DAQ run status	update IniFile information data taking ongoing check for KILL signal	RUNNING
5		run over send DAQ_RDY wait for next DCS signal	DAQ_RDY
7	send command STOP	DAQ shuts down	STOP

Table A.1: Inter-process communication cycles in between the webDCS and the DAQ through file string signals.

1614 and loop over to take data without any further manual intervention. In v2.X, the data is taken for a
1615 single detector setting and at the end of each run, the softwares asks the user if he intends on taking
1616 more runs. If so, the software invites the user to set the operating voltages accordingly to what is
1617 necessary and to manual update the configuration file in consequence. This working mode can be a
1618 very first approach before an evolution and has been successfully used by colleagues from different
1619 collaborations.

1620

1621 For a more robust operation, it is recommended to develop a GUI or a web application to inter-
1622 face the DAQ. Moreover, to limit the amount of manual interventions, and thus the probability to
1623 make mistakes, it is also recommended to add an extra feature into the DAQ by installing the HV
1624 Wrapper library provided by CAEN of which an example of use in a similar DAQ software devel-
1625 opped by a master student of UGent, and called TinyDAQ, is provided on UGent's github. Then, this
1626 HV Wrapper will help you communicating with and give instructions to a CAEN HV powered crate
1627 and can be added into the DAQ at the same level where the communication with the user was made
1628 in DAQ v2.X. In case you are using another kind of power system for your detectors, it is stringly
1629 adviced to use HV modules or crates that can be remotely controled via a using C++ libraries.

1630

B

1631

1632

Details on the offline analysis package

1633 The data collected in GIF++ thanks to the DAQ described in Appendix A is difficult to interpret by
1634 a human user that doesn't have a clear idea of the raw data architecture of the ROOT data files. In
1635 order to render the data human readable, a C++ offline analysis tool was designed to provide users
1636 with detector by detector histograms that give a clear overview of the parameters monitored during
1637 the data acquisition [62]. In this appendix, details about this software in the context of GIF++, as of
1638 how the software was written and how it functions will be given.

1639 **B.1 GIF++ Offline Analysis file tree**

1640 GIF++ Offline Analysis source code is fully available on github at https://github.com/afagot/GIF_OfflineAnalysis. The software requires ROOT as non-optionnal dependency
1641 as it takes ROOT files in input and write an output ROOT file containing histograms. To compile the
1642 GIF++ Offline Analysis project is compiled with cmake. To compile, first a build/ directory must
1643 be created to compile from there:

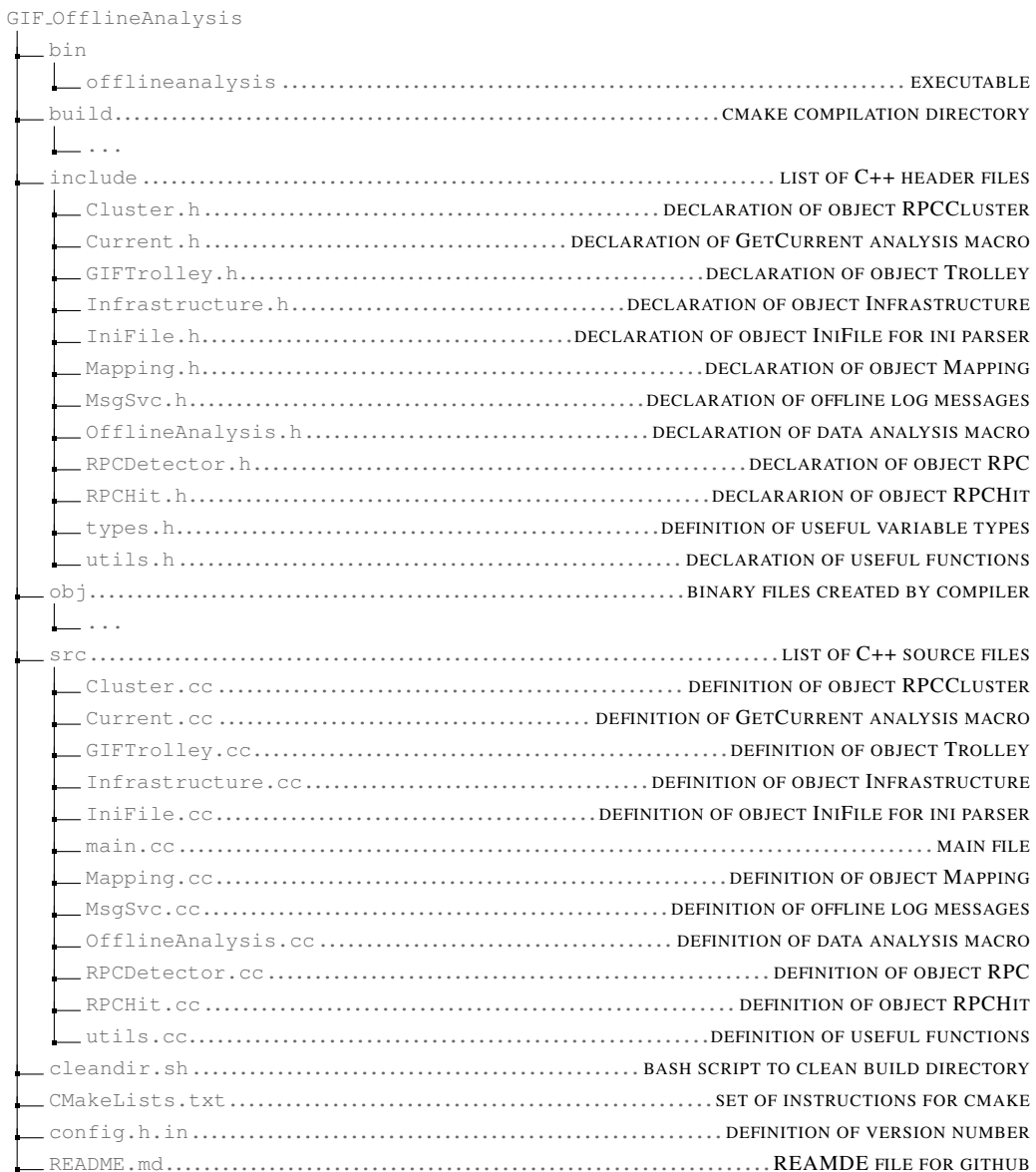
```
1645 mkdir build
1646 cd build
1647 cmake ..
1648 make
1649 make install
```

1647 To clean the directory and create a new build directory, the bash script cleandir.sh can be used:

```
1648
1649 ./cleandir.sh
```

1650 The source code tree is provided below along with comments to give an overview of the files' con-
1651 tent. The different objects created for this project (`Infrastructure`, `Trolley`, `RPC`, `Mapping`, `RPCHit`,
1652 `RPCCluster` and `Inifile`) will be described in details in the following sections.

1653



1654

B.2 Usage of the Offline Analysis

1655

In order to use the Offline Analysis tool, it is necessary to know the Scan number and the HV Step of the run that needs to be analysed. This information needs to be written in the following format:

1657

1658

```
Scan00XXXX_HVY
```

1659

where XXXX is the scan ID and Y is the high voltage step (in case of a high voltage scan, data will be taken for several HV steps). This format corresponds to the base name of data files in the database

1660

1661 of the GIF++ webDCS. Usually, the offline analysis tool is automatically called by the webDCS at
 1662 the end of data taking or by a user from the webDCS panel if an update of the tool was brought.
 1663 Nonetheless, an expert can locally launch the analysis for tests on the GIF++ computer, or a user can
 1664 get the code on its local machine from github and download data from the webDCS for its own anal-
 1665 ysis. To launch the code, the following command can be used from the `GIF_OfflineAnalysis` folder:

1666
 1667 `bin/offlineanalysis /path/to/Scan00XXXX_HVY`

1668 where, `/path/to/Scan00XXXX_HVY` refers to the local data files. Then, the offline tool will by itself
 1669 take care of finding all available ROOT data files present in the folder, as listed below:

- 1670
 - 1671 ● `Scan00XXXX_HVY_DAQ.root` containing the TDC data as described in Appendix ?? (events, hit
 and timestamp lists), and
 - 1672 ● `Scan00XXXX_HVY_CAEN.root` containing the CAEN mainframe data recorded by the monitor-
 ing tool webDCS during data taking (HVs and currents of every HV channels). This file is
 created independently of the DAQ.

1675 **B.2.1 Output of the offline tool**

1676 **B.2.1.1 ROOT file**

1677 The analysis gives in output ROOT datafiles that are saved into the data folder and called using the
 1678 naming convention `Scan00XXXX_HVY_Offline.root`. Inside those, a list of `TH1` histograms can be
 1679 found. Its size will vary as a function of the number of detectors in the setup as each set of histograms
 1680 is produced detector by detector. For each partition of each chamber, can be found:

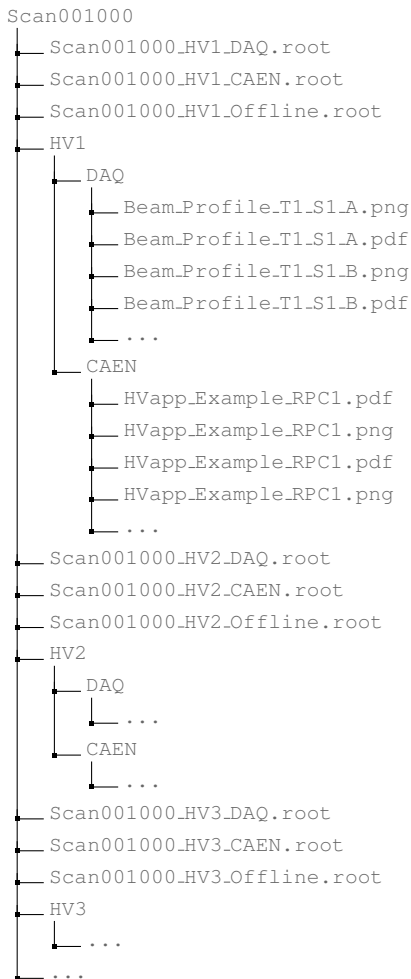
- 1681
 - 1682 ● `Time_Profile_Tt_Sc_p` shows the time profile of all recorded events (number of events per
 time bin),
 - 1683 ● `Hit_Profile_Tt_Sc_p` shows the hit profile of all recorded events (number of events per chan-
 nel),
 - 1685 ● `Hit_Multiplicity_Tt_Sc_p` shows the hit multiplicity (number of hits per event) of all recorded
 events (number of occurrences per multiplicity bin),
 - 1687 ● `Strip_Mean_Noise_Tt_Sc_p` shows noise/gamma rate per unit area for each strip in a se-
 lected time range. After filters are applied on `Time_Profile_Tt_Sc_p`, the filtered version
 of `Hit_Profile_Tt_Sc_p` is normalised to the total integrated time and active detection area
 of a single channel,
 - 1691 ● `Strip_Activity_Tt_Sc_p` shows noise/gamma activity for each strip (normalised version of
 previous histogram - strip activity = strip rate / average partition rate),
 - 1693 ● `Strip_Homogeneity_Tt_Sc_p` shows the *homogeneity* of a given partition ($\text{homogeneity} = \exp(-\text{strip rates standard deviation(strip rates in partition/average partition rate)})$),
 - 1695 ● `mask_Strip_Mean_Noise_Tt_Sc_p` shows noise/gamma rate per unit area for each masked
 strip in a selected time range. Offline, the user can control the noise/gamma rate and decide to
 mask the strips that are judged to be noisy or dead. This is done via the *Masking Tool* provided
 by the webDCS,

- 1699 ● `mask_Strip_Activity_Tt_Sc_p` shows noise/gamma activity per unit area for each masked
1700 strip with respect to the average rate of active strips,
- 1701 ● `NoiseCSize_H_Tt_Sc_p` shows noise/gamma cluster size, a cluster being constructed out of
1702 adjacent strips giving a signal at the *same time* (hits within a time window of 25 ns),
- 1703 ● `NoiseCMult_H_Tt_Sc_p` shows noise/gamma cluster multiplicity (number of reconstructed
1704 clusters per event),
- 1705 ● `Chip_Mean_Noise_Tt_Sc_p` shows the same information than `Strip_Mean_Noise_Tt_Scp` us-
1706 ing a different binning (1 chip corresponds to 8 strips),
- 1707 ● `Chip_Activity_Tt_Sc_p` shows the same information than `Strip_Activity_Tt_Scp` using
1708 chip binning,
- 1709 ● `Chip_Homogeneity_Tt_Sc_p` shows the homogeneity of a given partition using chip binning,
- 1710 ● `Beam_Profile_Tt_Sc_p` shows the estimated beam profile when taking efficiency scan. This
1711 is obtained by filtering `Time_Profile_Tt_Sc_p` to only consider the muon peak where the
1712 noise/gamma background has been subtracted. The resulting hit profile corresponds to the
1713 beam profile on the detector channels,
- 1714 ● `L0_Efficiency_Tt_Sc_p` shows the level 0 efficiency that was estimated **without** muon track-
1715 ing,
- 1716 ● `MuonCSize_H_Tt_Sc_p` shows the level 0 muon cluster size that was estimated **without** muon
1717 tracking, and
- 1718 ● `MuonCMult_H_Tt_Sc_p` shows the level 0 muon cluster multiplicity that was estimated **without**
1719 muon tracking.

1720 In the histogram labels, t stands for the trolley number (1 or 3), c for the chamber slot label in
1721 trolley t and p for the partition label (A, B, C or D depending on the chamber layout) as explained
1722 in Chapter ??.

1723 In the context of GIF++, an extra script called by the webDCS is called to extract the histograms
1724 from the ROOT files. The histograms are then stored in PNG and PDF formats into the correspond-
1725 ing folder (a single folder per HV step, so per ROOT file). the goal is to then display the histograms
1726 on the Data Quality Monitoring (DQM) page of the webDCS in order for the users to control the
1727 quality of the data taking at the end of data taking. An example of histogram organisation is given
1728 below:

1729
1730



1731 ***Here can put some screens from the webDCS to show the DQM and the plots available to users.***
 1732

1733 **B.2.1.2 CSV files**

1734 Moreover, up to 3 CSV files can be created depending on which ones of the 3 input files were in the
 1735 data folder:

- 1736 • `Offline-Corrupted.csv`, is used to keep track of the amount of data that was corrupted and
 1737 removed from old data format files that don't contain any data quality flag.
- 1738 • `Offline-Current.csv`, contains the summary of the currents and voltages applied on each
 1739 RPC HV channel.
- 1740 • `Offline-L0-EffC1.csv`, is used to write the efficiencies, cluster size and cluster multiplicity
 1741 of efficiency runs. Note that `L0` refers here to *Level 0* and means that the results of efficiency and
 1742 clusterization are a first approximation calculated without performing any muon tracking in

1743 between the different detectors. This offline tool provides the user with a preliminar calculation
 1744 of the efficiency and of the muon event parameters. Another analysis software especially
 1745 dedicated to muon tracking is called on selected data to retrieve the results of efficiency and
 1746 muon clusterization using a tracking algorithm to discriminate noise or gamma from muons
 1747 as muons are the only particles that pass through the full setup, leaving hits than can be used
 1748 to reconstruct their tracks.

- 1749 ● `Offline-Rate.csv`, is used to write the noise or gamma rates measured in the detector readout
 1750 partitions.

1751 Note that these 4 CSV files are created along with their *headers* (`Offline-[...]-Header.csv`
 1752 containing the names of each data columns) and are automatically merged together when the offline
 1753 analysis tool is called from the webDCS, contrary to the case where the tool is runned locally from
 1754 the terminal as the merging bash script is then not called. Thus, the resulting files, used to make
 1755 official plots, are:

- 1756 ● `Corrupted.csv`,
 1757 ● `Current.csv`,
 1758 ● `L0-EffCl.csv`.
 1759 ● `Rate.csv`.

1760 **B.3 Analysis inputs and information handling**

1761 The usage of the Offline Analysis tool as well as its output have been presented in the previous section.
 1762 It is now important to dig further and start looking at the source code and the inputs necessary
 1763 for the tool to work. Indeed, other than the raw ROOT data files that are analysed, more information
 1764 needs to be imported inside of the program to perform the analysis such as the description of the
 1765 setup inside of GIFT++ at the time of data taking (number of trolleys, of RPCs, dimensions of the
 1766 detectors, etc...) or the mapping that links the TDC channels to the coresponding RPC channels in
 1767 order to translate the TDC information into human readable data. 2 files are used to transmit all this
 1768 information:
 1769

- 1770 ● `Dimensions.ini`, that provides the necessary setup and RPC information, and
 1771 ● `ChannelsMapping.csv`, that gives the link between the TDC and RPC channels as well as the
 1772 *mask* for each channel (masked or not?).

1773 **B.3.1 Dimensions file and InFile parser**

1774 This input file, present in every data folder, allows the analysis tool to know of the number of active
 1775 trolleys, the number of active RPCs in those trolleys, and the details about each RPCs such as
 1776 the number of RPC gaps, the number of pseudo-rapidity partitions (for CMS-like prototypes), the
 1777 number of strips per partion or the dimensions. To do so, there are 3 types of groups in the INI file
 1778 architecture. A first general group, appearing only once at the head of the document, gives information
 1779 about the number of active trolleys as well as their IDs, as presented in Source Code B.1. For

1780 each active trolley, a group similar to Source Code B.2 can be found containing information about
 1781 the number of active detectors in the trolley and their IDs. Each trolley group as a `Tt` name format,
 1782 where `t` is the trolley ID. Finally, for each detector stored in slots of an active trolley, there is a group
 1783 providing information about their names and dimensions, as shown in Source Code B.3. Each slot
 1784 group as a `TtSs` name format, where `s` is the slot ID of trolley `t` where the active RPC is hosted.

```
1785 [General]
1786 nTrolleys=2
  TrolleysID=13
```

1787 *Source Code B.1: Example of `[General]` group as might be found in `Dimensions.ini`. In Gif++, only 2
 trolleys are available to hold RPCs and place them inside of the bunker for irradiation. The IDs of the trolleys
 are written in a single string as "13" and then read character by character by the program.*

```
1788 [T1]
  nSlots=4
  SlotsID=1234
```

1789 *Source Code B.2: Example of trolley group as might be found in `Dimensions.ini`. In this example, the file
 tells that there are 4 detectors placed in the holding slots of the trolley `T1` and that their IDs, written as a single
 string variable, are 1, 2, 3 and 4.*

```
1790 [T1S1]
  Name=RE2-2-NPD-BARC-8
  Partitions=3
  Gaps=3
  Gap1=BOT
  Gap2=TN
  Gap3=TW
  AreaGap1=11694.25
  AreaGap2=6432
  AreaGap3=4582.82
  Strips=32
  ActiveArea-A=157.8
  ActiveArea-B=121.69
  ActiveArea-C=93.03
```

1791 *Source Code B.3: Example of slot group as might be found in `Dimensions.ini`. In this example, the file
 provides information about a detector named `RE2-2-NPD-BARC-8`, having 3 pseudo-rapidity readout partitions
 and stored in slot `S1` of trolley `T1`. This is a CMS RE2-2 type of detector. This information will then be used for
 example to compute the rate per unit area calculation.*

1792 This information is readout and stored in a C++ object called `IniFile`, that parses the information
 1793 in the INI input file and stores it into a local buffer for later use. This INI parser is the exact same
 1794 one that was previously developed for the Gif++ DAQ and described in Appendix A.5.2.

1795 B.3.2 TDC to RPC link file and Mapping

1796 The same way the INI dimension file information is stored using `map`, the channel mapping and mask
 1797 information is stored and accessed through `map`. First of all, the mapping CSV file is organised into
 1798 3 columns separated by tabulations (and not by commas, as expected for CSV files as it is easier using
 1799 streams to read tab or space separated data using C++):

1800

1801 `RPC_channel` `TDC_channel` `mask`

1802 using as formatting for each field:

1803

1804 `TSCCC` `TCCC` `M`

1805 `TSCCC` is a 5-digit integer where `T` is the trolley ID, `s` the slot ID in which the RPC is held insite
 1806 the trolley `T` and `ccc` is the RPC channel number, or *strip* number, that can take values up to
 1807 3-digits depending on the detector,

1808 `TCCC` is a 4 digit integer where `T` is the TDC ID, `ccc` is the TDC channel number that can take values
 1809 in between 0 and 127, and

1810 `M` is a 1-digit integer indicating if the channel should be considered (`M = 1`) or discarded (`M = 0`)
 1811 during analysis.

1812 This mapping and masking information is readout and stored thanks to the object `Mapping`, pre-
 1813 sented in Source Code B.4. Similarly to `IniFile` objects, this class has private methods. The first
 1814 one, `Mapping::CheckIfNewLine()` is used to find the newline character '`\n`' or return character
 1815 '`\r`' (depending on which kind of operating system interacted with the file). This is used for the
 1816 simple reason that the masking information has been introduced only during the year 2017 but the
 1817 channel mapping files exist since 2015 and the very beginning of data taking at GIF++. This means
 1818 that in the older data folders, before the upgrade, the channel mapping file only had 2 columns, the
 1819 RPC channel and the TDC channel. For compatibility reasons, this method helps controling the
 1820 character following the readout of the 2 first fields of a line. In case any end of line character is
 1821 found, no mask information is present in the file and the default `M = 1` is used. On the contrary, if
 1822 the next character was a tabulation or a space, the mask information is present.

1823 Once the 3 fields have been readout, the second private method `Mapping::CheckIfTDCCh()` is
 1824 used to control that the TDC channel is an existing TDC channel. Finally, the information is stored
 1825 into 3 different maps (`Link`, `ReverseLink` and `Mask`) thanks to the public method `Mapping::Read()`.
 1826 `Link` allows to get the RPC channel by knowing the TDC channel while `ReverseLink` does the op-
 1827 posite by returning the TDC channel by knowing the RPC channel. Finally, `Mask` returns the mask
 1828 associated to a given RPC channel.

```

1829 typedef map<Uint,Uint> MappingData;

1830 class Mapping {
    private:
        bool          CheckIfNewLine(char next);
        bool          CheckIfTDCCh(Uint channel);
        string         FileName;
        MappingData   Link;
        MappingData   ReverseLink;
        MappingData   Mask;
        int           Error;

1831     public:
        Mapping();
        Mapping(string baseName);
        ~Mapping();

        void SetFileName(const string filename);
        int Read();
        Uint GetLink(Uint tdcchannel);
        Uint GetReverse(Uint rpcchannel);
        Uint GetMask(Uint rpcchannel);
    };

```

1831 *Source Code B.4: Description of C++ object Mapping used as a parser for the channel mapping and mask file.*

1832 **B.4 Description of GIF++ setup within the Offline Analysis tool**

1833 In the previous section, the tool input files have been discussed. The dimension file information is
 1834 stored in a map hosted by the `IniFile` object. But this information is then used to create a series of
 1835 new objects that helps defining the GIF++ infrastructure directly into the Offline Analysis. Indeed,
 1836 from the `RPC`, to the more general `Infrastructure`, every element of the GIF++ infrastrucutre is
 1837 recreated for each data analysis based on the information provided in input. All this information
 1838 about the infrastructure will be used to assign each hit signal to a specific strip channel of a specific
 1839 detector, and having a specific active area. This way, rate per unit area calculation is possible.

1840

1841 **B.4.1 RPC objects**

1842 `RPC` objects have been developped to represent physical active detectors in GIF++ at the moment
 1843 of data taking. Thus, there are as many `RPC` objects created during the analysis than there were
 1844 active `RPC`s tested during a run. Each `RPC` hosts the information present in the corresponding INI
 1845 slot group, as shown in B.3, and organises it using a similar architecture. This can be seen from
 1846 Source Code B.5.

1847 To make the object more compact, the lists of gap labels, of gap active areas and strip active
 1848 areas are stored into `vector` dynamical containers. `RPC` objects are always contructed thanks to the
 1849 dimension file information stored into the `IniFILE` and their ID, using the format `TtSs`. Using the
 1850 `RPC` ID, the constructor calls the methods of `IniFILE` to initialise the `RPC`. The other constructors
 1851 are not used but exist in case of need. Finally, some getters have been written to access the different
 1852 private parameters storing the detector information.

```

1853 class RPC{
1854     private:
1855         string      name;           //RPC name as in webDCS database
1856         Uint        nGaps;          //Number of gaps in the RPC
1857         Uint        nPartitions;    //Number of partitions in the RPC
1858         Uint        nStrips;        //Number of strips per partition
1859         vector<string> gaps;       //List of gap labels (BOT, TOP, etc...)
1860         vector<float>  gapGeo;        //List of gap active areas
1861         vector<float>  stripGeo;      //List of strip active areas
1862
1863     public:
1864         RPC();
1865         RPC(string ID, IniFile* geofile);
1866         RPC(const RPC& other);
1867         ~RPC();
1868         RPC& operator=(const RPC& other);
1869
1870         string GetName();
1871         Uint GetNGaps();
1872         Uint GetNPartitions();
1873         Uint GetNStrips();
1874         string GetGap(Uint g);
1875         float GetGapGeo(Uint g);
1876         float GetStripGeo(Uint p);
1877     };

```

1855 *Source Code B.5: Description of C++ objects RPC that describe each active detectors used during data taking.*

1856 B.4.2 Trolley objects

1857 Trolley objects have been developped to represent physical active trolleys in GIFT++ at the moment
 1858 of data taking. Thus, there are as many trolley objects created during the analysis than there were
 1859 active trolleys hosting tested RPCs during a run. Each Trolley hosts the information present in the
 1860 corresponding INI trolley group, as shown in B.2, and organises it using a similar architecture. In
 1861 addition to the information hosted in the INI file, these object have a dynamical container of RPC
 1862 objects, representing the active detectors the active trolley was hosting at the time of data taking.
 1863 This can been seen from Source Code B.6.

1864 Trolley objects are always contructed thanks to the dimension file information stored into the
 1865 IniFILE and their ID, using the format Tt. Using the Trolley ID, the constructor calls the methods
 1866 of IniFILE to initialise the Trolley. Retrieving the information of the RPC IDs via SlotsID, a new
 1867 RPC is constructed and added to the container RPCs for each character in the ID string. The other
 1868 constructors are not used but exist in case of need. Finally, some getters have been written to access
 1869 the different private parameters storing the trolley and detectors information.

```

1870
class Trolley{
    private:
        Uint          nSlots; //Number of active RPCs in the considered trolley
        string        SlotsID; //Active RPC IDs written into a string
        vector<RPC*> RPCs;   //List of active RPCs

    public:
        //Constructors, destructor and operator =
        Trolley();
        Trolley(string ID, IniFile* geofile);
        Trolley(const Trolley& other);
        ~Trolley();
        Trolley& operator=(const Trolley& other);

        //Get GIFTrolley members
        Uint  GetNSlots();
        string GetSlotsID();
        Uint   GetSlotID(Uint s);

        //Manage RPC list
        RPC*  GetRPC(Uint r);
        void  DeleteRPC(Uint r);

        //Methods to get members of RPC objects stored in RPCs
        string GetName(Uint r);
        Uint   GetNGaps(Uint r);
        Uint   GetNPartitions(Uint r);
        Uint   GetNStrips(Uint r);
        string GetGap(Uint r, Uint g);
        float  GetGapGeo(Uint r, Uint g);
        float  GetStripGeo(Uint r, Uint p);
    };

```

Source Code B.6: Description of C++ objects `Trolley` that describe each active trolley used during data taking.

1873 B.4.3 Infrastructure object

1874 The `Infrastructure` object has been developped to represent the GIFT++ bunker area dedicated to
 1875 CMS RPC experiments. With this very specific object, all the information about the CMS RPC
 1876 setup within GIFT++ at the moment of data taking is stored. It hosts the information present in the
 1877 corresponding INI general group, as shown in B.1, and organises it using a similar architecture. In
 1878 addition to the information hosted in the INI file, this object have a dynamical container of `Trolley`
 1879 objects, representing the active tolleys in GIFT++ area. This can be seen from Source Code B.7.

1880 The `Infrastructure` object is always contructed thanks to the dimension file information stored
 1881 into the `IniFILE`. Retrieving the information of the trolley IDs via `TrolleysID`, a new `Trolley` is
 1882 constructed and added to the container `Trolleys` for each character in the ID `string`. By extension,
 1883 it is easy to understand that the process described in Section B.4.2 for the construction of RPCs
 1884 takes place when a trolley is constructed. The other constructors are not used but exist in case of
 1885 need. Finally, some getters have been written to access the different private parameters storing the
 1886 infrastructure, tolleys and detectors information.

```

1887
class Infrastructure {
    private:
        Uint             nTrolleys;   //Number of active Trolleys in the run
        string          TrolleysID;  //Active trolley IDs written into a string
        vector<Trolley*> Trolleys;  //List of active Trolleys (struct)

    public:
        //Constructors and destructor
        Infrastructure();
        Infrastructure(IniFile* geofile);
        Infrastructure(const Infrastructure& other);
        ~Infrastructure();
        Infrastructure& operator=(const Infrastructure& other);

        //Get Infrastructure members
        Uint  GetNTrolleys();
        string GetTrolleysID();
        Uint   GetTrolleyID(Uint t);

1888
        //Manage Trolleys
        Trolley* GetTrolley(Uint t);
        void     DeleteTrolley(Uint t);

        //Methods to get members of GIFTrolley objects stored in Trolleys
        Uint  GetNSlots(Uint t);
        string GetSlotsID(Uint t);
        Uint   GetSlotID(Uint t, Uint s);
        RPC*  GetRPC(Uint t, Uint r);

        //Methods to get members of RPC objects stored in RPCs
        string GetName(Uint t, Uint r);
        Uint   GetNGaps(Uint t, Uint r);
        Uint   GetNPartitions(Uint t, Uint r);
        Uint   GetNStrips(Uint t, Uint r);
        string GetGap(Uint t, Uint r, Uint g);
        float  GetGapGeo(Uint t, Uint r, Uint g);
        float  GetStripGeo(Uint t, Uint r, Uint p);
};


```

Source Code B.7: Description of C++ object Infrastructure that contains the full information about CMS RPC experiment in GIF++.

1890 B.5 Handeling of data

1891 As discussed in Appendix A.4.2, the raw data as a `TTree` architecture where every entry is related to
 1892 a trigger signal provided by a muon or a random pulse, whether the goal of the data taking was to
 1893 measure the performance of the detector or the noise/gamma background respectively. Each of these
 1894 entries, referred also as events, contain a more or less full list of hits in the TDC channels to which
 1895 the detectors are connected. To this list of hits corresponds a list of time stamps, marking the arrival
 1896 of the hits within the TDC channel.

1897 The infrastructure of the CMS RPC experiment within `GIF++` being defined, combining the
 1898 information about the raw data with the information provided by both the mapping/mask file and the
 1899 dimension file allows to build new physical objects that will help in computing efficiency or rates.

1900 B.5.1 RPC hits

1901 The raw data stored in the ROOT file as output of the GIFT++ DAQ, is readout by the analysis tool
 1902 using the structure `RAWData` presented in Source Code B.9 that differs from the structure presented
 1903 in Appendix A.4.2 as it is not meant to hold all of the data contained in the ROOT file. In this sense,
 1904 this structure is in the case of the offline analysis tool not a dynamical object and will only be storing
 1905 a single event contained in a single entry of the `TTree`.

```
1906
1907 class RPCHit {
1908     private:
1909         Uint Channel;      //RPC channel according to mapping (5 digits)
1910         Uint Trolley;      //0, 1 or 3 (1st digit of the RPC channel)
1911         Uint Station;      //Slot where is held the RPC in Trolley (2nd digit)
1912         Uint Strip;        //Physical RPC strip where the hit occurred (last 3
1913             digits)
1914         Uint Partition;    //Readout partition along eta segmentation
1915         float TimeStamp;   //Time stamp of the arrival in TDC
1916
1917     public:
1918         //Constructors, destructor & operator =
1919         RPCHit();
1920         RPCHit(Uint channel, float time, Infrastructure* Infra);
1921         RPCHit(const RPCHit& other);
1922         ~RPCHit();
1923         RPCHit& operator=(const RPCHit& other);
1924
1925         //Get RPCHit members
1926         Uint GetChannel();
1927         Uint GetTrolley();
1928         Uint GetStation();
1929         Uint GetStrip();
1930         Uint GetPartition();
1931         float GetTime();
1932     };
1933
1934     typedef vector<RPCHit> HitList;
1935     typedef struct GIFHitList { HitList rpc[NTROLLEYS][NSLOTS][NPARTITIONS]; } →
1936             GIFHitList;
1937
1938     bool SortHitbyStrip(RPCHit h1, RPCHit h2);
1939     bool SortHitbyTime(RPCHit h1, RPCHit h2);
1940 }
```

1908 *Source Code B.8: Description of C++ object RPCHit.*

```
1941
1942     struct RAWData{
1943         int iEvent;          //Event i
1944         int TDCNHits;       //Number of hits in event i
1945         int QFlag;           //Quality flag list (1 flag digit per TDC)
1946         vector<Uint> *TDCCh; //List of channels giving hits per event
1947         vector<float> *TDCTS; //List of the corresponding time stamps
1948     };
1949 }
```

1910 *Source Code B.9: Description of C++ structure RAWData.*

1911 Each member of the structure is then linked to the corresponding branch of the ROOT data tree,
 1912 as shown in the example of Source Code B.10, and using the method `GetEntry(int i)` of the ROOT
 1913 class `TTree` will update the state of the members of `RAWData`.

```

1914 TTree* dataTree = (TTree*)dataFile.Get("RAWData");
1915 RAWData data;
1916
1917 dataTree->SetBranchAddress("EventNumber", &data.iEvent);
1918 dataTree->SetBranchAddress("number_of_hits", &data.TDCNHits);
1919 dataTree->SetBranchAddress("Quality_flag", &data.QFlag);
1920 dataTree->SetBranchAddress("TDC_channel", &data.TDCCh);
1921 dataTree->SetBranchAddress("TDC_TimeStamp", &data.TDCTS);

```

1916 *Source Code B.10: Example of link in between RAWData and TTree.*

1917 The data is then analysed entry by entry and to each element of the TDC channel list, a `RPCHit` is
 1918 constructed by linking each TDC channel to the corresponding RPC channel thanks to the `Mapping`
 1919 object. The information carried by the RPC channel format allows to easily retrieve the trolley and
 1920 slot from which the hit was recorded (see section B.3.2). Using these 2 values, the readout partition
 1921 can be found by knowing the strip channel and comparing it with the number of partitions and strips
 1922 per partition stored into the `Infrastructure` object.

1923 Thus `RPCHit` objects are then stored into 3D dynamical list called `GIFHitList` (Source Code B.9)
 1924 where the 3 dimensions refer to the 3 layers of the readout in `GIF++` : in the bunker there are *trolleys*
 1925 (τ) holding detectors in *slots* (s) and each detector readout is divided into 1 or more pseudo-rapidity
 1926 *partitions* (p). Using these 3 information allows to assign an address to each readout partition and
 1927 this address will point to a specific hit list.

1928

1929 B.5.2 Clusters of hits

1930 All the hits contained in the ROOT file have been sorted into the different hit lists through the
 1931 `GIFHitList`. At this point, it is possible to start looking for clusters. A cluster is a group of adjacent
 1932 strips getting hits within a time window of 25 ns. These strips are then assumed to be part of the same
 1933 physical avalanche signal generated by a muon passing through the chamber or by the interaction of
 1934 a gamma stopping into the electrodes of the RPCs.

1935 To keep the cluster information, `RPCCluster` objects have been defined as shown in Source
 1936 Code B.11. Using the information of each individual `RPCHit` taken out of the hit list, it stores
 1937 the cluster size (number of adjacent strips composing the cluster), the first and last hit, the center for
 1938 spatial reconstruction and finally the start and stop time stamps as well as te time spread in between
 1939 the first and last hit.

```

1940
class RPCCluster{
    private:
        Uint ClusterSize; //Size of cluster #ID
        Uint FirstStrip; //First strip of cluster #ID
        Uint LastStrip; //Last strip of cluster #ID
        float Center; //Center of cluster #ID ((first+last)/2)
        float StartStamp; //Time stamp of the earliest hit of cluster #ID
        float StopStamp; //Time stamp of the latest hit of cluster #ID
        float TimeSpread; //Time difference between earliest and latest hits
                           //of cluster #ID

    public:
        //Constructors, destructor & operator =
        RPCCluster();
        RPCCluster(HitList List, Uint cID, Uint cSize, Uint first, Uint firstID);
        RPCCluster(const RPCCluster& other);
        ~RPCCluster();
        RPCCluster& operator=(const RPCCluster& other);

        //Get Cluster members
        Uint GetID();
        Uint GetSize();
        Uint GetFirstStrip();
        Uint GetLastStrip();
        float GetCenter();
        float GetStart();
        float GetStop();
        float GetSpread();
};

typedef vector<RPCCluster> ClusterList;

//Other functions to build cluster lists out of hit lists
void BuildClusters(HitList &cluster, ClusterList &clusterList);
void Clusterization(HitList &hits, TH1 *hcSize, TH1 *hcMult);

```

Source Code B.11: Description of C++ object Cluster.

To investigate the hit list of a given detector partition, the function `Clusterization()` defined in `include/Cluster.h` needs the hits in the list to be time sorted. This is achieved by calling function `sort()` of library `<algorithm>` using the comparator `SortHitbyTime(RPCHit h1, RPCHit h2)` defined in `include/RPCHit.h` that returns `true` if the time stamp of hit `h1` is lower than that of `h2`. A first isolation of strips is made only based on time information. All the hits within the 25 ns window are taken separately from the rest. Then, this sub-list of hits is sorted this time by ascending strip number, using this time the comparator `SortHitbyStrip(RPCHit h1, RPCHit h2)`. Finally, the groups of adjacent strips are used to construct `RPCCluster` objects that are then stored in a temporary list of clusters that is at the end of the process used to know how many clusters were reconstructed and to fill their sizes into an histogram that will allows to know the mean size of muon or gamma clusters.

1955 B.6 DAQ data Analysis

All the ingredients to analyse GIF++ data have been defined. This section will focus on the different part of the analysis performed on the data, from determining the type of data the tool is dealing with

1958 to calculating the rate in each detector or reconstructing muon or gamma clusters.

1959 B.6.1 Determination of the run type

1960 In GIF++, both the performance of the detectors in detecting muons in an irradiated environment and
 1961 the gamma background can be independantly measured. These corresponds to different run types
 1962 and thus, to different TDC settings giving different data to look at.

1963

1964 In the case of performance measurements, the trigger for data taking is provided by the coïncidence
 1965 of several scintillators when muons from the beam passing through the area are detected. Data
 1966 is collected in a 600 ns wide window around the arrival of muons in the RPCs. The expected time
 1967 distribution of hits is shown in Figure B.1a. The muon peak is clearly visible in the center of the
 1968 distribution and is to be extracted from the gamma background that composes the flat part of the
 1969 distribution.

1970 On the other hand, gamma background or noise measurements are focussed on the non muon
 1971 related physics and the trigger needs to be independant from the muons to give a good measurement
 1972 of the gamma/noise distribution as seen by the detectors. The trigger is then provided by a pulse
 1973 generator at a frequency of 300 Hz whose pulse is not likely to be on time with a muon. In order
 1974 to increase the integrated time without increasing the acquisition time too much, the width of the
 1975 acquisition windows are increased to 10 μ s. The time distribution of the hits is expected to be flat, as
 1976 shown by Figure B.1b.

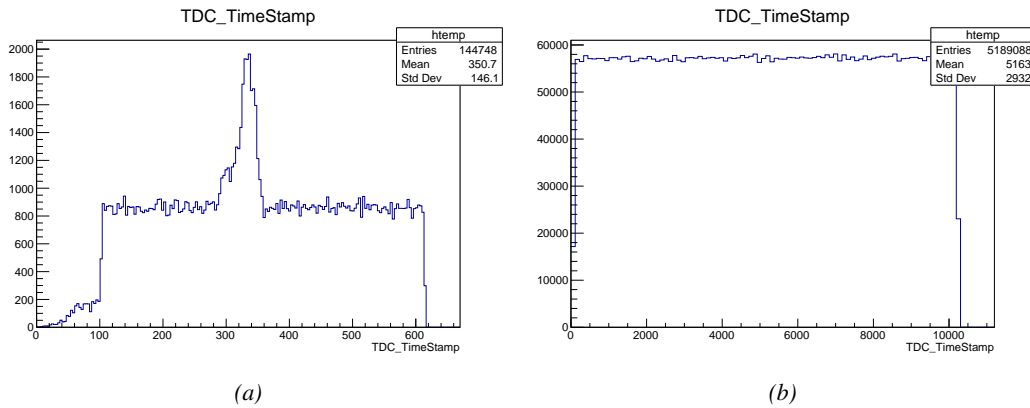


Figure B.1: Example of expected hit time distributions in the cases of efficiency (Figure B.1a) and noise/gamma rate per unit area (Figure B.1b) measurements as extracted from the raw ROOT files. The unit along the x-axis corresponds to ns. The fact that "the" muon peak is not well defined in Figure B.1a is due to the contribution of all the RPCs being tested at the same time that don't necessarily have the same signal arrival time. Each individual peak can have an offset with the ones of other detectors. The inconsistency in the first 100 ns of both time distributions is an artefact of the TDCs and are systematically rejected during the analysis.

1977 The ROOT files include a TTree called RunParameters containing, among other things, the in-
 1978 formation related to the type of run. The run type can then be accessed as described by Source
 1979 Code B.12 and the function IsEfficiencyRun() is then used to determine if the run file is an effi-
 1980 ciency run or, on the contrary, another type of run (noise or gamma measurement).

```

1981     TTree* RunParameters = (TTree*)dataFile.Get("RunParameters");
1982     TString* RunType = new TString();
1983     RunParameters->SetBranchAddress("RunType", &RunType);
1984     RunParameters->GetEntry(0);

```

1983 *Source Code B.12: Access to the run type contained in TTree* RunParameters.*

1984 Finally, the data files will have a slightly different content whether it was collected before or after
 1985 October 2017 and the upgrade of the DAQ software that brought a new information into the ROOT
 1986 output. This is discussed in Appendix A.4.3 and implies that the analysis will differ a little depending
 1987 on the data format. Indeed, as no information on the data quality is stored, in older data files, the cor-
 1988 rections for missing events has to be done at the end of the analysis. The information about the type
 1989 of data format is stored in the variable **bool** `isNewFormat` by checking the list of branches contained
 1990 in the data tree via the methods `TTree::GetListOfBranches()` and `TCollection::Contains()`.

1991 **B.6.2 Beam time window calculation for efficiency runs**

1992 Knowing the run type is important first of all to know the width of the acquisition window to be used
 1993 for the rate calculation and finally to be able to seek for muons. Indeed, the peak that appears in the
 1994 time distribution for each detectors is then fitted to extract the most probable time window in which
 1995 the tool should look for muon hits. The data outside of this time window is then used to evaluate the
 1996 noise or gamma background the detector was subjected to during the data taking. Computing the
 1997 position of the peak is done calling the function `SetBeamWindow()` defined in file `src/RPCHit.cc` that
 1998 loops a first time on the data. The data is first sorted in a 3D array of 1D histograms (`GIFH1Array`, see
 1999 `include/types.h`). Then the location of the highest bin is determined using `TH1::GetMaximumBin()`
 2000 and is used to define a window in which a gaussian fit will be applied to compute the peak width.
 2001 This window is a 80 ns defined by Formula B.1 around the central bin.

$$t_{center}(ns) = bin \times width_{bin}(ns) \quad (\text{B.1a})$$

$$[t_{low}; t_{high}] = [t_{center} - 40; t_{center} + 40] \quad (\text{B.1b})$$

2002 Before the fit is performed, the average number of noise/gamma hits per bin is evaluated using
 2003 the data outside of the fit window. Excluding the first 100 ns, the average number of hits per bin
 2004 due to the noise or gamma is defined by Formula B.2 after extracting the amount of hits in the time
 2005 windows $[100; t_{low}]$ and $[t_{high}; 600]$ thanks to the method `TH1::Integral()`. This average number
 2006 of hits is then subtracted to every bin of the 1D histogram, in order to *clean* it from the noise or
 2007 gamma contribution as much as possible to improve the fit quality. Bins where $\langle n_{hits} \rangle$ is greater
 2008 than the actual bin content are set to 0.

$$\Delta t_{noise}(ns) = 600 \overbrace{-t_{high} + t_{low}}^{-80ns} - 100 = 420ns \quad (\text{B.2a})$$

$$\langle n_{hits} \rangle = width_{bin}(ns) \times \frac{\sum_{t=100}^{t_{low}} + \sum_{t=t_{high}}^{600}}{\Delta t_{noise}(ns)} \quad (\text{B.2b})$$

2009 Finally, the fit parameters are extracted and saved for each detector in 3D arrays of **float**
 2010 (`muonPeak`, see `include/types.h`), a first one for the mean arrival time of the muons, `PeakTime`,

2011 and a second one for the width of the peak, `PeakWidth`. The width is defined as 6σ of the gaussian
 2012 fit. The same settings are applied to every partitions of the same detector. To determine which one
 2013 of the detector's partitions is directly illuminated by the beam, the peak height of each partition is
 2014 compared and the highest one is then used to define the peak settings.

2015 **B.6.3 Data loop and histogram filling**

2016 3D arrays of histogram are created to store the data and display it on the DQM of G4F++ webDCS
 2017 for the use of shifters. These histograms, presented in section B.2.1.1, are filled while looping on
 2018 the data. Before starting the analysis loop, it is necessary to control the entry quality for the new
 2019 file formats featuring `QFlag`. If the `QFlag` value for this entry shows that 1 TDC or more have a
 2020 `CORRUPTED` flag, then this event is discarded. The loss of statistics is low enough to be neglected.
 2021 `QFlag` is controlled using the function `IsCorruptedEvent()` defined in `src/utils.cc`. As explained
 2022 in Appendix A.4.3, each digit of this integer represents a TDC flag that can be 1 or 2. Each 2 is
 2023 the sign of a `CORRUPTED` state. Then, the data is accessed entry by entry in the ROOT `TTree` using
 2024 `RAWData` and each hit in the hit list is assigned to a detector channel and saved in the corresponding
 2025 histograms. In the first part of the analysis, in which the loop over the ROOT file's content is
 2026 performed, the different steps are:

2027 **1- RPC channel assignment and control:** a check is done on the RPC channel extracted thanks
 2028 to the mapping via the method `Mapping::GetLink()`. If the channel is not initialised and is 0, or if
 2029 the TDC channel was greater than 5127, the hit is discarded. This means there was a problem in the
 2030 mapping. Often a mapping problem leads to the crash of the offline tool.

2031 **2- Creation of a `RPCHit` object:** to easily get the trolley, slot and partition in which the hit has
 2032 been assigned, this object is particularly helpful.

2033 **3- General histograms are filled:** the hit is filled into the time distribution and the general hit
 2034 distribution histograms, and if the arrival time is within the first 100 ns, it is discarded and nothing
 2035 else happens and the loop proceeds with the next hit in the list.

2036 **4- Multiplicity counter:** the hit multiplicity counter of the corresponding detectors incremented.

2037 **5-a- Efficiency runs - Is the hit within the peak window? :** if the peak is contained in the peak
 2038 window previously defined in section B.6.2, the hit is filled into the beam hit profile histogram of
 2039 the corresponding chamber, added into the list of muon hits and increments the counter of *in time*
 2040 hits. The term *in time* here refers to the hits that are likely to be muons by arriving in the expected
 2041 time window. If the hit is outside of the peak window, it is filled into the noise profile histogram
 2042 of the corresponding detector, added into the list of noise/gamma hits and increments the counter of
 2043 noise/gamma hits.

2044 **5-b- Noise/gamma rate runs - Noise histograms are filled:** the hit is filled into the noise profile
 2045 histogram of the corresponding detector, added into the list of noise/gamma hits and increments the
 2046 counter of noise/gamma hits.

2047

2048 After the loop on the hit list of the entry is over, the next step is to clusterize the 3D lists filled
 2049 in the previous steps. A 3D loop is then started over the active trolley, slot and RPC partitions to
 2050 access these objects. Each `NoiseHitList` and `MuonHitList`, in case of efficiency run, are clusterized
 2051 as described in section B.5.2. There corresponding cluster size and multiplicity histograms are filled
 2052 at the end of the clustering process. Then, the efficiency histogram is filled in case of efficiency run.
 2053 The selection is simply made by checking whether the RPC detected signals in the peak window
 2054 during this event. Nevertheless, it is useful to highlight that at this level, it is not possible yet to
 2055 discriminate in between a muon hit and noise or gamma hit. Thus, `MuonCSize_H`, `MuonCMult_H`
 2056 and `Efficiency0_H` are subjected to noise and gamma contamination. This contamination will be
 2057 estimated and corrected at the moment the results will be written into output CSV files. Finally, the
 2058 loop ends on the filling of the general hit multiplicity histogram.

2059 **B.6.4 Results calculation**

2060 As mentioned in section B.2.1, the analysis of DAQ data provides the user with 3 CSV files and
 2061 a ROOT file associated to each and every ROOT data file. The fourth CSV file is provided by the
 2062 extraction of the CEAN main frame data monitored during data taking and will be discussed later.
 2063 After looping on the data in the previous part of the analysis macro, the output files are created and a
 2064 3D loop on each RPC readout partitions is started to extract the histograms parameters and compute
 2065 the final results.

2066

2067 **B.6.4.1 Rate normalisation**

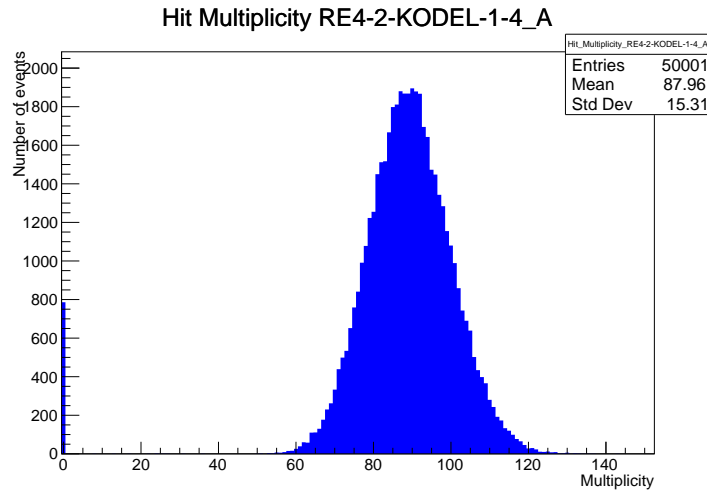


Figure B.2: The effect of the quality flag is explained by presenting the reconstructed hit multiplicity of a data file without `Quality_flag`. The artificial high content of bin 0 is the effect of corrupted data.

2068 To analyse old data format files, not containing any quality flag, it is needed to estimate the amount
 2069 of corrupted data via a fit as the corrupted data will always fill events with a fake "0 multiplicity".
 2070 Indeed, as no hits were stored in the DAQ ROOT files, these events artificially contribute to fill
 2071 the bin corresponding to a null multiplicity, as shown in Figure B.2. In the case the mean of the

hit multiplicity distribution is high, the contribution of the corrupted data can easily be evaluated for later correction by comparing the level of the bin at multiplicity 0 and of a skew fit curve that should indicate a value consistent with 0. A skew fit has been chosen over a Poisson fit as it was giving better results for lower mean multiplicity values. Nevertheless, for low irradiation cases, as explained in Appendix A.4.3, the hit multiplicity distribution mean is, on the contrary, rather small and the probability to record events without hits can't be considered small anymore, leading to a difficult and non-reliable estimation of the corruption. As can be seen in Source Code B.13, conditions have been applied to prevent bad fits and wrong corruption estimation in cases where :

- The difference in between the data for multiplicity 1 and the corresponding fit value should be lower than 1% of the total amount of data : $\frac{|n_{m=1} - sk(1)|}{N_{tot}} < 0.01$ where $n_{m=1}$ is the number of entries with multiplicity 1, $sk(1)$ the value of the skew fit, as defined by Formula 4.3, for multiplicity 1 and N_{tot} the total number of entries.

- The amount of data contained in the multiplicity 0 bin should not exceed 40% : $\frac{n_{m=0}}{N_{tot}} \leq 0.4$ where $n_{m=0}$ is the number of entries with multiplicity 0. This number has been determined to be the maximum to be able to separate the excess of data due to corruption from the hit multiplicity distribution.

Those 2 conditions need to be fulfilled to estimate the corruption of old data format files. If the fit was successful, the level of corruption is written in `Offline-Corrupted.csv` and the number of corrupted entries, refered as the integer `nEmptyEvent`, is subtracted from the total number of entries when the rate normalisation factor is computed as explicit in Source Code B.13. Note that for new data format files, the number of corrupted entries being set to 0, the definition of `rate_norm` stays valid.

```

2094
if(!isNewFormat){
    TF1* GaussFit = new TF1("gaussfit","[0]*exp(-0.5*((x-[1])/[2])**2)",0,Xmax);
    GaussFit->SetParameter(0,100);
    GaussFit->SetParameter(1,10);
    GaussFit->SetParameter(2,1);
    HitMultiplicity_H.rpc[T][S][p]->Fit(GaussFit,"LIQR","",0.5,Xmax);

    TF1* SkewFit = new TF1("skewfit","[0]*exp(-0.5*((x-[1])/[2])**2) / (1 +
→ exp(-[3]*(x-[4])))",0,Xmax);
    SkewFit->SetParameter(0,GaussFit->GetParameter(0));
    SkewFit->SetParameter(1,GaussFit->GetParameter(1));
    SkewFit->SetParameter(2,GaussFit->GetParameter(2));
    SkewFit->SetParameter(3,1);
    SkewFit->SetParameter(4,1);
    HitMultiplicity_H.rpc[T][S][p]->Fit(SkewFit,"LIQR","",0.5,Xmax);

    double fitValue = SkewFit->Eval(1,0,0,0);
    double dataValue = (double)HitMultiplicity_H.rpc[T][S][p]->GetBinContent(2);
    double difference = TMath::Abs(dataValue - fitValue);
    double fitTOdataVSentries_ratio = difference / (double)nEntries;
    bool isFitGOOD = fitTOdataVSentries_ratio < 0.01;

2095
    double nSinglehit = (double)HitMultiplicity_H.rpc[T][S][p]->GetBinContent(1);
    double lowMultRatio = nSinglehit / (double)nEntries;
    bool isMultLOW = lowMultRatio > 0.4;

    if(isFitGOOD && !isMultLOW){
        nEmptyEvent = HitMultiplicity_H.rpc[T][S][p]->GetBinContent(1);
        nPhysics = (int)SkewFit->Eval(0,0,0,0);
        if(nPhysics < nEmptyEvent)
            nEmptyEvent = nEmptyEvent-nPhysics;
    }
}

double corrupt_ratio = 100.*(double)nEmptyEvent / (double)nEntries;
outputCorrCSV << corrupt_ratio << '\t';

float rate_norm = 0.;
float stripArea = GIFIInfra->GetStripGeo(tr,sl,p);

if(IsEfficiencyRun(RunType)){
    float noiseWindow = BMTDCWINDOW - TIMEREJECT - 2*PeakWidth.rpc[T][S][p];
    rate_norm = (nEntries-nEmptyEvent)*noiseWindow*1e-9*stripArea;
} else
    rate_norm = (nEntries-nEmptyEvent)*RDMNOISEWDW*1e-9*stripArea;

```

Source Code B.13: Definition of the rate normalisation variable. It takes into account the number of non corrupted entries and the time window used for noise calculation, to estimate the total integrated time, and the strip active area to express the result as rate per unit area.

2097 B.6.4.2 Rate and activity

2098 At this point, the strip rate histograms, StripNoiseProfile_H.rpc[T][S][p], only contain an in-
2099 formation about the total number of noise or rate hits each channel received during the data taking.
2100 As described in Source Code B.14, a loop on the strip channels will be used to normalise the content
2101 of the rate distribution histogram for each detector partitions. The initial number of hits recorded for
2102 a given bin will be extracted and 2 values will be computed:

- 2103 ● the strip rate, defined as the number of hits recorded in the bin normalised like described in
 2104 the previous section, using the variable `rate_norm`, and

- 2105 ● the strip activity, defined as the number of hits recorded in the bin normalised to the average
 2106 number of hits per bin contained in the partition histogram, using the variable `averageNhit`.
 2107 This value provides an information on the homogeneity of the detector response to the gamma
 2108 background or of the detector noise. An activity of 1 corresponds to an average response.
 2109 Above 1, the channel is more active than the average and bellow 1, the channel is less active.

```

int nNoise = StripNoiseProfile_H.rpc[T][S][p]->GetEntries();
float averageNhit = (nNoise>0) ? (float)(nNoise/nStripsPart) : 1.;

for(Uint st = 1; st <= nStripsPart; st++){
    float stripRate =
        StripNoiseProfile_H.rpc[T][S][p]->GetBinContent(st)/rate_norm;
    float stripAct =
        StripNoiseProfile_H.rpc[T][S][p]->GetBinContent(st)/averageNhit;

    StripNoiseProfile_H.rpc[T][S][p]->SetBinContent(st,stripRate);
    StripActivity_H.rpc[T][S][p]->SetBinContent(st,stripAct);
}

```

2111 *Source Code B.14: Description of the loop that allows to set the content of each strip rate and strip activity
 channel for each detector partition.*

2112 On each detector partitions, which are readout by a single FEE, all the channels are not processed
 2113 by the same chip. Each chip can give a different noise response and thus, histograms using a chip
 2114 binning are used to investigate chip related noise behaviours. The average values of the strip rate
 2115 or activity grouped into a given chip are extracted using the using the function `GetChipBin()` and
 2116 stored in dedicated histograms as described in Source Codes B.15 and B.16 respectively.

```

float GetChipBin(TH1* H, Uint chip){
    Uint start = 1 + chip*NSTRIPSCHIP;
    int nActive = NSTRIPSCHIP;
    float mean = 0.;

    for(Uint b = start; b <= (chip+1)*NSTRIPSCHIP; b++){
        float value = H->GetBinContent(b);
        mean += value;
        if(value == 0.) nActive--;
    }

    if(nActive != 0) mean /= (float)nActive;
    else mean = 0.;

    return mean;
}

```

2119 *Source Code B.15: Function used to compute the content of a bin for an histogram using chip binning.*

```

2120   for(UInt ch = 0; ch < (nStripsPart/NSTRIPSCHIP); ch++) {
      ChipMeanNoiseProf_H.rpc[T][S][p]->
          SetBinContent(ch+1,GetChipBin(StripNoiseProfile_H.rpc[T][S][p],ch));
      ChipActivity_H.rpc[T][S][p]->
          SetBinContent(ch+1,GetChipBin(StripActivity_H.rpc[T][S][p],ch));
}

```

Source Code B.16: Description of the loop that allows to set the content of each chip rate and chip activity bins for each detector partition knowing the information contained in the corresponding strip distribution histograms.

The activity variable is used to evaluate the homogeneity of the detector response to background or of the detector noise. The homogeneity h_p of each detector partition can be evaluated using the formula $h_p = \exp(-\sigma_p^R / \langle R \rangle_p)$, where $\langle R \rangle_p$ is the partition mean rate and σ_p^R is the rate standard deviation calculated over the partition channels. The more homogeneously the rates are distributed and the smaller will σ_p^R be, and the closer to 1 will h_p get. On the contrary, if the standard deviation of the channel's rates is large, h_p will rapidly get to 0. This value is saved into histograms as shown in Source Code B.17 and could in the future be used to monitor through time, once extracted, the evolution of every partition homogeneity. This could be of great help to understand the apparition of eventual hot spots due to ageing of the chambers subjected to high radiation levels. The monitored homogeneity information could then be combined with a monitoring of the activity of each individual channel in order to have a finer information. Monitoring tools have been suggested and need to be developed for this purpose.

```

2134   float MeanPartSDev = GetTH1StdDev(StripNoiseProfile_H.rpc[T][S][p]);
   float strip_homog = (MeanPartRate==0)
     ? 0.
     : exp(-MeanPartSDev/MeanPartRate);
   StripHomogeneity_H.rpc[T][S][p]->Fill("exp -#left(#frac{\#sigma_{Strip
     \rightarrow Rate}}{\#mu_{Strip Rate}}\#right)",strip_homog);
   StripHomogeneity_H.rpc[T][S][p]->GetYaxis()->SetRangeUser(0.,1.);

2135   float ChipStDevMean = GetTH1StdDev(ChipMeanNoiseProf_H.rpc[T][S][p]);
   float chip_homog = (MeanPartRate==0)
     ? 0.
     : exp(-ChipStDevMean/MeanPartRate);
   ChipHomogeneity_H.rpc[T][S][p]->Fill("exp -#left(#frac{\#sigma_{Chip
     \rightarrow Rate}}{\#mu_{Chip Rate}}\#right)",chip_homog);
   ChipHomogeneity_H.rpc[T][S][p]->GetYaxis()->SetRangeUser(0.,1.);

```

Source Code B.17: Storage of the homogeneity into dedicated histograms.

B.6.4.3 Strip masking tool

The offline tool is automatically called at the end of each data taking to analyse the data and offer the shifter DQM histograms to control the data quality. After the histograms have been published online in the DQM page, the shifter can decide to mask noisy or dead channels that will contribute to bias the final rate calculation by editing the mask column of `ChannelsMapping.csv` as can be seen in Figure B.3.

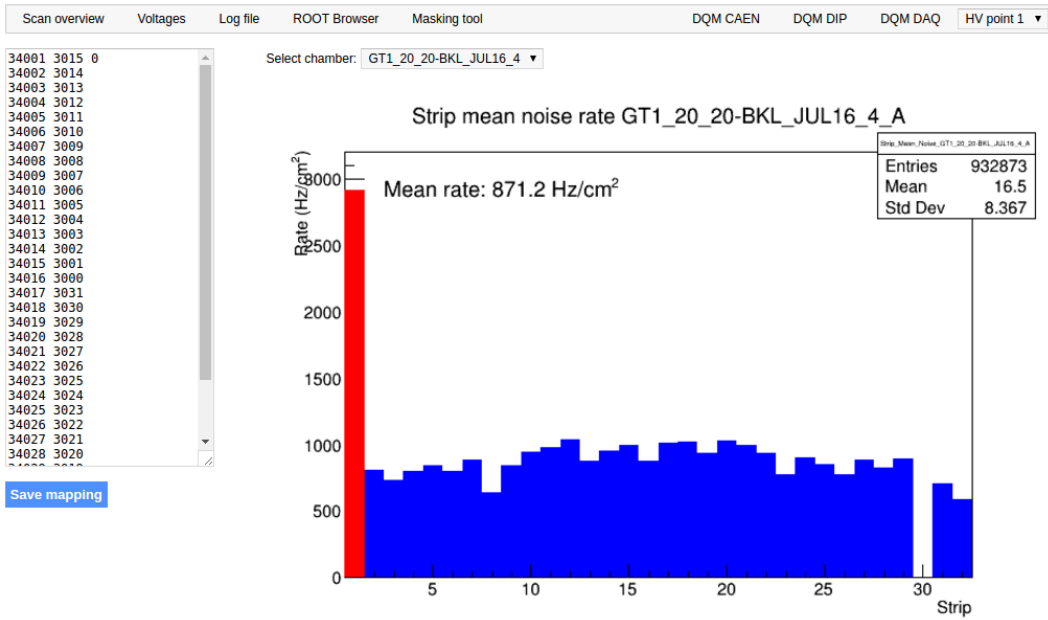


Figure B.3: Display of the masking tool page on the webDCS. The window on the left allows the shifter to edit ChannelsMapping.csv. To mask a channel, it only is needed to set the 3rd field corresponding to the strip to mask to 0. It is not necessary for older mapping file formats to add a 1 for each strip that is not masked as the code is versatile and the default behaviour is to consider missing mask fields as active strips. The effect of the mask is directly visible for noisy channels as the corresponding bin turns red. The global effect of masking strips will be an update of the rate value showed on the histogram that will take into consideration the rejected channels.

2143 From the code point of view, the function `GetTH1Mean()` is used to retrieve the mean rate par-
 2144 tition by partition after the rates have been calculated strip by strip and filled into the histograms
 2145 `StripNoiseProfile_H.rpc[T][S][p]`, as described through Source Code B.18.

2146 Once the mask for each rejected channel has been updated, the shifter can manually run the of-
 2147 fline tool again to update the DQM plots, now including the masked strips, as well the rate results
 2148 written in the output CSV file `Offline-Rate.csv`. If not done during the shifts, the strip masking
 2149 procedure needs to be carefully done by the person in charge of data analysis on the scans that were
 2150 selected to produce the final results.

```

2151
2152     float GetTH1Mean(TH1* H) {
2153         int nBins = H->GetNbinsX();
2154         int nActive = nBins;
2155         float mean = 0.;

2156         for(int b = 1; b <= nBins; b++) {
2157             float value = H->GetBinContent(b);
2158             mean += value;
2159             if(value == 0.) nActive--;
2160         }

2161         if(nActive != 0) mean /= (float)nActive;
2162         else mean = 0.;

2163         return mean;
2164     }

```

Source Code B.18: The function `GetTH1Mean()` is used to return the mean along the y-axis of `TH1` histograms containing rate information. In order to take into account masked strips whose rate is set to 0, the function looks for masked channels and decrement the number of active channels for each null value found.

2154 B.6.4.4 Output CSV files filling

2155 All the histograms have been filled. Parameters will then be extracted from them to compute the
 2156 final results that will later be used to produce plots. Once the results have been computed, the very
 2157 last step of the offline macro is to write these values into the corresponding CSV outputs. Aside of
 2158 the file `Offline-Corrupted.csv`, 2 CSV files are being written by the macro `offlineAnalysis()`,
 2159 `Offline-Rates.csv` and `Offline-L0-EffCl.csv` that respectively contain information about noise
 2160 or gamma rates, cluster size and multiplicity, and about level 0 reconstruction of the detector effi-
 2161 ciency, muon cluster size and multiplicity. Details on the computation and file writing are respec-
 2162 tively given in Sources Codes B.19 and B.20.

2163 **Noise/gamma background variables** are computed and written in the output file for each detector
 2164 partitions. A detector average of the hit and cluster rate is also provided, as shown through Sources
 2165 Code B.19. The variables that are written for each partition are:

- 2166 • The mean partition hit rate per unit area, `MeanPartRate`, that is extracted from the histogram
 2167 `StripNoiseProfile_H` as the mean value along the y-axis, as described in section B.6.4.3. No
 2168 error is recorded for the hit rate as this is considered a single measurement. No statistical error
 2169 can be associated to it and the systematics are unknown.
- 2170 • The mean cluster size, `cSizePart`, is extracted from the histogram `NoiseCSize_H` and it's
 2171 statistical error, `cSizePartErr`, is taken to be 2σ of the total distribution.
- 2172 • The mean cluster multiplicity per trigger, `cMultPart`, is extracted from the histogram `NoiseCMult_H`
 2173 and it's statistical error, `cMultPartErr`, is taken to be 2σ of the total distribution. It is impor-
 2174 tant to point to the fact that this variable gives an information that is dependent on the buffer
 2175 window width used for each trigger for the calculation.
- 2176 • The mean cluster rate per unit area, `ClustPartRate`, is defined as the mean hit rate normalised

2177 to the mean cluster size and it's statistical error, `ClustPartRateErr`, is then obtained using the
 2178 relative statistical error on the mean cluster size.

```

for (UInt tr = 0; tr < GIFInfra->GetNTrolleys(); tr++) {
  UInt T = GIFInfra->GetTrolleyID(tr);

  for (UInt sl = 0; sl < GIFInfra->GetNSlots(tr); sl++) {
    UInt S = GIFInfra->GetSlotID(tr,sl) - 1;

    float MeanNoiseRate = 0.;
    float ClusterRate = 0.;
    float ClusterSDev = 0.;

    for (UInt p = 0; p < GIFInfra->GetNPartitions(tr,sl); p++) {
      float MeanPartRate = GetTH1Mean(StripNoiseProfile_H.rpc[T][S][p]);
      float cSizePart = NoiseCSIZE_H.rpc[T][S][p]->GetMean();
      float cSizePartErr = (NoiseCSIZE_H.rpc[T][S][p]->GetEntries()==0)
        ? 0.
        : 2*NoiseCSIZE_H.rpc[T][S][p]->GetStdDev() /
          sqrt(NoiseCSIZE_H.rpc[T][S][p]->GetEntries());
      float cMultPart = NoiseCMult_H.rpc[T][S][p]->GetMean();
      float cMultPartErr = (NoiseCMult_H.rpc[T][S][p]->GetEntries()==0)
        ? 0.
        : 2*NoiseCMult_H.rpc[T][S][p]->GetStdDev() /
          sqrt(NoiseCMult_H.rpc[T][S][p]->GetEntries());
      float ClustPartRate = (cSizePart==0) ? 0.
        : MeanPartRate/cSizePart;
      float ClustPartRateErr = (cSizePart==0) ? 0.
        : ClustPartRate * cSizePartErr/cSizePart;

      outputRateCSV << MeanPartRate << '\t'
        << cSizePart << '\t' << cSizePartErr << '\t'
        << cMultPart << '\t' << cMultPartErr << '\t'
        << ClustPartRate << '\t' << ClustPartRateErr << '\t';

      RPCarea += stripArea * nStripsPart;
      MeanNoiseRate += MeanPartRate * stripArea * nStripsPart;
      ClusterRate += ClustPartRate * stripArea * nStripsPart;
      ClusterSDev += (cSizePart==0)
        ? 0.
        : ClusterRate*cSizePartErr/cSizePart;
    }

    MeanNoiseRate /= RPCarea;
    ClusterRate /= RPCarea;
    ClusterSDev /= RPCarea;

    outputRateCSV << MeanNoiseRate << '\t'
      << ClusterRate << '\t' << ClusterSDev << '\t';
  }
}

```

2180 *Source Code B.19: Description of rate result calculation and writing into the CSV output Offline-Rate.csv. Are saved into the file for each detector, the mean partition rate, cluster size and cluster mutiplicity, along with their errors, for each partition and as well as a detector average.*

2181 **Muon performance variables** are computed and written in the output file for each detector parti-
 2182 tions as shown through Sources Code B.20. The variables that are written for each partition are:

- 2183 ● The muon efficiency, `eff`, extracted from the histogram `Efficiency0_H`. It is reminded that
2184 this offline tool doesn't include any tracking algorithm to identify muons from the beam and
2185 only relies on the hits arriving in the time window corresponding to the beam time. The con-
2186 tent of the efficiency histogram is thus biased by the noise/gamma background contribution
2187 into this window and is thus corrected by estimating the muon data content in the peak re-
2188 gion knowing the noise/gamma content in the rate calculation region. Both time windows
2189 being different, the choice was made to normalise the noise/gamma background calculation
2190 window to it's equivalent beam window in order to have comparable values using the variable
2191 `windowRatio`. Finally, to estimate the data ratio in the peak region, the variable `DataRatio`
2192 is defined as the ratio in between the estimated mean cluster multiplicity of the muons in the
2193 peak region, `MuonCM`, and of the total mean cluster multiplicity in the peak region, `PeakCM`.
2194 `MuonCM` is itself defined as the difference in between the total mean cluster multiplicity in the
2195 peak region and the normalised mean noise/gamma cluster multiplicity calculated outside of
2196 the peak region. The statistical error related to the efficiency, `eff_err`, is computed using a
2197 binomial distribution, as the efficiency measure the probability of "success" and "failure" to
2198 detect muons.
- 2199 ● The mean muon cluster size, `MuonCS`, is calculated using the total mean cluster size and multi-
2200 plicity in the peak region, respectively extracted from histograms `MuonCSize_H` and `MuonCMult_H`,
2201 the noise/gamma background mean cluster size and normalised multiplicity, extracted from
2202 `NoiseCSize_H` and `NoiseCMult_H`, and of the estimated muon cluster multiplicity `MuonCM` pre-
2203 viously explicated. The associated statistical error, `MuonCM_err`, is calculated using the propa-
2204 gation of errors of the mentioned variables.
- 2205 ● The mean muon cluster multiplicity in the peak region, `MuonCM`, explicated above whose sta-
2206 tistical error, `MuonCM_err`, is the sum of statistical error associated to the total mean clus-
2207 ter multiplicity in the peak reagion, `PeakCM_err`, and of the mean noise/gamma cluster size,
2208 `NoiseCM_err`.

2209 In addition to these 2 CSV files, the histograms are saved in ROOT file `Scan00XXXX_HVY_Offline.root`
2210 as explained in section B.2.1.1.

2211

```

for (UInt tr = 0; tr < GIFInfra->GetNTrolleys(); tr++) {
    UInt T = GIFInfra->GetTrolleyID(tr);
    for (UInt sl = 0; sl < GIFInfra->GetNSlots(tr); sl++) {
        UInt S = GIFInfra->GetSlotID(tr,sl) - 1;
        for (UInt p = 0; p < GIFInfra->GetNPartitions(tr,sl); p++) {
            float noiseWindow =
                BMTDCWINDOW - TIMEREJECT - 2*PeakWidth.rpc[T][S][p];
            float peakWindow = 2*PeakWidth.rpc[T][S][p];
            float windowRatio = peakWindow/noiseWindow;

            float PeakCM = MuonCMult_H.rpc[T][S][p]->GetMean();
            float PeakCS = MuonCSize_H.rpc[T][S][p]->GetMean();
            float NoiseCM = NoiseCMult_H.rpc[T][S][p]->GetMean() *windowRatio;
            float NoiseCS = NoiseCSize_H.rpc[T][S][p]->GetMean();
            float MuonCM = (PeakCM<NoiseCM) ? 0. : PeakCM-NoiseCM;
            float MuonCS = (MuonCM==0 || PeakCM*PeakCS<NoiseCM*NoiseCS)
                ? 0.
                : (PeakCM*PeakCS-NoiseCM*NoiseCS) / MuonCM;
            float PeakCM_err = (MuonCMult_H.rpc[T][S][p]->GetEntries()==0.)
                ? 0.
                : 2*MuonCMult_H.rpc[T][S][p]->GetStdDev() /
                    sqrt(MuonCMult_H.rpc[T][S][p]->GetEntries());
            float PeakCS_err = (MuonCSize_H.rpc[T][S][p]->GetEntries()==0.)
                ? 0.
                : 2*MuonCSize_H.rpc[T][S][p]->GetStdDev() /
                    sqrt(MuonCSize_H.rpc[T][S][p]->GetEntries());
            float NoiseCM_err = (NoiseCMult_H.rpc[T][S][p]->GetEntries()==0.)
                ? 0.
                : windowRatio*2*NoiseCMult_H.rpc[T][S][p]->GetStdDev() /
                    sqrt(NoiseCMult_H.rpc[T][S][p]->GetEntries());
            float NoiseCS_err = (NoiseCSize_H.rpc[T][S][p]->GetEntries()==0.)
                ? 0.
                : 2*NoiseCSize_H.rpc[T][S][p]->GetStdDev() /
                    sqrt(NoiseCSize_H.rpc[T][S][p]->GetEntries());
            float MuonCM_err = (MuonCM==0) ? 0. : PeakCM_err+NoiseCM_err;
            float MuonCS_err = (MuonCS==0 || MuonCM==0) ? 0.
                : (PeakCS*PeakCM_err + PeakCM*PeakCS_err +
                    NoiseCS*NoiseCM_err + NoiseCM*NoiseCS_err +
                    MuonCS*MuonCM_err) / MuonCM;

            float DataRatio = MuonCM/PeakCM;
            float DataRatio_err = (MuonCM==0) ? 0.
                : DataRatio*(MuonCM_err/MuonCM + PeakCM_err/PeakCM);
            float eff = DataRatio*Efficiency0_H.rpc[T][S][p]->GetMean();
            float eff_err = DataRatio*2*Efficiency0_H.rpc[T][S][p]->GetStdDev() /
                sqrt(Efficiency0_H.rpc[T][S][p]->GetEntries()) +
                Efficiency0_H.rpc[T][S][p]->GetMean()*DataRatio_err;

            outputEffCSV << eff << '\t' << eff_err << '\t'
                << MuonCS << '\t' << MuonCS_err << '\t'
                << MuonCM << '\t' << MuonCM_err << '\t';
        }
    }
}

```

2212

2213

Source Code B.20: Description of efficiency result calculation and writing into the CSV output Offline-L0-EffCl.csv. Are saved into the file for each detector, the efficiency, corrected taking into account the background in the peak window of the time profile, muon cluster size and muon cluster multiplicity, along with their errors, for each partition and as well as a detector average.

2214 B.7 Current data Analysis

2215 Detectors under test at GIF++ are connected both to a CAEN HV power supply and to a CAEN
2216 ADC that reads the currents inside of the RPC gaps bypassing the supply cable. During data tak-
2217 ing, the webDCS records into a ROOT file called `Scan00XXXX_HVY_CAEN.root` histograms with the
2218 monitored parameters of both CAEN devices. Are recorded for each RPC channels (in most cases,
2219 a channel corresponds to an RPC gap):

- 2220 • the effective voltage, HV_{eff} , set by the webDCS using the PT correction on the CAEN power
2221 supply,
- 2222 • the applied voltage, HV_{app} , monitored by the CAEN power supply, and the statistical error
2223 related to the variations of this value through time to follow the variation of the environmental
2224 parameters defined as the RMS of the histogram divided by the square root of the number of
2225 recorded points,
- 2226 • the monitored current, I_{mon} , monitored by the CAEN power supply, and the statistical error
2227 related to the variations of this value through time to follow the variation of the environmental
2228 parameters defined as the RMS of the histogram divided by the square root of the number of
2229 recorded points,
- 2230 • the corresponding current density, J_{mon} , defined as the monitored current per unit area,
2231 $J_{mon} = I_{mon}/A$, where A is the active area of the corresponding gap,
- 2232 • the ADC current, I_{ADC} , recorded through the CAEN ADC module that monitors the dark
2233 current in the gap itself. First of all, the resolution of such a module is better than that of
2234 CAEN power supplies and moreover, the current is not read-out through the HV supply line
2235 but directly at the chamber level giving the real current inside of the detector. The statistical
2236 error is defined as the RMS of the histogram distribution divided by the square root of the
2237 number of recorded points.

2238 Once extracted through a loop over the element of GIF++ infrastructure via the C++ macro
2239 `GetCurrent()`, these parameters, organised in 9 columns per detector HV supply line, are written in
2240 the output CSV file `Offline-Current.csv`. The macro can be found in the file `Current.cc`.

References

2241

- 2242 [1] T. Massam et al. “Experimental observation of antideuteron production”. In: *Il Nuovo Cimento A* 63 (1965), pp. 10–14.
- 2243
- 2244 [2] UA1 Collaboration. “Experimental observation of isolated large transverse energy electrons with associated missing energy at $s = 540 \text{ GeV}$ ”. In: *Physics Letters B* 122 (1983), pp. 103–116.
- 2245
- 2246 [3] UA2 Collaboration. “Observation of single isolated electrons of high transverse momentum in events with missing transverse energy at the CERN pp collider”. In: *Physics Letters B* 122 (1983), pp. 476–485.
- 2247
- 2248 [4] UA1 Collaboration. “Experimental observation of lepton pairs of invariant mass around $95 \text{ GeV}/c^2$ at the CERN SPS collider”. In: *Physics Letters B* 126 (1983), pp. 398–410.
- 2249
- 2250 [5] UA2 Collaboration. “Evidence for $Z_0 \rightarrow e^+e^-$ at the CERN pp collider”. In: *Physics Letters B* 129 (1983), pp. 130–140.
- 2251
- 2252 [6] ALEPH Collaboration. “Determination of the number of light neutrino species”. In: *Physics Letters B* 231 (1989), pp. 519–529.
- 2253
- 2254 [7] CERN, ed. (1985).
- 2255
- 2256 [8] CERN, ed. (1986).
- 2257
- 2258 [9] CERN, ed. (1994).
- 2259
- 2260 [10] CERN, ed. (1998).
- 2261
- 2262 [11] CERN, ed. (1999).
- 2263
- 2264 [12] CERN. Geneva. LHC Experiments Committee. *Letter of Intent for A Large Ion Collider Experiment [ALICE]*, note = CERN-LHCC-93-016. Tech. rep. ALICE Collaboration, 1993.
- 2265
- 2266 [13] CERN. Geneva. LHC Experiments Committee. *ATLAS : technical proposal for a general-purpose pp experiment at the Large Hadron Collider at CERN*, note = CERN-LHCC-94-43. Tech. rep. ATLAS Collaboration, 1994.
- 2267
- 2268 [14] CERN. Geneva. LHC Experiments Committee. *CMS : letter of intent by the CMS Collaboration for a general purpose detector at LHC*, note = CERN-LHCC-92-003. Tech. rep. CMS Collaboration, 1992.
- 2269
- 2270 [15] CERN. Geneva. LHC Experiments Committee. *LHCb : letter of intent*. Tech. rep. CERN-LHCC-95-5. LHCb Collaboration, 1995.
- 2271
- 2272 [16] L. Evans and P. Bryant. “LHC Machine”. In: *JINST* 3 (2008). S08001.
- 2273
- 2274 [17] CMS Collaboration ATLAS Collaboration. “Combined Measurement of the Higgs Boson Mass in pp Collisions at $\sqrt{s} = 7$ and 8 TeV with the ATLAS and CMS Experiments”. In: *Physical Review Letters* 114 (2015). 191803.
- 2275
- 2276 [18] LHCb Collaboration. “Observation of $J/\psi p$ Resonances Consistent with Pentaquark States in $\Lambda_b^0 \rightarrow J/\psi K^- p$ Decays”. In: *Physical Review Letters* 115 (2015). 072001.

- 2277 [19] LHCb Collaboration. “Observation of $J/\psi\phi$ Structures Consistent with Exotic States from
2278 Amplitude Analysis of $B^+ \rightarrow J/\psi\phi K^+$ Decays”. In: *Physical Review Letters* 118 (2017).
2279 022003.
- 2280 [20] CERN. Geneva. *High-Luminosity Large Hadron Collider (HL-LHC) Technical Design Re-*
2281 *port V. 0.1*. Tech. rep. CERN-2017-007-M. 2017.
- 2282 [21] CERN. Geneva. LHC Experiments Committee. *The CMS muon project : Technical Design*
2283 *Report*. Tech. rep. CERN-LHCC-97-032. CMS Collaboration, 1997.
- 2284 [22] CERN. Geneva. LHC Experiments Committee. *Technical Proposal for the Phase-II Upgrade*
2285 *of the CMS Detector*. Tech. rep. CERN-LHCC-2015-010. CMS Collaboration, 2015.
- 2286 [23] CERN. Geneva. LHC Experiments Committee. *CMS, the Compact Muon Solenoid : technical*
2287 *proposal*. Tech. rep. CERN-LHCC-94-38. CMS Collaboration, 1994.
- 2288 [24] R. Santonico and R. Cardarelli. “Development of resistive plate counters”. In: *Nucl. Instr.*
2289 *Meth. Phys. Res.* 187 (1981), pp. 377–380.
- 2290 [25] Yu.N. Pestov and G.V. Fedotovich. *A picosecond time-of-flight spectrometer for the VEPP-2M*
2291 *based on local-discharge spark counter*. Tech. rep. SLAC-TRANS-0184. SLAC, 1978.
- 2292 [26] W.W. Ash, ed. *Spark Counter With A Localized Discharge*. Vol. SLAC-R-250. 1982, pp. 127–
2293 131.
- 2294 [27] I. Crotty et al. “The non-spark mode and high rate operation of resistive parallel plate cham-
2295 bers”. In: *NIMA* 337 (1993), pp. 370–381.
- 2296 [28] I. Crotty et al. “Further studies of avalanche mode operation of resistive parallel plate cham-
2297 bers”. In: *NIMA* 346 (1994), pp. 107–113.
- 2298 [29] R. Cardarelli et al. “Avalanche and streamer mode operation of resistive plate chambers”. In:
2299 *NIMA* 382 (1996), pp. 470–474.
- 2300 [30] E. Cerron Zeballos et al. “A new type of resistive plate chamber: The multigap RPC”. In:
2301 *NIMA* 374 (1996), pp. 132–135.
- 2302 [31] M.C.S. Williams. “The development of the multigap resistive plate chamber”. In: *Nucl. Phys.*
2303 *B* 61 (1998), pp. 250–257.
- 2304 [32] H. Czyrkowski et al. “New developments on resistive plate chambers for high rate operation”.
2305 In: *NIMA* 419 (1998), pp. 490–496.
- 2306 [33] P. Camarri et al. “Streamer suppression with SF6 in RPCs operated in avalanche mode”. In:
2307 *NIMA* 414 (1998), pp. 317–324.
- 2308 [34] E. Cerron Zeballos et al. “Effect of adding SF6 to the gas mixture in a multigap resistive plate
2309 chamber”. In: *NIMA* 419 (1998), pp. 475–478.
- 2310 [35] CERN. Geneva. LHC Experiments Committee. *ATLAS muon spectrometer: Technical design*
2311 *report*. Tech. rep. CERN-LHCC-97-22. ATLAS Collaboration, 1997.
- 2312 [36] CERN. Geneva. LHC Experiments Committee. *ALICE Time-Of-Flight system (TOF) : Tech-*
2313 *nical Design Report*. Tech. rep. CERN-LHCC-2000-012. ALICE Collaboration, 2000.
- 2314 [37] The CALICE collaboration. “First results of the CALICE SDHCAL technological proto-
2315 type”. In: *JINST* 11 (2016).
- 2316 [38] PoS, ed. *Density Imaging of Volcanoes with Atmospheric Muons using GRPCs*. International
2317 Europhysics Conference on High Energy Physics - HEP 2011. 2011.
- 2318 [39] C. Lippmann. “Detector Physics of Resistive Plate Chambers”. PhD thesis. Johann Wolfgang
2319 Goethe-Universität, 2003.

BIBLIOGRAPHY

- [40] M. Abbrescia et al. “Properties of C₂H₂F₄-based gas mixture for avalanche mode operation of resistive plate chambers”. In: *NIMA* 398 (1997), pp. 173–179.
- [41] G. Battistoni et al. “Sensitivity of streamer mode to single ionization electrons”. In: *NIMA* 235 (1985), pp. 91–97.
- [42] W. Riegler. “Induced signals in resistive plate chambers”. In: *NIMA* 491 (2002), pp. 258–271.
- [43] E. Cerron Zeballos et al. “A comparison of the wide gap and narrow gap resistive plate chamber”. In: *NIMA* 373 (1996), pp. 35–42.
- [44] M. Abbrescia et al. “Cosmic ray tests of double-gap resistive plate chambers for the CMS experiment”. In: *NIMA* 550 (2005), pp. 116–126.
- [45] ALICE Collaboration. “A study of the multigap RPC at the gamma irradiation facility at CERN”. In: *NIMA* 490 (2002), pp. 58–70.
- [46] B. Bonner et al. “A multigap resistive plate chamber prototype for time-of-flight for the STAR experiment at RHIC”. In: *NIMA* 478 (2002), pp. 176–179.
- [47] S. Yang et al. “Test of high time resolution MRPC with different readout modes for the BESIII upgrade”. In: *NIMA* 763 (2014), pp. 190–196.
- [48] A. Akindinov et al. “RPC with low-resistive phosphate glass electrodes as a candidate for the CBM TOF”. In: *NIMA* 572 (2007), pp. 676–681.
- [49] JINST, ed. *Development of the MRPC for the TOF system of the MultiPurpose Detector*. RPC2016: XII Workshop on Resistive Plate Chambers and Related Detectors. 2016.
- [50] M.C.S. Williams. “Particle identification using time of flight”. In: *Journal of Physics G* 39 (2012).
- [51] A. Alici et al. “Aging and rate effects of the Multigap RPC studied at the Gamma Irradiation Facility at CERN”. In: *NIMA* 579 (2007), pp. 979–988.
- [52] M. Abbrescia et al. “The simulation of resistive plate chambers in avalanche mode: charge spectra and efficiency”. In: *NIMA* 431 (1999), pp. 413–427.
- [53] M. Abbrescia et al. “Study of long-term performance of CMS RPC under irradiation at the CERN GIF”. In: *NIMA* 533 (2004), pp. 102–106.
- [54] H.C. Kim et al. “Quantitative aging study with intense irradiation tests for the CMS forward RPCs”. In: *NIMA* 602 (2009), pp. 771–774.
- [55] S. Agosteo et al. “A facility for the test of large-area muon chambers at high rates”. In: *NIMA* 452 (2000), pp. 94–104.
- [56] PoS, ed. *CERN GIF ++ : A new irradiation facility to test large-area particle detectors for the high-luminosity LHC program*. Vol. TIPP2014. 2014, pp. 102–109.
- [57] A. Fagot. *GIF++ DAQ v4.0*. 2017. URL: https://github.com/afagot/GIF_DAQ.
- [58] CAEN. *Mod. V1190-VX1190 A/B, 128/64 Ch Multihit TDC*. 14th ed. 2016.
- [59] CAEN. *Mod. V1718 VME USB Bridge*. 9th ed. 2009.
- [60] W-Ie-Ne-R. *VME 6021-23 VXI*. 5th ed. 2016.
- [61] Wikipedia. *INI file*. 2017. URL: https://en.wikipedia.org/wiki/INI_file.
- [62] S. Carrillo A. Fagot. *GIF++ Offline Analysis v6*. 2017. URL: https://github.com/afagot/GIF_OfflineAnalysis.